EXPERIMENTAL INVESTIGATIONS OF FLOW DEVELOPMENT, GAP INSTABILITY AND GAP VORTEX STREET GENERATION IN ECCENTRIC ANNULAR CHANNELS

by

George H. Choueiri

Thesis submitted to the
Faculty of Graduate and Postdoctoral Studies
in partial fulfillment of the requirements
for the Doctorate in Philosophy degree in Mechanical Engineering

Ottawa-Carleton Institute for Mechanical and Aerospace Engineering
Faculty of Engineering
University of Ottawa

Abstract

Isothermal flow development, gap instability, and gap vortex street generation in eccentric annular channels have been studied experimentally. A representative paradigm of a flow in a highly eccentric annular channel was examined for a channel having an inner-to-outer diameter ratio $d/D = 0.50$ and an eccentricity $e = 0.8$ for a Reynolds number Re = 7300. Observation of the flow development has identified three distinct regions: the entrance region, the fluctuation-growth region and the rapid-mixing region. Weak quasi-periodic velocity fluctuations were first detected in the downstream part of the entrance region, and grew into very strong ones, reaching peak-to-peak amplitudes in the narrow gap that were nearly 60% of the bulk velocity. The dependence on inlet conditions, d/D, e and Re on the development and structure of flows was also investigated. Experimental conditions covered the ranges: $0 \leq \text{Re} \leq 19000$, $0 \leq e \leq 0.9$ and $d/D = 0.25$, 0.50 and 0.75. For Re < 7000, the Strouhal number, the normalized mid-gap axial flow velocity and the axial and cross-flow fluctuation intensities at mid-gap were found to increase with increasing Re and to depend strongly on inlet conditions. At higher Re, however, these parameters reached asymptotic values that were only mildly sensitive to inlet conditions. A map was constructed for the various stages of periodic motions *vs.* e and Re and it was found that, for $e < 0.5$ or Re < 1100, the flow was unconditionally stable as far as gap instability is concerned. For $e \leq 0.5$, transition to turbulence occurred at Re $\approx$ 6000, whereas, for $0.6 \leq e \leq 0.9$, the critical Reynolds number for the formation of periodic motions was found to increase with eccentricity from 1100 for e = 0.6 to 3800 for e = 0.9. The use of an empirically derived "mixing layer Strouhal number" permitted a universal description of gap vortex street periodicity in eccentric annular channels. This study has contributed to our understanding of the physical mechanisms that lead to gap instability and the development of a gap vortex street and the dependence of these flow phenomena on the channel geometry and the dynamic conditions of the flow.

Acknowledgements

First and foremost, I acknowledge my supervisor Professor Stavros Tavoularis whose mentorship, support, dedication and friendship have left an eternal mark on my professional and personal life; the only regret I have in all the time I've spent under his supervision is that I have not thanked him enough for all he has and continues to do.

I acknowledge the mechanical engineering department at the University of Ottawa and the professors and support staff who have made me feel at home this whole time; particularly Professors Bertrand Jodoin and William Hallett (Department Chairs) and Susan Rennie, John Perrins, Leo Denner, Stanley Weedmark and Michael Burns (support staff).

I would like to thank my colleagues for their insight, support and friendship, especially those whom served with me in my time as president of OMEGA; Iain Baxter, Christina Vanderwel, Laura Brown and Eli Marshall.

I also thank my beautiful wife, Anne-Lise, who has taught me the meaning of sacrifice, patience and love; her ever-smiling face and twinkling eyes got me through many snowy days and thesis edits.

I would finally like to acknowledge the financial support of the Natural Sciences and Engineering Research Council of Canada and Atomic Energy of Canada Limited.

Table of Contents

List of Tables

List of Figures

Nomenclature

A cross-sectional area, m^2

a half length of LDV measurement volume, m

c length scale in eccentric annulus, m

D outer diameter in annuli and rod-bundles, m

d diameter, core diameter in annuli and rod-bundles, m

e eccentricity

f frequency, Hz

f_T lens focal distance, m

L length, m

n index of refraction

P wetted perimeter, m

p pitch, m

Re Reynolds number

St Strouhal number

U average velocity, m/s

u velocity, m/s

u' velocity fluctuations

w combined width of wall bounded gap and rod, m

x axis parallel to gap, m

y axis perpendicular to gap, m

z axial position starting from the inlet of the test section, m

Greek symbols

α intersection half angle of LDV laser beams

δ gap spacing, m

δ_w shear layer thickness, m

ξ gap instability mass transfer number

ϑ dimensionless velocity

λ wavelength, nm

μ dynamic viscosity, kg/m $\cdot$ s

ν kinematic viscosity, m^2/s

Subscripts

b bulk or averaged value

cr critical value for gap instability

e pertaining to laser beam

fe pertaining to focused laser beam

h hydraulic

mv measurement volume

o reference case

tr critical value for transition to turbulence

Acronyms

CFD computational fluid dynamics

CPC connected parallel channels (mainly rectangular, see figure 1-b)

DNS direct numerical simulation

IDDES improved delayed detached eddy simulations

LDV laser Doppler velocimetry

LES large eddy simulation

PIV particle image velocimetry

RANS Reynolds-averaged Navier-Stokes

RCR rectangular cross-section containing a rod (see figure 1-c)

SAS scale adaptive simulations

URANS unsteady Reynolds-averaged Navier-Stokes

Chapter 1

Introduction

1.1 Flow instability, transition and turbulence

Flow instability, transition to turbulence and turbulence characteristics in geometrically simple free and bounded shear flows are essential topics of fundamental fluid mechanics and heat transfer. The physical mechanisms that eventually lead to transition of a laminar flow to a turbulent one are usually associated with one or more hydrodynamic instability processes. An unstable laminar flow may break down and be replaced by a stable laminar flow or undergo transition to a turbulent flow (Drazin & Reid, 2004). In general, instability is triggered by some disturbance which upsets the momentum balance of the system. Among the various influencing forces, some play a stabilizing role and others a destabilizing one. Viscous forces generally dissipate the energy of disturbances, thus acting in a stabilizing fashion. However, friction also diffuses momentum, which may destabilize a flow.

In elementary fluid mechanics textbooks, laminar flows are described as ones in which fluid flows in smooth layers or laminae (Fox *et al.*, 2004; Massey & Ward-Smith, 2006). A more general description of laminar flows is that they are flows with strong momentum diffusion and weak momentum convection (Grandy & Grandy,

2008; Bhowmik & Bose, 2010; Wu, 2010). The latter definition includes flows with large-scale vortical and wave-like motions. Turbulent flows are generally characterized by high levels of dissipation and randomness; additional characteristics of turbulent flows are detailed in section 3.1.

As the famous Reynolds pipe flow experiments demonstrated, a flow can be laminar or turbulent depending on the values of various parameters, which can be combined into a dimensionless group, called the Reynolds number. A flow in a pipe could start out laminar and become turbulent further downstream. It is also possible to observe turbulent patches within an otherwise laminar flow. The Reynolds number is a measure of the ratio of strengths of inertia and viscous forces. The Reynolds number at which a flow becomes unstable is called the critical Reynolds number. This term is sometimes also used to denote transition to turbulence, although instability and transition are distinct concepts.

1.2 Flows in channels with narrow gaps

Flows in channels with simple cross-sections such as pipes, rectangular ducts and rivers with a single main channel, as well as flows in concentric annular channels, have relatively simple velocity distributions on transverse planes. In contrast, flows in channels which contain narrow gaps connected to larger subchannels, such as those shown in figure 1.1, have cross-sectional velocity variations which are inflectional; inflection points in velocity profiles are known to cause hydrodynamic instability (Rayleigh, 1880; Greitzer *et al.*, 2004).

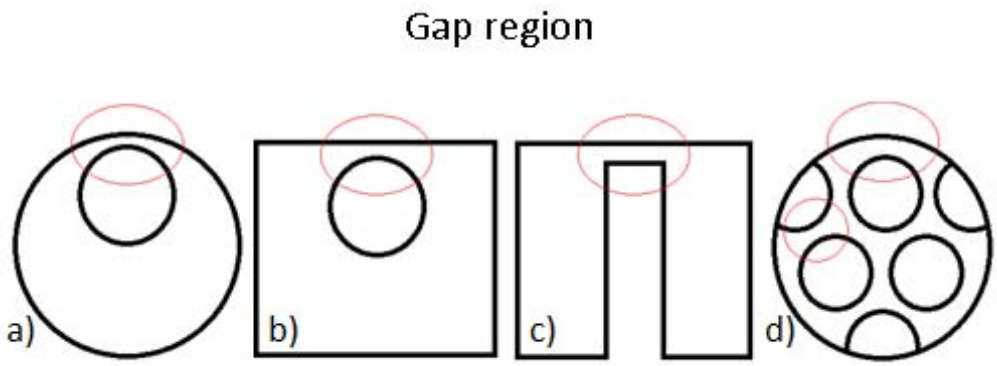

Figure 1.1: Examples of channels with narrow gap regions.

Flows in channels with narrow gaps are found in a variety of engineering and environmental applications. Examples are air flows through heat sinks of electronic components, liquid coolant circulating through the cores of nuclear reactors and water flowing in rivers with inundated flood plains. Of particular interest to the present study are flows in nuclear reactor rod bundles. Mixing of flows in adjacent subchannels of a rod bundle can be caused by different mechanisms. Mixing occurs because of pressure differences between subchannels, arising from differences in mean subchannel velocities or as a result of flow obstruction by spacers and end-plates supporting the fuel elements. Additionally, mixing can occur by means of turbulent diffusion between subchannels; this turbulent interchange is generally non-directional and causes exchange of momentum, enthalpy and concentration between adjacent subchannels without a time averaged net mass transport (Rehme, 1992). Finally, large-scale vortical structures forming about the inflection points in the cross-sectional velocity profile tend to transport fluid from one subchannel to another across narrow gaps. This form

of mixing, which is the primary focus of this study, is especially beneficial in tightly-packed nuclear reactor rod bundles as it tends to even out temperature differences among subchannels and lowers wall temperature peaks in the gaps.

To study the large scale vortical structures near gaps, the present study will look at the simple geometry of eccentric annuli (figure 1.1 a). It has been observed experimentally that, in such geometries, oscillatory cross flows exist and are strongest in the narrow gap (Rowe *et al.*, 1974; Hooper, 1984; Hooper & Rehme, 1984) These cross flows are the result of large scale counter-rotating vortices on either side of the gap, arranged in a quasi-periodic order similar to a von Kármán vortex street. These vortices are generated by a Kelvin-Helmholtz-type instability of the shear layer between the slower fluid in the gap and the faster fluid in the open subchannel. Tavoularis (2011) has introduced the terms "gap instability" and "gap vortex street" to describe these phenomena. He also introduced the term "gap vortex network" to describe collectively all vortex streets that form in a tightly-packed rod bundle and interact with each other, thus coupling the flows in all subchannels of the rod bundle (Baratto *et al.*, 2006).

1.3 Organization of the thesis

This thesis has six chapters. In Chapter 2 we present a literature review, at the end of which we identify gaps in the current understanding of gap instability and present the objectives and scope of the current research. In Chapter 3 we present a brief background section which covers relevant hydrodynamic instability mechanisms. Chapter

4 discusses the apparatus used in this study as well as all the instrumentation and measurement techniques; the final section of this chapter outlines the experimental procedures used, including an assessment of fluid properties. Experimental results and their discussion and analysis are presented in the two sections of Chapter 5, each of which reproduces a manuscript that has been submitted, or is under preparation for submission, to a refereed journal for possible publication. Chapter 6 summarizes the results and presents some thoughts on future research.

Chapter 2

Literature Review and Background Material

2.1 Overview

The observation of unusual flow phenomena in rod bundles was first reported by Hofmann in 1964 (Möller, 1991; Meyer, 2010). Hofmann discovered that the heat transfer coefficient in the gap region increased as the gap size was reduced and attributed this to the presence of transverse flows in the narrow gaps, which he observed using flow visualization. An early explanation for the enhancement of mixing across the gap was the formation of secondary flows transporting mass, momentum and energy from open subchannel regions towards the gap (Tachibana *et al.*, 1969; Skinner *et al.*, 1969; Levchenko *et al.*, 1972; Hooper, 1980; Rapley & Gosman, 1986). Nevertheless, most authors (for example, Seale, 1979; Hooper, 1984; Vonka, 1988a,b; Rehme, 1992) concluded that secondary flow played an insignificant part in cross-gap mixing for tightly packed rod bundles. Rehme (1992) summarized earlier developments in the understanding of this phenomenon and associated increased mixing in rod bundles to large-scale, cross-flow pulsations, dismissing the significance of secondary flow effects. Rehme also tabulated values of empirical mixing factors across the gap from various publications and suggested a simple correlation in terms of the relative gap size.

In a recent historical review, Meyer (2010) outlines the earlier work at Research Center Karlsruhe (FZK) as well as work by several other research groups until recently. Meyer also refers to the early misconceptions of the significance of secondary flows and summarizes the evidence that cross-gap mixing enhancement in tightly-packed rod bundles is due to vortex streets forming on either side of narrow gaps. Decreasing the gap size within a certain range is known to result in stronger vortices, whereas in rod bundles having pitch-to-diameter ratios $p/d > 1.2$, the vortices may not form, or at least their effects on the flow are not measurable. In a recent experimental study, however, Mahmood *et al.* (2011) claim to have found evidence for the presence of vortex streets in a loosely-packed, 4 x 4 square rod-bundle array with $p/d = 1.43$. Based on the wide range of studies summarized by Meyer, one can safely say that, for relatively small p/d, vortex streets have a significant effect on intersubchannel mixing in rod-bundles.

Tavoularis (2011) summarized the current understanding on the topic of large-scale motions in rod-bundles and channels containing narrow gap regions. He associated the instability leading to the formation of such large-scale motions with inflectional cross-sectional velocity distributions (Gosset & Tavoularis, 2006; Piot & Tavoularis, 2011), which lead to hydrodynamic instability similar to those in wakes and boundary layers, although the similarity is not sufficient for all mechanisms to be classified in the same category. In the absence of any previous term to denote flow instability in gaps connecting larger subchannels, Tavoularis introduced the term gap

instability and further proposed the term gap vortex street to describe the physical phenomenon which leads to flow pulsations across individual gaps. In the case of rod-bundles, where multiple narrow gaps exist, the gap vortex streets become coupled together and changing the flow conditions in a single gap would inevitably affect the flow in the entire bundle (Baratto *et al.*, 2006). To account for these interactions, Tavoularis proposed the term rod bundle vortex network. He further stressed the need for more quantitative works in which test section geometry and physical conditions, including those upstream of the test section and at the inlet, would be specified in detail.

2.2 Previous experimental studies

Rowe *et al.* (1974) were among the earliest authors who documented experimentally the existence of macroscopic flow pulsations adjacent to the narrow gap in rod bundles. Using laser Doppler velocimetry (LDV) for Reynolds numbers in the range between $50,000$ and $200,000$; they found that the pitch to diameter ratio (p/d) was the most significant geometric parameter affecting the flow structure, and that decreasing p/d increased the turbulent intensity in the gap region; on the other hand, when p/d was increased to 1.25, no pulsations were observed. Additional observations that the flow pulsations became stronger with decreasing gap size have been made by many other authors for different rod bundle and related geometries and flow conditions (e.g., Hooper, 1983, 1984; Hooper & Wood, 1984; Hooper & Rehme, 1984; Rehme, 1987, 1989; Baratto *et al.*, 2006; Möller, 1991; Guellouz & Tavoularis, 2000a,b; Gosset &

Tavoularis, 2006; Lexmond *et al.*, 2005).

Tapucu & Merilo (1977) studied flows in parallel rectangular channels connected by a narrow gap, and observed nearly sinusoidal pressure fluctuations in the gap region with a wavelength which was a function of gap clearance. Hooper & Rehme (1984) summarized earlier results obtained in two rod bundles, one consisting of four linearly aligned rods in a rectangular duct and a channel consisting of two subchannels formed by six rods with p/d = 1.107, as shown in figure 2.1, and found no evidence that secondary flows affected significantly the gap turbulence. Analysis of measurements in both experimental rigs showed a tendency for the turbulent levels to increase in the gap region as either p/d or w/d were reduced, where w was defined as the sum of the rod diameter and the gap between this rod and an adjacent duct wall. The same authors observed that the time histories of the cross and axial flow velocities in the gap region were quasi-sinusoidal. Hooper & Rehme (1984) attributed the cross-flows to large-scale structures generated to an incompressible flow instability due to static pressure differences between the parallel subchannels; however, this conclusion, according to Meyer (2010), was never substantiated as later measurements (for which no reference was given) using high sensitivity pressure transducers disclosed no relevant pressure fluctuations.

Wu & Trupp (1993) examined flow in a trapezoidal cross-section with a cylindrical core and also attributed the cross-flow and increased mixing between subchannels to large-scale vortices. Möller (1991) used hot wires and microphones to study flow

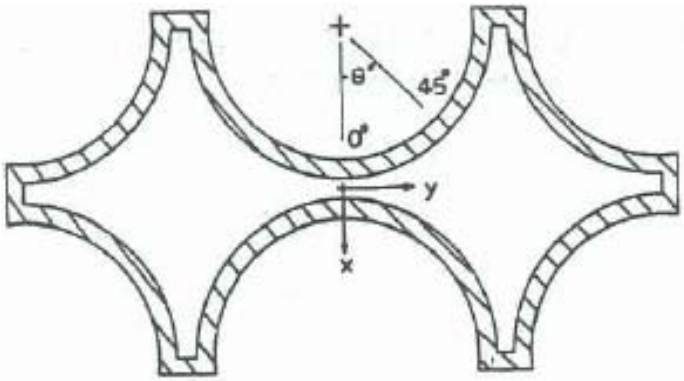

Figure 2.1: Symmetrical six-rod channel cross-section (Hooper, 1983).

in a rod bundle with a linear array of four cylinders inside a rectangular channel; he found a strong enhancement of transverse and axial turbulence in the gap region with decreased gap spacing. The author also proposed a phenomenological model of counter-rotating vortices, but incorrectly positioned their axes in the centre of the gap; he further concluded that the Strouhal number for these vortices was independent of the Reynolds number and inversely proportional to the gap width. Meyer & Rehme (1994, 1995) and Krauss & Meyer (1998) showed that the axes of these vortices were offset on either side of the gap centre. Meyer & Rehme (1994) estimated the diameters of the vortices to be roughly equal to the width of the gap. Guellouz & Tavoularis (2000a) determined that, for the rectangular channel containing a single cylindrical rod cross-section, herein referred to as an RCR type cross-section (see figure 2.2-left), the distance between structures was proportional to gap spacing and the convection velocity of the structures increased with gap spacing, eventually reaching an asymptotic value for $w/d > 1.25$. In the figure 2.2-right, flow visualization shows the cross-gap motions which are associated with gap vortex streets. The authors

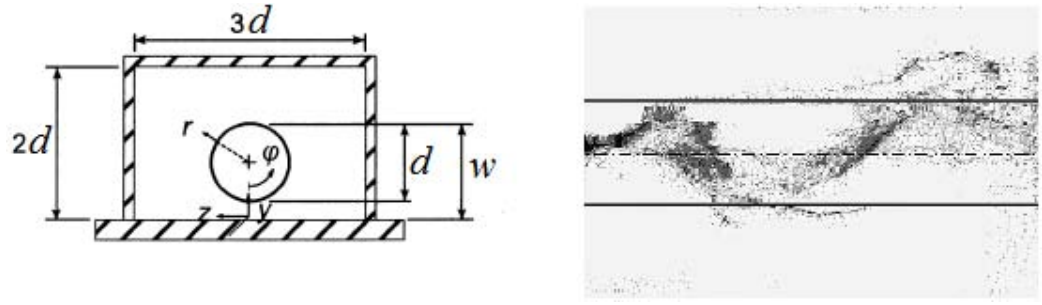

Figure 2.2: Cross-section of apparatus used by Guellouz & Tavoularis (2000a,b) (left) and flow visualization across the narrow gap for Re = 16000 (right).

concluded that the driving mechanism behind the coherent structures was similar to that found in two-dimensional mixing layers, whereby faster flow in the open channel would interact with low velocity flow in the gap region; this is particularly evident when looking at the sense of rotation of the vortices and their spacing.

In one of the earliest published studies on gap instability under laminar flow conditions, Gosset & Tavoularis (2006) attempted to trace the gap vortex streets in RCR type channels to their origins, noting that the characteristics of gap vortex streets under laminar flow conditions were found to be compatible in many ways with those found under turbulent flow conditions. A lower bound for the Reynolds number, below which no cross gap motion was observable, was found and termed the critical Reynolds number; a homage to the Reynolds pipe flow experiments. The critical Reynolds number was found to increase with decreasing gap size; an observation also made by Piot & Tavoularis (2011) for laminar flow through an eccentric annulus with d/D = 0.28 (figure 2.3) for eccentricities greater than 0.5. In the wide gap region for eccentricities less than 0.5, Piot & Tavoularis (2011) found that the critical Reynolds number was independent of gap size.

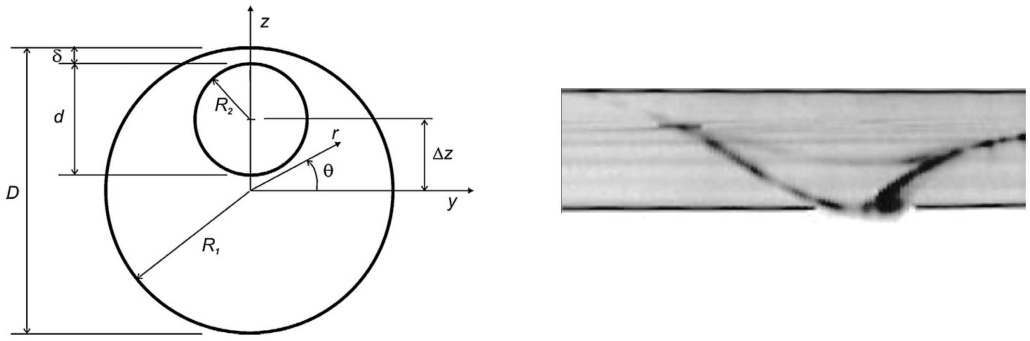

Figure 2.3: Eccentric annulus cross-section (left) and flow visualization across the gap for $e = 0.4$ and Re = 990 (right) (Piot & Tavoularis, 2011).

Gosset & Tavoularis (2006) found that the Strouhal number for the gap vortex streets increased with increased Reynolds number. The authors also found that for configurations having a very narrow gap, viscous forces would obstruct local cross-flow pulsations which have otherwise been observed in configurations having a wider gap for the same value of the Reynolds number; however, low amplitude pulsations were still detected in the wide gap region.

Investigation of momentum and energy transport in wall bounded and central subchannels of a heated 37-rod bundle with a p/d of 1.12 and 1.06 were performed by Krauss & Meyer (1996, 1998). The highest temperature was found in the gap region between two heated rods. Anisotropy of momentum and heat transfer was found to be very large, meaning that the ratio between eddy diffusivities in the radial and azimuthal directions is large, and in both cases, it increased sharply with decreased p/d. Wall shear stress, mean velocity and cross-flow velocity fluctuations had the same distribution in both heated and isothermal flow conditions.

Lexmond *et al.* (2005) investigated fluid transfer between two rectangular sub-channels connected by a narrow rectangular gap, herein referred to as the CPC configuration (figure 1.1-c), using particle image velocimetry (PIV). Streets of alternating vortices were observed with zones of high cross-flow in between. While the vortices were convected at a velocity proportional to the Reynolds number, the overall size of the vortices remained constant. The velocity of the structures was found to be much higher than the superficial velocity in the gap and this velocity, as with the structure size, remained constant even at over three times the Reynolds number. Mass transfer was measured using tracers, and it was found that fluid transfer across the gap was increased by a factor of seven for a Reynolds number increase by a factor of 4. Lexmond *et al.* (2005) proposed a new dimensionless number, ξ, for mass transfer as a result of gap instability and found a strong correlation between it and experimental measurements of mass transfer; the proposed structure mass transfer number relates the residence time of fluid in a structure, the cross flow velocity, and the gap width. A similar study was later performed by Mahmood *et al.* (2009) with a slightly modified cross-section allowing for an adjustable gap height. These authors found that decreasing the gap height from 3 mm to 2 mm resulted in an increase in the velocity of cross-flow fluctuations but a decrease in the mass transfer across the gap.

Silin *et al.* (2008) used time resolved temperature measurements, using a technique proposed by Silin *et al.* (2004) and the experimental setup described by Silin & Juanic (2006); they obtained information on the large-scale pulsations in a rod-bundle

consisting of an outer cylinder and three equidistant inner rods with p/d = 1.205. Measurements were performed at a location downstream where the flow was said to be hydrodynamically developed. Varying the Reynolds number between 850 and 3600 showed a monotonic increase of approximately 10% in the Strouhal number; however, increasing the Reynolds number further, up to 7200, resulted in a slight decrease in St by approximately 6%.

Piot & Tavoularis (2011) showed that the dependence of the Strouhal number on the Reynolds number is linear for a range of small Reynolds numbers; this trend is not expected to hold at higher Reynolds numbers (Möller, 1991); however, the size of the structures was found to be independent of Reynolds number, even at low values of Re (Silin *et al.*, 2008). Piot & Tavoularis (2011) calculated the normalized azimuthal velocity distribution in fully developed annular flow using the exact solution of Snyder & Goldstein (1965) and demonstrated the presence of two inflection points, one on either side of the gap. Inflection points are associated with flow instability, which would explain the clear presence of cross-flow oscillations even at very low values of Re. Additional details on this study are given in section 3.2, which discusses linear stability analysis in eccentric annuli.

In addition to gaps connecting parallel subchannels, Meyer & Rehme (1994) found similar large-scale fluctuations near slots of sufficient depth (1.7 times the thickness). Flow visualisation on channels with two or more closely placed fins and under a wide range of bulk Reynolds number ($2300 \leq \mathrm{Re} \leq 100000$) showed large scale vortices

elongated in the flow direction rotating in the same sense and moving axially through the slot. These vortices appeared abruptly after a certain distance from the inlet and developed to their final form, which was kept roughly constant up to the end of the channel. Using different fluid viscosities (with variation up to a factor of 13) showed no systematic correlation linking viscosity to the characteristic frequency of the large scale structures. The axial spacing of the vortices was found to be between 3 and 6 times the slot depth, with larger spacing being observed for more shallow slots. The spacing was concluded to be exclusively a function of slot geometry and independent of velocity and viscosity in the experimental range. Additionally, in the case of multiple fins, the vortices were found to be synchronized in all the parallel slots; this behaviour is similar to the rod-bundle vortex networks later observed by Krauss & Meyer (1998) and Baratto *et al.* (2006).

2.3 Previous numerical studies

Lee & Jang (1997) attempted to model turbulent flow in closely spaced bare rod arrays by means of solving the Reynolds-averaged Navier-Stokes (RANS) equations using a nonlinear $\kappa - \varepsilon$ model. The authors compared their results with experimental results by Hooper (1984) and Wu & Trupp (1993), and concluded that the azimuthal turbulence could not be simulated by secondary flow as the turbulent convection is caused by large scale motions of eddies. The physics behind these coherent structures was not truly represented by the gradient type model employed in this study and the authors suggested that future studies take these large scale structures into account.

To overcome the limitations of RANS alone in modeling the large-scale structures, Chang & Tavoularis (2005, 2007) employed a method in which unsteady Reynolds-averaged Navier-Stokes (URANS) equations were used to resolve individual very-large-scale motions, whereas turbulence models were used to estimate the small-scale turbulence. The results clearly depicted the counter rotating vortices forming on either side of the gap in the RCR cross-section and in a section of a 37-rod bundle. In the latter case, coherent structures were found to be strongly correlated in the entire rod-bundle as had been observed experimentally (Baratto *et al.*, 2006). URANS was also used by Home *et al.* (2009) to model the CPC configuration and achieved good agreement with the experimental work of Meyer & Rehme (1994), capturing important aspects of the flow such as the pulsations across the gap. Merzari *et al.* (2008*a*) used large eddy simulations (LES) to model the CPC configuration and URANS to model a subchannel of a rod bundle. The authors concluded that LES could predict turbulent mixing phenomena in bare rod arrays and similar geometries if long enough domains were used; however, their application is limited by their large computational power requirement. Their URANS simulations predicted fairly accurately average velocity and turbulence statistics.

Chang & Tavoularis (2008) revisited the RCR channel geometry, this time extending the study to heat transfer across the gap. It was found that the coherent part of the turbulent kinetic energy and temperature fluctuations increased as gap size decreased up to a gap size $\delta/d = 0.01$; below this, no coherent structures could be

established due to the dominating effect of the viscous forces. A critical gap size for each Reynolds number was established for which coherent structure frequency would peak. Beyond this critical value, the frequency would decrease with decreasing δ/d until the gap size becomes very small, where the cross flows would all in all disappear.

Mayer & Hzi (2006), Mayer *et al.* (2007) and Krauss & Meyer (1998) used LES in combination with the lattice Boltzmann method to simulate flow in channels containing a narrow gap and rod bundles. The authors concluded that while the major characteristics of such flows, such as flow pulsations across the gaps, could be reproduced using this method, quantitatively the simulated results deviated from empirical data. Merzari & Ninokata (2009) employed LES in studying the eccentric annulus configuration and found that at low eccentricity stream-wise coherent structures present at low Reynolds numbers were less dominant at higher Reynolds numbers. At eccentricities of 0.5, and in agreement with the DNS study by Nikitin (2006), it was found that a set of four vortices are present in the cross-section of the annulus. At higher eccentricities ($e = 0.8$), four counter-rotating vortices were found in each half domain. At the walls, these secondary flow structures were credited by the authors with the transport of flow from regions of higher momentum in the wider gap, to those of lower momentum in the narrow gap; flow is then transported back to the wider gap in the middle, low shear, region of the annulus.

Various CFD methods were employed by Ninokata *et al.* (2009) at low Reynolds numbers in eccentric annuli and between tightly bound cylindrical arrays. Of most

relevance to our study are the results of DNS and LES simulations on an eccentric annulus with diameter ratio of 0.5 and eccentricity of 0.5. Flow in the narrow gap of the annulus was found to be subjected to local laminarization, although the standard deviations of the cross-flow velocity components were comparable in the narrow and wider gaps. Additionally, stream-wise secondary flow was observed as seen in figure 2.4; this secondary flow is formed at the wall region of the wide gap and is not observed in the narrow gap. Higher eccentricity was found to have a stabilizing effect and delayed transition to turbulence. The authors suggested that turbulence is transported from the wider gap region to the narrow gap by a pair of large scale secondary flow vortices as seen in figure 2.5. The lower stream-wise fluctuation level in the narrow gap was taken to suggest a lower local turbulence production in the gap. Concerning cross-flow pulsations in the narrow gap, the authors found it to be directly connected to the pair of large scale secondary flow vortices and its significance to diminish with Reynolds number increasing up to 26600, at which point the cross-flow becomes insignificant.

Ikeno & Kajishima (2010) used LES to simulate rod bundle flows with three different pitch to diameter ratios. They suggested that the flow contained three-dimensional structures that arose from the same source of the secondary flow of Prandtl's second kind, i.e., stream-wise mean vorticity generated by Reynolds stresses in straight noncircular ducts (Bradshaw, 1987). The authors concluded that the cross flow pulsations observed in other studies were caused by turbulent energy transferred

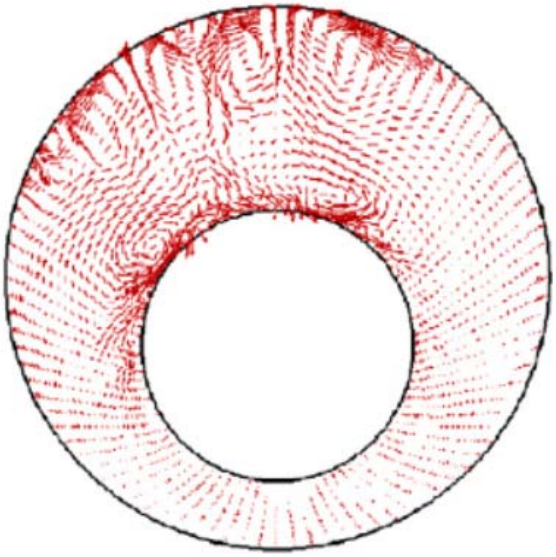

Figure 2.4: DNS results showing secondary flow distribution in eccentric annulus for Re = 12200 and $e = 0.5$ (Ninokata *et al.*, 2009).

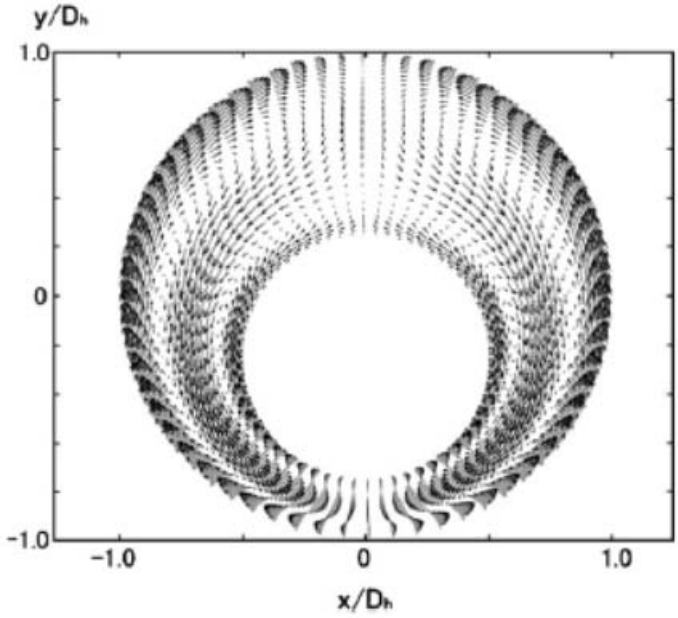

Figure 2.5: Secondary flow distribution obtained by Reynolds averaging of LES results for Re = 12100 and $e = 0.5$ (Ninokata *et al.*, 2009).

from the main flow direction to the wall tangential direction.

A recent article by Chang & Tavoularis (2012) presented three-dimensional unsteady simulations of developing isothermal turbulent flows in an RCR type channel with the intent of investigating the sensitivity of the results to inlet boundary conditions and turbulence models; this study is unlike the majority of discussed works in that it focuses on upstream conditions. A wide range of numerical methods were used, including RANS, URANS, scale adaptive simulations (SAS), improved delayed detached eddy simulations (IDDES) and segregated hybrid simulations, which used SAS for the upstream domain and LES for the downstream one. The authors found that the discrepancy between results obtained by RANS and experimental data was extremely high, and that important flow features were not properly predicted by the RANS method. URANS on the other hand was found to be much more suitable, especially as a first estimate for approximating flows in tightly packed rod-bundles. A clear development length was observed, after which strong cross-flow pulsations built up rapidly across the gap. It was concluded that inlet turbulence specifications did not significantly affect the URANS simulations (see figure 2.6-a,b) and a uniform inlet velocity was found to be preferable to fully developed inlet velocity distributions. SAS and IDDES simulations were also found to be fairly accurate, and both predicted that gap instability would occur faster than had been computed by URANS. A comparison of typical results from different simulation methods is shown in Figure 2.6. These authors concluded that LES was the most suitable as it was able to predict

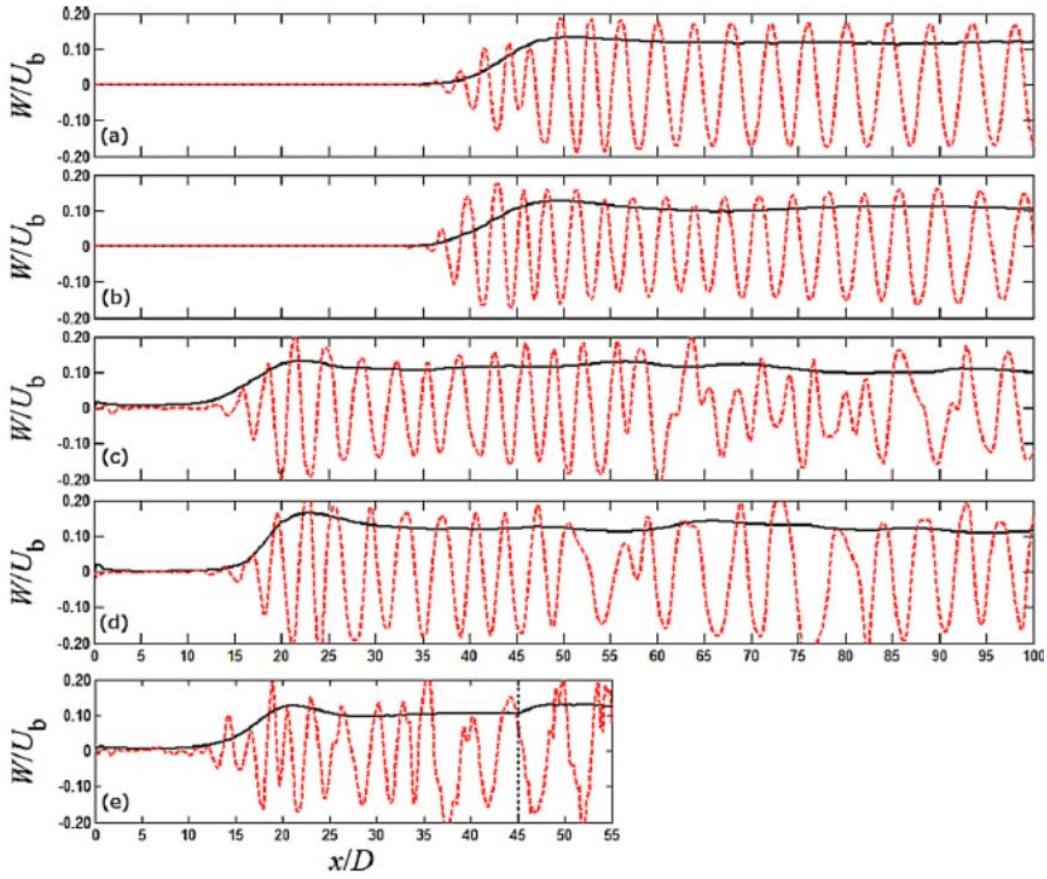

Figure 2.6: Instantaneous stream-wise profile of the cross-flow along the gap centre in an RCR type configuration (dashed line) and standard deviation of local cross-flow fluctuations (solid line) for URANS with RSM-ε (a), URANS with RSM-ω (b), SAS (c), IDDES (d), and the segregated hybrid model (e), (Chang & Tavoularis, 2012).

most accurately the mean flow, turbulence and gap vortex street; the limitation of LES is its significant computational requirements, which allowed simulations to be conducted only in a relatively short domain.

2.4 Objective and scope of the current research

After reviewing the literature we found that there is no experimental study which clearly demonstrates how, in an eccentric annular channel, gap instability is initiated,

how a gap vortex street is formed, and how it develops. There is also no experimental study on the effects of inlet conditions on the flow development and flow structure. Very few studies have focused on gap instability under laminar flow conditions and no significant quantitative experimental studies have been conducted on gap instability in eccentric annular channels over a range of Reynolds numbers which cover laminar, transitional and turbulent flow conditions.

The main objective of this study is to document experimentally the phenomena of gap instability and gap vortex street in eccentric annular channels within ranges of geometrical and dynamic conditions. The documentation of these phenomena will be in sufficient detail so that the results can serve as benchmark data for the validation of future CFD studies on the subject. In particular, the following tasks will be undertaken:

1. Establish on a firm basis our understanding of how gap instability is initiated and how a vortex street is generated and how it evolves.

2. Examine the effects of inlet conditions, inner-to-outer diameter ratio, eccentricity and Reynolds number on the development of the gap vortex street and its characteristics.

Three test-sections were used in the present studies. They all consisted of a cylindrical channel with a diameter D = 50.8 mm and a length of L = 1478 mm, which contained one of three cylindrical cores, so that the three test sections had inner-to

outer diameter ratios d/D = 0.25, 0.50 and 0.75, respectively. The experiments were conducted for Reynolds numbers in the range from 0 to nearly 19000.

Chapter 3

Background

This section will introduce various concepts related to flow instability and transition to turbulence, particularly in annular channels. Because the proposed work is of an experimental nature, this presentation will only be an overview of relevant physical mechanisms without going into mathematical derivations.

3.1 Flow instability, transition and turbulence

Wall-bounded flows are generally more stable due to the constraining of the development of disturbances. However, shear stresses in a boundary layer diffuse outwards due to viscosity, and may under certain conditions create flow instability. The condition at which viscosity changes from a stabilizing factor to a destabilizing one corresponds to a critical Reynolds number Re_{cr}, at which there is a balance between the destabilizing forces of shear and stabilizing viscous forces.

Instability of a laminar flow may under certain conditions be the first step towards transition to turbulence. The vast majority of environmental and technological flows are turbulent. Turbulence is characterized by high rates of mixing and energy dissipation and greatly enhanced mass, heat and momentum transfer. To be considered

turbulent, a flow must have the following characteristics (Tavoularis, 2007):

- Randomness and high levels of disorder
- High diffusivity
- Rotationality and three dimensionality
- Strong dissipative action
- Motions with wide ranges of amplitudes, length and time scales
- Spatial intermittency.

All fluid flows would be laminar if the Reynolds number were lower than a certain limit and they would all become turbulent if the Reynolds number exceeded some other value. A state between laminar and fully turbulent flow is called transition to turbulence. During transition, disturbances act on the laminar flow and build up until the flow becomes turbulent. External forces, including viscous and buoyancy forces, may dampen the disturbances, maintaining the flow in the laminar state. If, on the other hand, disturbances grow in time, then a laminar flow would change state and may eventually become turbulent. Some types of flow may have multiple laminar states, each of which may be stable within a range of conditions, and so it is possible for an instability of a laminar flow to lead to another laminar state rather than directly to turbulence. Moreover, it is possible for a flow to contain turbulent patches, which may exist side by side with laminar flow regions.

3.2 Stability analysis of annular flows

3.2.1 Linear stability analysis

Linear stability analysis is a mathematical procedure, according to which infinitesimally small perturbations are introduced into the equations of motion (i.e., the Navier-Stokes equations for the case of viscous flows), the equations are linearized for the perturbation terms and a set of perturbation equations is derived. The solution of the perturbation equations yields an eigenvalue problem in terms of the wave number and frequency of the introduced perturbation. If the solution is found to grow in time, then the flow is said to be linearly unstable, whereas if the solution is damped, then the flow is said to be linearly stable. Linear stability analyses of flows in annular channels have been presented by Mott & Joseph (1968), Merzari *et al.* (2008*b*), Guellouz *et al.* (2009), and Piot & Tavoularis (2011).

For flows in annular channels with an outer diameter D and an inner diameter d, the bulk Reynolds number is defined as

$$\mathrm{Re} = \frac{U_b D_h}{\nu} \tag{3.1}$$

where U_b is the bulk flow velocity, ν is the kinematic viscosity and the hydraulic diameter is computed as $D_h = D - d$.

In the present study, we shall consider that the term critical Reynolds number for flow in an eccentric annular channel refers to the onset of gap instability, namely the

lowest Reynolds number for which cross-flow oscillations become clearly identifiable in the narrow gap region anywhere along the channel. The lowest Reynolds number at which the process of transition to turbulence is initiated anywhere within the channel will be termed the transitional Reynolds number Re_{tr}. The two concepts, gap instability and transition to turbulence, are distinct and either can be present with or without the other.

3.2.2 Rayleigh's inflection-point theorem

Rayleigh's inflection-point theorem states that the presence of an inflectional velocity profile is a necessary, though not sufficient, condition for instability in inviscid shear flows. According to this theorem, Hagen-Poiseuille flow in a pipe, which has a parabolic velocity profile with no inflection points, would be unconditionally stable in the absence of viscous effects. Flows in concentric annular channels have no inflection points. Linear stability analysis of flows in concentric annuli with different diameter ratios was performed by Mott & Joseph (1968). These authors found that, as the core diameter approached zero, the flow became unconditionally stable to small perturbations, similar to that of Hagen-Poiseuille flow in a circular pipe, whereas as the diameter ratio approached unity, the flow became more like Poiseuille flow in a two-dimensional channel, which is known to be unstable when the Reynolds number exceeds a critical value. For diameter ratios between these two extreme values, Re_{tr} was found to have a monotonic trend, decreasing from an infinite value for $d/D \longrightarrow 0$ to a finite value of approximately 5800 for $d/D \longrightarrow 1$.

Snyder & Goldstein (1965) derived an expression for the dimensionless velocity in laminar, fully developed annular flow as

$$\vartheta = \frac{U}{(c^2/\mu)/(-dp/dx)} \tag{3.2}$$

where c is a length scale dependent on the eccentricity and the diameter ratio; this expression is an exact solution of the Navier-Stokes equations expressed in terms of bipolar coordinates. Fully developed flows in eccentric annuli are found to have a transverse shear layer between the slower flow region in the narrow gap and the faster flow regions in the wide gap. Therefore, the velocity distribution on a transverse plane would have two inflection points, one on either side of the gap. This was illustrated by Piot & Tavoularis (2011) for a fully developed laminar flow in an eccentric annulus with a diameter ratio $d/D = 0.282$ and an eccentricity $e = 0.6$. These authors plotted isotachs of the velocity field obtained from equation 3.2, and the locus of peak velocity inside the annulus (see figure 3.1-left). Then, they demonstrated that the azimuthal peak velocity variation had two inflection points, as shown in figure 3.1-right. This suggests that inviscid flow in this eccentric annulus with the fully developed viscous flow velocity distribution would be potentially unstable (Drazin & Reid, 2004). The maximum dimensionless velocity occurs in the wide gap where it is equal to 1, while the minimum dimensionless velocity occurs at the wall where it is equal to zero. In terms of azimuthal peak dimensionless velocity, the lowest value is found in the narrow gap where it is equal to 0.082.

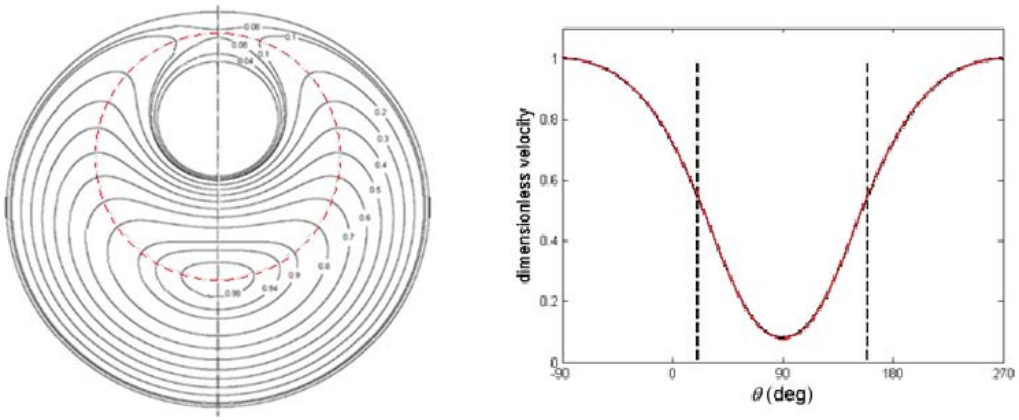

Figure 3.1: Isotachs for d/D = 0.282 and e = 0.6 showing the locus of velocity peaks as a dashed line (left) and dimensionless azimuthal peak velocity distribution in the eccentric annulus (right), (Piot & Tavoularis, 2011).

Merzari *et al.* (2008*a*,*b*) performed a biglobal linear stability analysis on the eccentric annulus and CPC configurations. The authors stated that linear stability analysis is not able to predict instability for pipe flow subjected to infinitesimally small disturbances, and for reasons not fully understood, it over-predicts instability for the annular configuration. Their research suggested that the eccentric annulus configuration was more stable than the concentric one at low eccentricities ($e < 0.3$), as becomes evident by the increase in Re_{tr} with increasing eccentricity; however, the flow becomes increasingly unstable at higher eccentricities due to increased span-wise variation of the velocity. These authors concluded that at low eccentricities the modes of linear instability are masked and not important; however, as eccentricity increases, they become the main cause of instability.

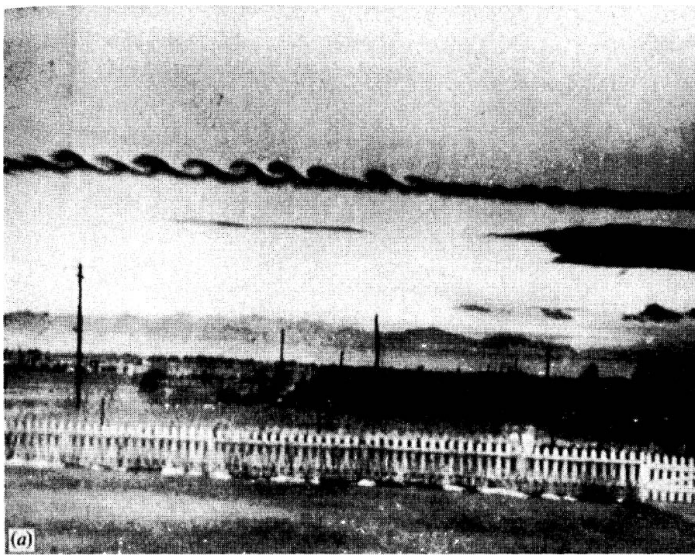

Figure 3.2: Billow clouds near Denver, Colorado, photographed by Paul E. Branstine (Drazin and Reid, 2004).

3.3 Kelvin-Helmholtz instability

The Kelvin-Helmholtz instability is a classical type of flow instability, which originally applied to density stratified shear flows found in the atmosphere (see example in figure 3.2). In this case, the instability arises from an imbalance between the destabilizing effects of inertia and the stabilizing effects of buoyancy.

In the case of shear flows of homogeneous fluids, the Kelvin-Helmholtz instability arises when small disturbances in the region of higher velocity become unstable and cause a roll-up into the lower velocity region (see figure 3.3); the physical mechanism is described in more detail by Batchelor (1967) who considered the idealized case of a vortex sheet (figure 3.4-a) with a sinusoidal disturbance and the special case of the Kelvin-Helmholtz instability when the density of both fluid streams is the same. Instability in this case is connected to the inviscid Rayleigh mechanism, as opposed

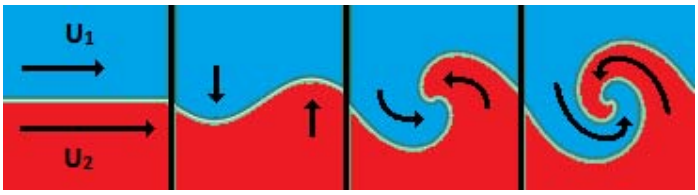

Figure 3.3: Illustration of Kelvin-Helmholtz instability in a mixing layer.

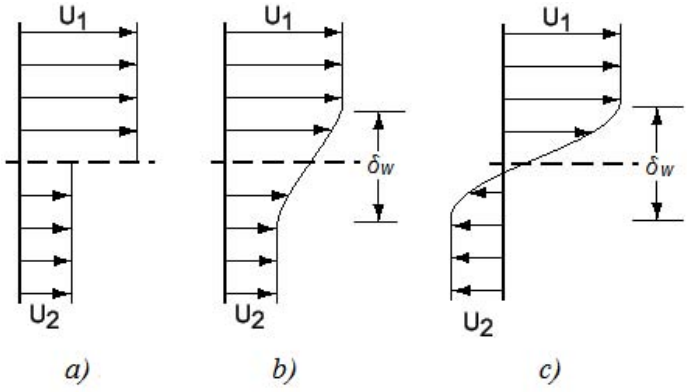

Figure 3.4: Shear flows; (a) vortex sheet, (b) co-flow mixing layer, (c) counter-flow mixing layer.

to viscous instabilities arising from Tollmien-Schlichting instability, which is present in pressure-driven Poiseuille flow (Drazin, 2002).

Drazin (2002) discusses the mathematical procedure for linear stability analysis of shear flow, resorting to the simple case of a vortex sheet in a homogeneous fluid. It is noted that, for this special case, the flow is always unstable and, because waves of all lengths are unstable, there is no length scale for the basic flow. In the case of actual parallel flows, where a velocity gradient is present (figure 3.4-b,c), a shear layer of finite thickness δ_w, also called a mixing layer, will be formed; it can be shown that, for such cases, short waves would be stable; however, at sufficiently high Reynolds numbers, these flows would all become unstable.

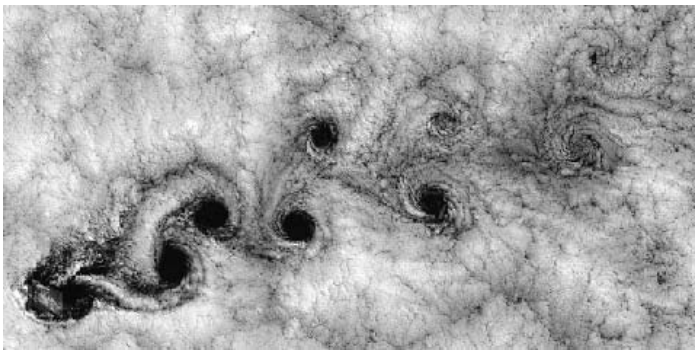

Figure 3.5: von Kármán vortex streets forming past an island off the Chilean coast (NASA).

3.4 von Kármán vortex streets vs. gap vortex streets

von Kármán vortex streets are arrays of counter-rotating vortex pairs shed from a bluff body immersed in a stream. An example is shown in figure 3.5.

The dimensionless frequency of the vortices in a von Kármán vortex street is called the Strouhal number, defined as

$$\mathrm{St} = \frac{fD}{U} \tag{3.3}$$

for which f is the shedding frequency measured in Hz, D is a frontal width of the object and U is the free stream velocity. In the eccentric annulus, where the nominal direction of the flow is parallel to the core cylinder, the shear layer type instability forming about the inflection points on either side of the narrow gap generates quasi-periodic counter-rotating vortex streets which bear close resemblance to von Kármán vortex streets. The generated vortices tend to transport higher momentum fluid from the wide gap region from alternating directions across the narrow gap, corresponding

to the direction of rotation of the vortices. This frequency of the cross-flow can be measured by either simple visualization or velocimetry techniques. A Strouhal number for the gap vortex street in an annular channel can be defined as

$$\mathrm{St} = \frac{fd}{U_b} \tag{3.4}$$

where f is the frequency of the cross-gap oscillations, d is the core diameter, and U_b is the bulk velocity in the channel.

Chapter 4

Apparatus, Instrumentation and Procedures

4.1 Flow loop and test sections

The test section, shown schematically in figure 4.1, is an annular channel with three interchangeable span-wise traversable cores having inner-to-outer diameter ratios of 0.25, 0.50 and 0.75.

The cores are contained in a channel machined from acrylic blocks and 1478 mm (58.2″) long. Its outer surface has a square cross-section with sides equal to 61.0 mm (2.4″), whereas its inner surface is cylindrical with a diameter of 50.8 mm (2.0″). Annular channels are formed by inserting acrylic rods with diameters of 12.7 mm (0.5″), 24.5 mm (1.0″) or 38.1 mm (1.5″). The flow areas A, equivalent pipe diameters

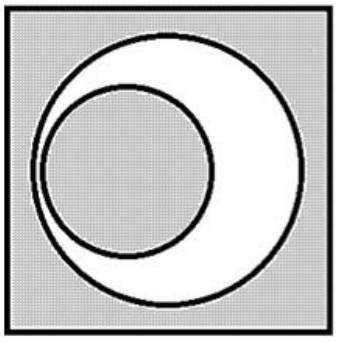

Figure 4.1: Cross sections of an eccentric annular channel.

Test-section	A mm^2 (in^2)	D_{eq} mm (in)	D_h mm (in)
$d/D = 0.25$	1900 (2.95)	24.6 (0.97)	38.1 (1.5)
$d/D = 0.50$	1520 (2.36)	22.0 (0.87)	25.4 (1.0)
$d/D = 0.75$	887 (1.37)	16.8 (0.66)	12.7 (0.5)

Table 4.1: Flow areas, equivalent pipe diameters and hydraulic diameters for test-sections.

D_{eq} for pipes with the same flow area and hydraulic diameters D_h for all test sections used are given in table 4.1.

The test-section is connected to an inlet tank and a discharge tank at its corresponding ends (see figure 4.2). Each tank has a square cross-section 0.254 m in length and a total height of 0.508 m. The inlet tank is partitioned by a vertical plate on which the strong inlet jet impacts and dissipates before the fluid enters the test-section after passing over an overflow and through side grooves. Moreover, the inlet tank is filled with synthetic packing material to suppress inner motions and the flow enters the test-section through a bell-mouth contraction to permit smooth entrance and reduce the chance of flow separation at the inlet. Traversing mechanisms are fastened to vertical walls in each tank to support the rod of each annular channel. A front view of the experimental apparatus showing all relevant dimensions in mm is presented in figure 4.3.

The apparatus is only filled half way with 37.5 liters of a nearly saturated aqueous solution of ammonium thiocyanate (NH_4SCN). The concentration and temperature of this solution are adjusted so that the refractive index of the solution matches precisely that of the acrylic material of the test-section walls. The refractive index of the fluid

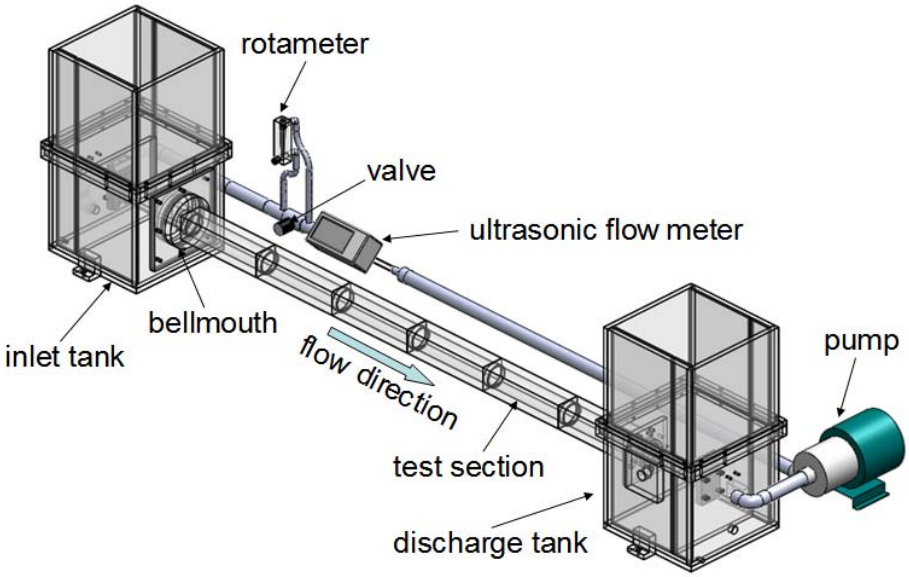

Figure 4.2: Sketch of experimental apparatus.

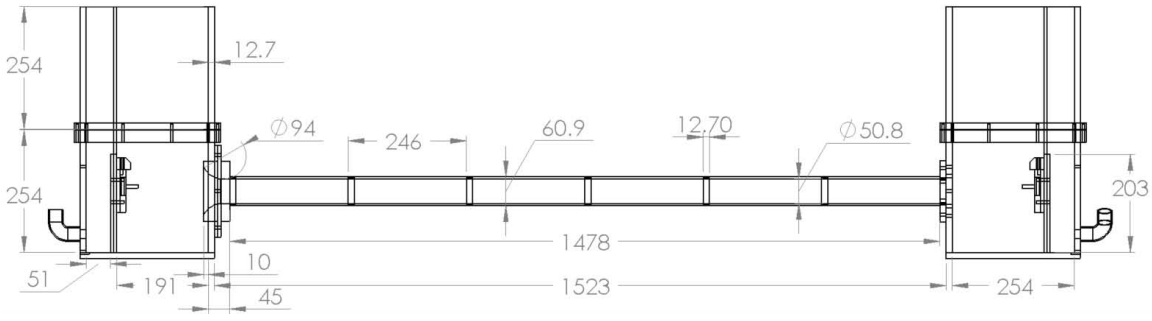

Figure 4.3: Front view of experimental apparatus showing relevant dimensions in mm (sketch shown without the interchangeable core).

was measured at temperatures ranging between 23°C and 45°C using a refractometer (Bausch & Lomb, model ABBE-3L) with a circulating water temperature control block.

Viscosity was measured at temperatures ranging between 18°C and 54°C using a dial viscometer (Brookfield model LVF with a model UL adapter for low viscosity measurements) and later with a calibrated falling ball viscometer (Gilmont Instruments Inc., model GV-2100, size No.1), because the reading on the dial viscometer was on the lower side of its scale. The dial viscometer has an accuracy of ±1% of the full scale range and the possible percentage error is relatively high; approximately 10%. Measurements are reproducible within 0.02 cps in the 0-10 cps range when the UL adapter is attached. The falling ball viscometer on the other hand had a repeatability of ±1%, and it was calibrated using water and tabulated values of viscosity.

The density of the solution was measured using a hydrometer with a range of 1000 to 1220 kg/m^3 having division every 5 kg/m^3 and a scale length of 185 mm (Fisher, model 11522A). Results for the variation of index of refraction, viscosity and density with temperature can be found in section 4.4.1.

The fluid is recirculated through the apparatus by a magnetic-drive pump (Iwaki magnet pump, model MD-70RLT), with its suction connected to the discharge tank and its discharge leading to the flow meter and flow control assembly and then to the inlet tank. The pump motor speed is controlled by a variable transformer (Powerstat, model 3PN116C).

4.2 Instrumentation

4.2.1 Fluid Temperature measurement

A hand-held digital thermometer (OMEGA Engineering Inc., calibrator/thermometer, model CL3512A) was used along with a specially manufactured k-type thermocouple probe having a thin glass exterior and filled with a thermally conductive chemically set cement (OMEGA Engineering Inc., OMEGABOND 600). The thermometer was tested using an ice point reference device and a mercury thermometer and was found to be accurate. Some of the manufacturer's specifications for the hand-held thermometer are as follows:

- Sampling rate: 1 Hz
- Resolution: 0.1 (to 199.9) or 1°C
- Measurement uncertainty: ±(0.1% reading + 1°C) in the range -60 to 1372°C (not including thermocouple error).

Temperature measurements were verified using a glass thermometer (Ever-Safe, Ertco model N16B) with 1°C increments.

4.2.2 Bulk flow velocity measurement

The flow rate in the loop is measured by two separate, calibrated flow meters, each used in a different range. Two transit-time ultrasonic flow meters connected in series (OMEGA Engineering Inc., model FDT-30 and FDT-33) are used to measure the

volume flow rate range between 2 l/m and 375 l/m with an uncertainty of ±1%, whereas a rotameter with a needle valve (King Instruments, model 7530-3-1-2-2C-08), connected in parallel to the ultrasonic flow meter through a valved bypass branch, measures the volume flow rate in the range between 0.3 l/m and 2 l/m with an uncertainty of ±0.179 l/m.

A data acquisition system (National Instruments, model USB-6009), with a ±10 V input, 14-bit resolution and a sampling rate of 48000 samples per second, connected in parallel to a 249 Ohm resistor acting as a shunt was used to acquire the 4-20 mA signal output of the ultrasonic flow meter. No data acquisition was connected to the rotameter, so for very low flow rates, measurements were recorded manually.

4.2.3 Laser Doppler velocimetry

The laser Doppler velocimetry arrangement (see figure 4.4) available for use in this research was a two-component system (Dantec Dynamics S/A, Fiber Flow 2D LDA system, Skovlunde, Denmark). It was powered by an argon-ion laser (Cambridge Lasers, Lexcel 95L-5, Fremont, California) with a continuous-wave power of 5 W. The signal was processed by a burst analyzer processor (Dantec Dynamics, model BSA-F50) using the manufacturer's software package (Dantec Dynamics, BSA Flow software, v4.5). The LDV probe was fitted with an adaptor on which a short-focal distance lens (Yashica 55mm, f1:1.2) was attached, allowing for a smaller measurement control volume than was possible with the lenses provided by the LDV system's manufacturer.

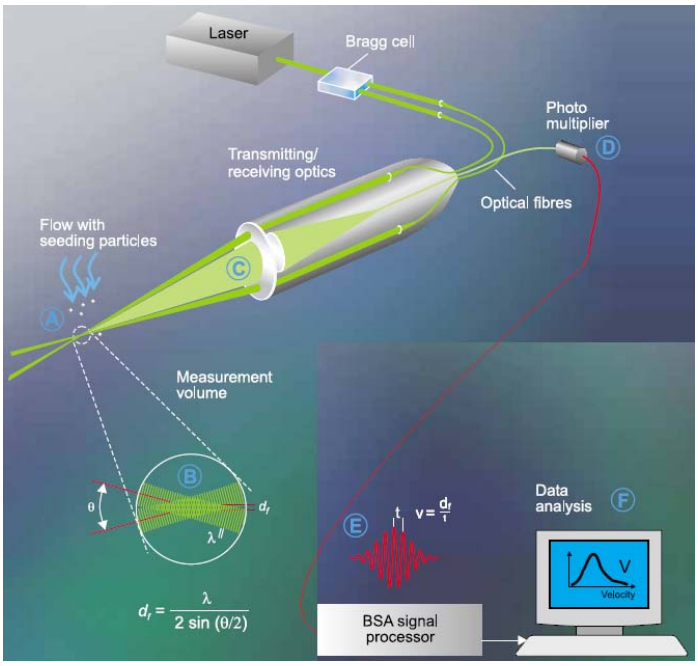

Figure 4.4: Conceptual sketch of LDV system (Reproduced from the Dantec Dynamics brochure).

LDV works by crossing two beams of collimated, monochromatic, and coherent laser light in the flow for which velocity measurements are required. A lens focuses the beams so that they intersect at their focal point where they interfere and generate a set of fringes. As seeding particles pass through the fringes, they reflect light which fluctuates in intensity at the same frequency as the Doppler shift between the incident and scattered light. This frequency is proportional to the velocity of a particle passing through the intersecting beams. The spatial resolution, or measurement volume, of the LDV probe is dependent on the diameter of the laser at its focal point and the angle at which the lasers intersect.

Since a custom lens was used with the LDV probe, the measurement volume must be calculated in order to assess the quality of the flow measurements. The

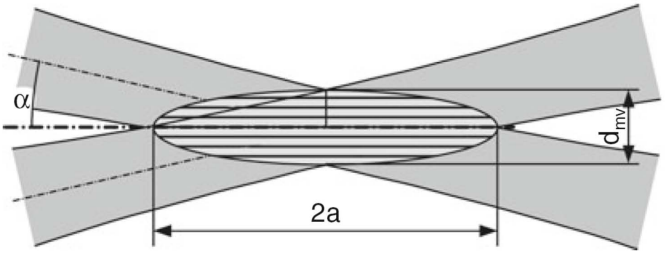

Figure 4.5: Measuring volume and fringe pattern for LDV (Zhang, 2010).

measurement volume can be approximated as an ellipsoid (seen in figure 4.5) which is formed by the intersection of two laser beams having a focused diameter d_{fe} and an intersection half angle α.

The focused beam diameter can be calculated from the focal distance of the lens f_T, the wavelength of the laser λ and the beam diameter d_e using the following equation (Tavoularis, 2005)

$$d_{fe} = \frac{4 f_T \lambda}{\pi d_e} \tag{4.1}$$

The diameter of the measurement volume d_{mv} is calculated from the focused beam diameter and the intersection angle as

$$d_{mv} = \frac{d_{fe}}{cos(\alpha)} \tag{4.2}$$

while the half length a of the measurement volume is calculated using the following equation

$$a = \frac{d_{fe}}{2sin(\alpha)}. \tag{4.3}$$

Velocity direction	λ (nm)	d_e (mm)	α (deg)	d_{mv} (mm)	$2a$ (mm)
Streamwise	514.5	2.2	38.1	0.0165	0.147
Transverse	488.0	2.2	38.1	0.0156	0.139

Table 4.2: Measurement volume of LDV.

The measurement volume would then be

$$volume = \frac{\pi d_{fe}^3}{6\,\cos(\alpha)\,\sin(\alpha)}. \tag{4.4}$$

The calculated dimensions of the LDV measurement volume using the 55 mm lens are presented in table 4.2.

To take velocity measurements in the cavity of the acrylic test-section, the beams of the LDV must pass from air, which has an index of refraction of 1.0008, through the acrylic test-section, having an index of refraction of 1.491, and finally through the ammonium thiocyanate solution, with matching index of refraction. This will cause a shift in the position of the measurement volume, as well as a change in the wavelength and angle of the intersecting beams (see Figure 4.6). The intersection angle between the two refracted laser beams is calculated by Snell's law and found to be 25.6°, while the variation in the wavelength is given by the following equation (Zhang, 2010)

$$\lambda_2 = \frac{n_1}{n_2}\lambda_1 \tag{4.5}$$

where n_1 and n_2 are the indices of refraction of the two media, and λ_1 and λ_2 are the respective wavelengths of the laser beam in the same two media. Using the small angle

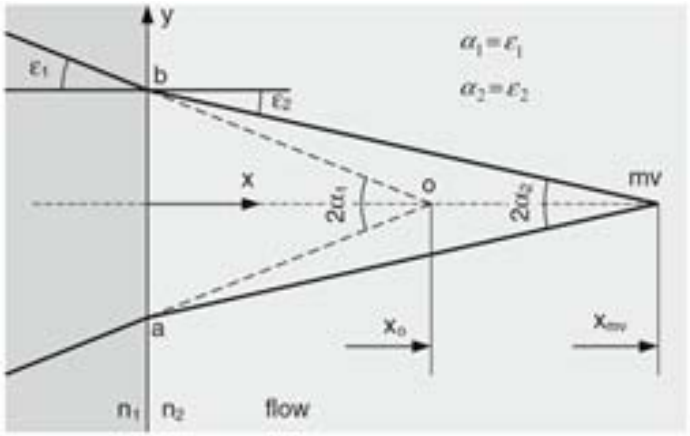

Figure 4.6: LDV laser bean passing from one medium to another (Zhang, 2010).

approximation and Snell's law, one can approximate the position of the measurement volume with respect to the test-section wall x_{mv} as

$$x_{mv} = \frac{n_2}{n_1} x_o \tag{4.6}$$

where x_o is the virtual beam intersection position in a uniform medium. Zhang(2010) shows mathematically that the fringe spacing, which is used to calculate the velocity, remains unchanged, as long as the LDV axis is perpendicular to the test-section wall as shown in figure 4.6, and this remains true irrespective of the number of media the LDV laser beams pass through. Additionally, for two-dimensional LDV measurements, requiring two intersecting pairs of beams of different wavelengths, Zhang (2010) shows that the optical dispersion is negligible.

4.2.4 Particle image velocimetry

The LaVision (Ypsilanti, MI, USA) planar Particle Image Velocimetry (PIV) system components and operation are illustrated in figure 4.7. It consists of a double pulse Nd:YAG laser (New Wave Research, Solo PIV 120XT, Fremont, California, USA) with an attached sheet generator (LaVision Inc., model 1108405), which is synchronized with two digital cameras (LaVision Inc., Imager ProX 4M), each with a resolution of 2048×2048 pixels, by a programmable timing unit (LaVision Inc., model 1108058). Attached to the cameras are 50 mm Nikon lenses with add-on interference filters tuned to the 532 nm wavelength of the laser (LaVision Inc., model 1108501). The PIV system is capable of acquiring images at a maximum frequency of 7.24 Hz.

PIV works by taking two consecutive images of particles illuminated by a laser sheet and uses software to determine the relative displacement of particles in the flow, thus giving a velocity field. In the case of stereoscopic PIV, two cameras are used to look at the laser illuminated sheet at an angle; the images are then processed to provide a three-dimensional velocity field.

4.3 BSA Flow software

After considerable time spent using MATLAB to generate auto-correlations and power spectra from raw LDV data, it was concluded that the BSA Flow software which comes with the LDV system is more than capable of generating such plots and has several key features which allow us to modify how data is analyzed. The program automatically

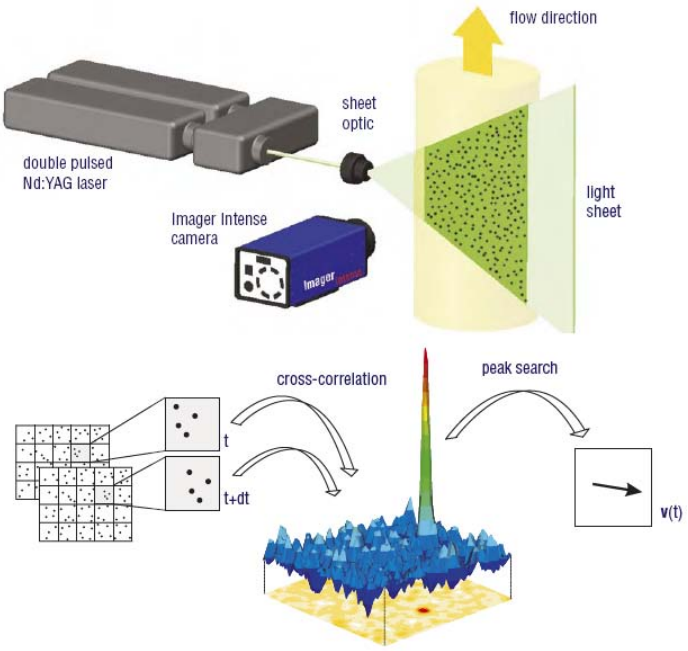

Figure 4.7: Conceptual sketch of a planar PIV system (Reproduced from LaVision Inc. brochure).

resamples the raw data when generating power spectra and has features which allow for ensemble averaging (referred to as blocking) and filtering. While all this can be done in MATLAB, whose functions allow for increased control over the analysis, we used mostly the BSA Flow software to generate all the histograms, auto-correlations and spectral plots.

4.3.1 Resampling

Due to the nature of the LDV measurement process, velocity is obtained at random intervals (when a seeding particle passes through the LDV's intersecting beams). However, frequency analysis using Fast Fourier Transforms requires samples which are equally spaced in time. As a result, we need to resample the raw data and one

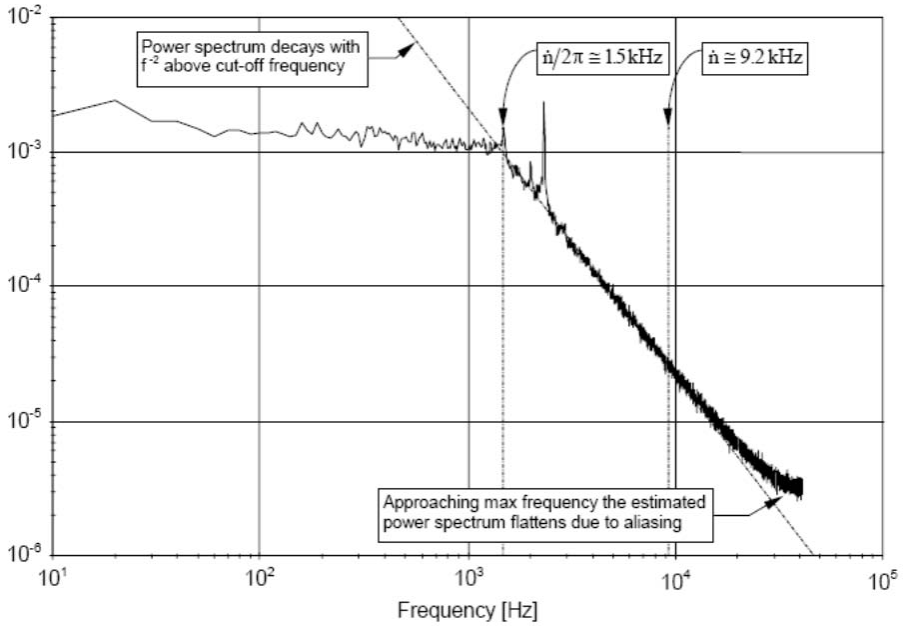

Figure 4.8: Effect of sample and hold on the power spectrum (BSA Flow software manual, Dantec Dynamics).

method of doing this is using the sample-and-hold technique. Determining a proper resampling rate is a challenging task.

It is important to note that using the sample-and-hold method will impose a first order low-pass filter (known as a particle rate filter) with a cut-off frequency equal to the mean data rate divided by 2π. As a result, attenuation at the high-frequency components of the signal will occur above the cut-off frequency, and the power spectrum estimate will be attenuated by a factor proportional to f^{-2}. Figure 4.8 shows the effect of using the sample and hold technique on the power spectrum. It is important to be aware of this attenuation as it can be confused with the Kolmogorov turbulence spectrum law which decays with $f^{-5/3}$.

4.3.2 Blocking and filtering

The Fast Fourier Transform method used to estimate spectra requires raw data to only cover a time-span corresponding to half the reciprocal of the desired frequency resolution (BSA Flow software manual, Dantec Dynamics). When a large number of samples is gathered, the raw data can be divided into several blocks which all meet the aforementioned requirement. The final spectrum estimate will be the average of all estimates generated from the data blocks. This is commonly known as ensemble averaging. The number of samples in each block should be an integer power of 2, and the software's maximum limit is 65536 samples per block. For the best resolution it is recommended to have the maximum samples per block; however, there should be a balance between the resolution of each ensemble member and the number of members to be averaged. Ideally sets of raw data would contain 6553600 samples; however, this could take many hours depending on the seeding. Therefore, based on each set of measurements and the sampling frequency of that particular case, a judgment must be made as to which setting will produce the best results. This decision would take into account an estimate of the time scale of the large scale structures we are trying to identify as well as the sampling frequency and convective velocity of the structures.

After generating the power spectrum, artefact peaks must be filtered out. Having a large number of blocks to average does help; however, if we are limited by the number of blocks, further filtering (or frequency smoothing) may be needed. The BSA Flow software offers four options for filtering: no filter, Box filter, Hanning filter

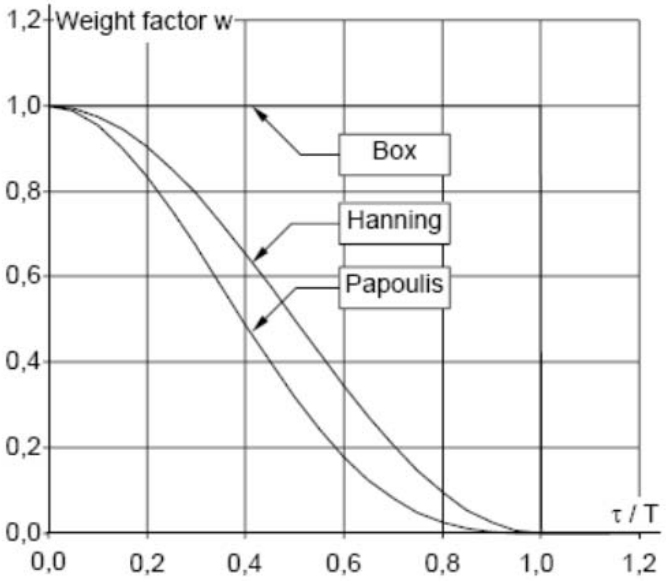

Figure 4.9: Weighting factors used for filtering (BSA Flow software manual, Dantec Dynamics).

and Papoulis filter. To reduce calculation time, filters are implemented using Fast Fourier Transform techniques. A graph of each filter weight factor can be seen in figure 4.9. Having experimented with the different filtering types, we found that the Hanning filter best suited our needs.

4.4 Experimental procedures

4.4.1 Fluid physical properties

Temperature measurement

The Reynolds number was found to be highly dependent on temperature, mainly due to the large variations of viscosity brought on by small variations in temperature.

The temperature of the ammonium thiocyanate solution circulating through the test-section was found to be dependent on several factors; the room temperature, the setting of the variable transformer and the control valve positions used to control the volume flow rate through the test-section, the upstream and downstream mesh density, the core diameter and the eccentricity of the core relative to the test-section and finally, the length of time the fluid has been circulating with all other variables being the same. With all these factors weighing in, it was impossible to achieve a constant temperature for all the experiments being performed, therefore a 100 watt aquarium heater with an adjustable temperature controller was placed in the discharge tank to moderate the temperature variations. Temperature measurements were read manually using a digital thermometer with a specially manufactured thermocouple probe (see section 4.2.1) being placed in the discharge tank and entered into the same LabVIEW program which was used to record the flow meter volume flow rate thus allowing the program to automatically calculate and record the Reynolds number.

Refractive index measurement and matching

Using a refractometer (Bausch & Lomb) with the built-in water block, several refractive index measurements were taken at different temperatures. To avoid erroneous measurements due to evaporation of water from the tested specimens, the tested sample was changed periodically. Figure 4.10 shows the variation of refractive index with temperature. For a temperature change of 22°C, the index of refraction changes by 0.0095. The refractive index of the ammonium thiocyanate solution in the apparatus

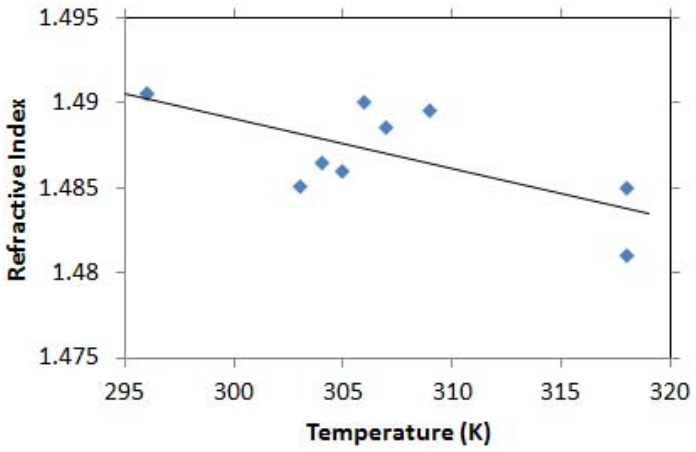

Figure 4.10: Refractive index variation of ammonium thiocyanate with temperature.

was periodically checked to make sure it had not changed (mostly due to evaporation); the target refractive index was 1.491. In the event that the refractive index had increased beyond this value, a controlled amount of water was added to the solution to bring it down; in general for 40 l of solution, adding 200 ml of water decreased the refractive index by 0.001. If too much water was added, the refractive index could be increased by dissolving more ammonium thiocyanate salt into the solution.

Viscosity measurement and temperature dependence

Noting a strong dependence of viscosity on temperature, preliminary experiments were conducted to obtain a relationship between the two; this relationship would be used as a correction factor for all future experiments where temperature is recorded. Two methods were used to measure the viscosity. The first was using a dial viscometer, for which beakers were filled with ammonium thiocyanate and cooled or heated in a reservoir of water before each viscosity test. The dial viscometer UL adapter and

spindle were submersed in the pre-heated/cooled beaker and left for several minutes in order for their temperature to match that of the solution. Because no constant temperature bath was available, the fluid temperature along with that of the UL adapter and spindle slowly shifted toward room temperature. Temperature measurements were taken before and after viscosity measurements and recorded along with the accompanying viscosity measurement. Generally, three measurements were performed in sequence 30 seconds apart at each temperature. To verify the viscosity measurements, a calibrated falling ball viscometer was used; the viscometer was submerged in a temperature controlled water bath and left for several minutes for its temperature to adjust to that of the bath; following this, a minimum of three concurrent measurements were taken for each temperature. Additionally, it was found that more consistent measurements could be obtained by tilting the falling ball viscometer at an angle of 15°, effectively making it a rolling ball viscometer. Figure 4.11 shows the viscosity measurements for NH_4SCN using the aforementioned viscosity measurement techniques in addition to the calibration measurements for the rolling ball viscometer using water.

Density measurement and temperature dependence

The density of the ammonium thiocyanate solution was measured and found to be approximately constant for the temperature range of interest in our experiments (see Figure 4.12). A correction (0.2T(°C) - 4) to the hydrometer reading was made to account for temperature variation as the hydrometer was calibrated at 20°C. At 31.5°C,

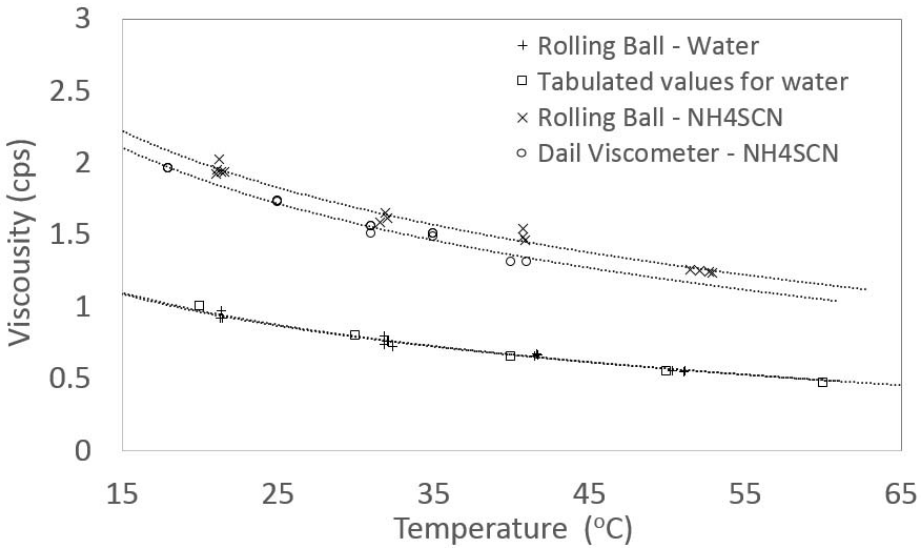

Figure 4.11: Viscosity versus temperature for NH_4SCN.

the density was found to be 1137 kg/m^3.

4.4.2 Mass flow rate

The majority of experiments conducted had a volume flow rate greater than 2 l/min, with few exceptions, therefore the OMEGA Series FDT-30 and DFT-33 were used most often. Initially, the FDT-30 was used; however, due to its narrow flow tube, it was found to restrict the flow to Reynolds numbers less than 10000, so the FDT-33 was installed along with a bypass loop to allow for higher flow rates. In the majority of recorded measurements, either the FDT-30 or FDT-33 were connected to the National Instruments model USB-6009 data acquisition system. Using LabVIEW the acquired flow meter readings were averaged across 15 second windows and this average was logged along with the time, fluid temperature, calculated Reynolds number and various other experimental notes. The average mass flow rate, or more importantly,

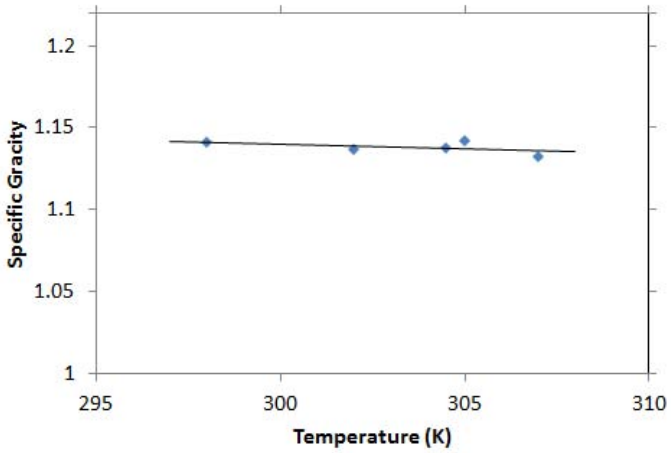

Figure 4.12: Density variation of ammonium thiocyanate with temperature.

Re, was taken to be the average of all recorded readings.

The OMEGA Series FDT-30 and FDT-33 readings were found to be sensitive to fluid temperature; therefore corrections had to be made to the recorded data. The King Instruments rotameter reading was not found to be as sensitive to temperature, so its reading, with corrections for specific gravity, was used as a lower bound in assessing the ultrasonic flow meter correction faction. The rotameter correction factor is as follows

$$\text{correction factor} = \sqrt{\frac{(\text{specific gravity of float} - 1) \times \text{specific gravity of fluid}}{\text{specific gravity of float} - \text{specific gravity of fluid}}} \quad (4.7)$$

For higher velocity ranges, the LDV probe was used to take vertical and horizontal velocity measurements across a downstream part of the test-section for various mass flow rates and temperatures; the flow profiles were then integrated and an average

mass flow rate was assessed. This average mass flow rate was then compared to the reading given by the ultrasonic flow meter and a temperature based correction factor was established. The FDT-30 output was found to be less sensitive to temperature than that of the FDT-33; the two corrections are as follows;

$$\text{FDT-30 Correction (GPM)} = 0.0152\ \text{T}(^{\circ}\text{C}) - 0.3375 \tag{4.8}$$

$$\text{FDT-33 Correction (GPM)} = -0.0865\ \text{T}(^{\circ}\text{C}) - 3.5953 \tag{4.9}$$

Setting of the mass flow rate is achieved by two methods: first by adjusting the various valve combinations on the apparatus, and second by varying the voltage of the variable transformer connected to the pump. The latter method was employed more often as the ball valves on the apparatus cannot be precisely set, so they are often left either completely open or completely closed. For fine adjustments, the needle valve on the rotameter was used. Since it is often desirable to try to match the Reynolds number, the LabVIEW program connected to the ultrasonic flow meters is monitored after each adjustment, and the flow rate is tracked over several minutes to ensure it has stopped changing. In general, it takes about 2 minutes for the flow in the loop to stabilize after each adjustment; however, since the temperature of the fluid is sensitive to any change done to the loop, the flow is often found to slowly creep away from the desired setting. This creep could be as high as 10% after one hour; therefore periodic adjustments need to be made for extended measurement sets.

4.4.3 Rod positioning and eccentricity

To align the core rod in the test-section and set its eccentricity, the following procedures were followed:

- The point where the four laser beams of the LDV meet is used as a reference during this procedure; a 40X microscope is used to zoom in and more accurately determine the relative position between the reference point and solid boundaries.

- The LDV probe is mounted on a traverse which moves parallel to the test-section. The LDV laser is positioned so that it intersects the outside vertical surface of the test-section at a single point; this point is then traversed horizontally along the test-section to insure that the traverse is in fact parallel to the test-section.

- Adjustments are made to the table carrying the test-section as the traverse is moved back and forth to insure proper alignment; the procedure is similar to alignment of a part to be machined on a mill.

- The carrier which holds the LDV probe is then moved toward the test-section by means of a precision dial marked every 0.0254 mm of traverse, which advanced the probe 5.08 mm per rotation. From Snell's law and the refractive index of the acrylic, the position of reference laser point in the test-section can be calculated relative to the traversed position of the probe. The reference point is moved such that it would intersect the outer wall of the core when the core

is positioned at a certain eccentricity.

- The reference point is moved horizontally to ensure that the core axis is parallel to that of the outer cylinder and properly aligned horizontally.

- A cathetometer is used to check the vertical alignment of the core as the acrylic can bow over time. The inner rod is then rotated until the vertical alignment is satisfactory, and the horizontal alignment is rechecked once more.

4.4.4 Local and traversing LDV measurements

After positioning the core to a desired eccentricity the flow velocity is adjusted and the LDV measurement volume is positioned in the desired location; usually the center of the narrow gap. The LDV probe is traversed back and forth horizontally and with the help of a 40X microscope, and the positioning and alignment are verified for a final time. The sampling rate is verified in the Dantec BSA Flow software (v4.5) and if it is found to be less than 200 kHz, additional seeding is added. The seeding is in the form of hollow glass spheres with a mean diameter of 11 μm (Potters Industries, Blacksburg, Virginia; Sphericel® 110P8 Hollow Glass Spheres). To add seeding, approximately a tablespoon of hollow glass spheres is added to 50 ml of ammonium thiocyanate solution and shaken vigorously, the seeded solution is then gradually added to the discharge tank. Alternatively, the meshing in the discharge tank and the inlet tank could be disturbed which would release trapped seeding particles added over time. Once properly seeded, the mass flow rate is monitored to ensure it is no

longer changing.

For local measurements, the LDV horizontal position is set either using pre-set positioning screws located on the traverse railing, or using a custom cut measuring tape which extends the length of the test-section. The measuring tape has standard metric/imperial marking and uses the end of the bell mouth inlet as the reference zero position. The LDV probe carrier is moved until the vertical LDV laser beams intersect the measuring tape at the desired downstream distance.

For traversing measurements, the LDV probe carrier is positioned near the inlet of the test-section and is connected to a pulley on either side of the traverse railing by means of a tensioned steel aircraft cable. To one of the pulleys is connected a gear reducer which is in turn connected to a variable direction/speed motor. The traverse speed is measured by changing the voltage to the motor and timing the displacement of the traverse. To verify that the velocity of the traverse is constant along the entire test-section, periodic position measurements were taken.

Once all settings are verified, simultaneously the recording on the BSA Flow software and the LabVIEW mass flow rate logging software is initialized, and in the case of traversing measurements, the traverse motor is engaged. Recording is stopped either when an allocated time has passed, or when the carrier has reached the end of its traversable distance.

4.4.5 Planar PIV velocity maps

The first step in conducting PIV measurements is to clean and lightly polish the test-section. The test-section core is then aligned to the desired eccentricity (see section 4.4.3). The pulsating laser sheet is then made to pulsate at a high frequency but with low intensity so that it can be visually inspected and aligned parallel to the desired measurement plane. Following this, the laser sheet is moved vertically or horizontally so that it lies in the desired measurement plane. With the laser sheet still pulsating rapidly, two PIV cameras placed side-by-side (to increase the measurement area without sacrificing resolution) are turned on and their focal planes are adjusted so that particles in the laser sheet are clearly visible and sharp.

PIV measurements usually start with the Reynolds number being set and the system allowed to run for at least an hour in order to allow its temperature to reach equilibrium. Following this, traversing LDV measurements (see section 4.4.4) are conducted to record the various stages of flow development and their locations; then stationary LDV measurements are conducted near the end of the test-section so statistical information on the flow can be attained. Finally, PIV measurements are taken for each of the six acrylic blocks in the test-section.

4.4.6 Stereoscopic PIV velocity maps

Before any stereoscopic PIV measurements could be conducted, the PIV cameras needed to be focused and aligned and a calibration of the stereoscopic field needed to

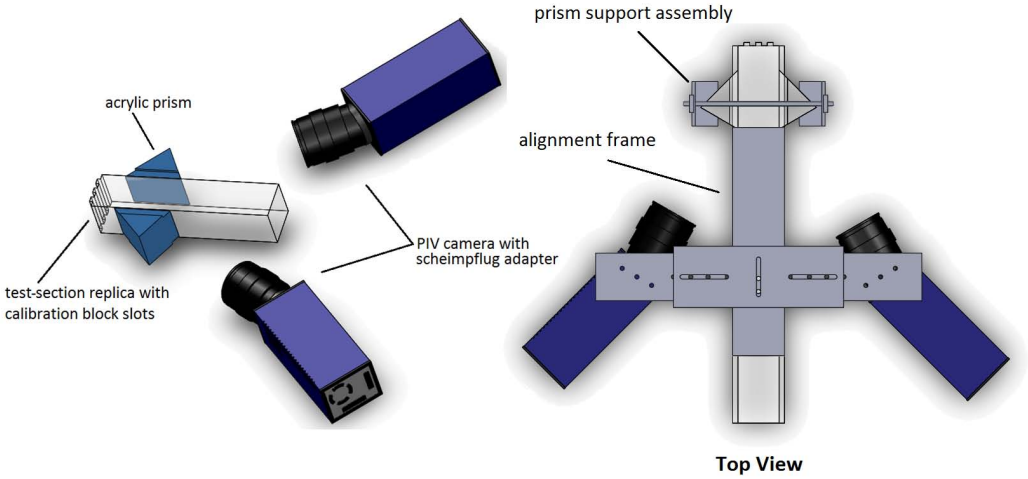

Figure 4.13: Stereoscopic PIV calibration setup.

be conducted. To do this an acrylic block having the same cross-sectional dimensions as the test-section was machined, and at one of its ends grooves were slotted to accommodate a LaVision calibration plate (LaVision Inc., 3D calibration plate, type 22). An alignment frame was constructed to hold the cameras at a fixed angle so that the calibration field would be the same when the setup was transported to the actual test-section. The PIV cameras were each equipped with a Scheimpflug adaptor in order to have a focused image while pointing at the test-section from an angle. Two acrylic prisms were also constructed to correct for image distortions. Figure 4.13 shows a stripped-down version of the calibration setup (left) and a top view of the full calibration setup (right).

Once the PIV setup was calibrated, the alignment frame with the mounted cameras and the acrylic prisms was moved to the test-section. Vegetable oil was placed between the acrylic prisms and the test-section to remove air between the two surfaces

which would otherwise lead to reflections due to the angle at which the cameras were pointing and the large difference between the refractive index of air and acrylic.

After setting the eccentricity as described in section 4.4.3, and aligning and focusing the PIV cameras, the following procedures were followed for each stereoscopic PIV measurement:

- A traversing LDV measurement was conducted as described in section 4.4.4 to determine the positions at which i) there was no strong cross-flow in the gap region, ii) the cross-flow in the gap region started to build up, and iii) the cross-flow reached full strength.
- A stationary LDV measurement was conducted at a far downstream position where the flow was found to be developed.
- A stereoscopic PIV measurement set (up to 5000 image pairs) was recorded at the same aforementioned downstream location.
- Another local LDV measurement was conducted at the same location to verify that the conditions had not changed.
- A stereoscopic PIV measurement was then near the inlet of the test-section, and another in the developing region.
- A stationary LDV measurement was taken at the inlet of the test-section.

Chapter 5

Results

This chapter consists of two manuscripts intended for publication in journals. In the first manuscript, we examined in detail a representative paradigm of a flow in a highly eccentric annular channel. The intent was to establish on a firm basis our understanding of how gap instability is initiated and how a vortex street is generated and evolves. In the second paper we presented additional measurements, which document the dependence of flow in eccentric annular channels on the inlet conditions, diameter ratio, eccentricity and Reynolds number.

5.1 Flow structure

The manuscript that follows, entitled "Experimental investigation of flow development and gap vortex street in an eccentric annular channel. Part 1. Overview of the flow structure" is an appended form of that submitted for publication in the Journal of Fluid Mechanics on November 18, 2013.

Experimental investigation of flow development and gap vortex street in an eccentric annular channel. Part 1. Overview of the flow structure

George H. Choueiri[1] **and Stavros Tavoularis**[1]†

[1]Department of Mechanical Engineering, University of Ottawa, Ottawa, ON K1N 6N5, Canada

(Received ?; revised ?; accepted ?. - To be entered by editorial office)

Flow visualization, laser Doppler velocimetry and planar and stereoscopic particle image velocimetry were used to investigate the isothermal velocity field along an eccentric annular channel with a diameter ratio of 0.5 and an eccentricity of 0.8 for a Reynolds number of 7300. Observation of the flow development has identified three distinct regions: the entrance region, the fluctuation-growth region and the rapid-mixing region. Weak quasi-periodic velocity fluctuations were first detected in the downstream part of the entrance region, and grew into very strong ones, reaching peak-to-peak amplitudes in the narrow gap that were nearly 60% of the bulk velocity. Two mixing layers were identified on either side of the gap, which generated a street of counter rotating vortices and thorough large-scale mixing of the fluid in the channel.

Key words: eccentric annular channel, annular flow, gap instability, gap vortex street

1. Introduction

Fluid flow and heat and mass transfer in concentric and eccentric annular channels have been investigated extensively for several decades. Besides the inherent interest in the intriguing phenomena that occur in such channels, motivation has been also provided by the need to describe and predict flow and transport characteristics in the many technological and natural systems that contain annular and other compound channels. Examples of the latter include nuclear reactor rod-bundles, oil-drilling wells, double-pipe heat exchangers, inundated rivers and catheterized arteries. Among the early analytical studies, notable is the derivation of an exact solution for fully developed laminar flow

† Email address for correspondence: stavros.tavoularis@uottawa.ca

in annular channels with arbitrary eccentricity by Snyder & Goldstein (1965). Mott & Joseph (1968) presented a linear stability analysis of parallel flow in concentric annuli subjected to axisymmetric disturbances and predicted that the critical Reynolds numbers for flow instability would be of the order of 10^4, which is much larger than values at which transition to turbulence would likely occur. More recently, Merzari *et al.* (2008) conducted a global linear stability analysis of laminar flows in eccentric annular channels and concluded that the most unstable eigenmodes corresponded to the azimuthal variation of the velocity distribution. Many experimental and computational studies of both laminar and turbulent flows in such systems have been conducted since then, which have documented several aspects of momentum, mass and heat transfer. In the case of turbulent flows in eccentric annuli, one of the topics of interest has been the formation of secondary flows of Prandtl's second kind, which are similar to those generated in turbulent flows in rectangular ducts and have been attributed to turbulence anisotropy (Kacker 1973; Nouri *et al.* 1993; Nikitin *et al.* 2009). Such secondary flows result in large-scale mixing across the channel, but they are very weak, with magnitudes reported to be of the order of 1% of the axial flow velocity. Nevertheless, under certain conditions, and for both laminar and turbulent flows in highly eccentric annular and related geometries, there exists another, much stronger, mechanism that is capable of large-scale transport across the channel cross-section. This mechanism has been known for a long time in the nuclear reactor thermalhydraulics research community. A thorough historical overview of early misconceptions and the recognition of the nature of this phenomenon has been presented by Meyer (2010) (see also Rehme 1992). Flow in channels containing narrow gap regions along the flow path and flanked by wider subchannels are prone to a particular type of instability, recently termed gap instability, which leads to the formation of a gap vortex street (Tavoularis 2011). According to the idealized model of this vortex street, as proposed by Meyer & Rehme (1994) and presented in figure 1, pairs of staggered vortices of alternating rotational direction are formed on either side of the narrow gap, in a manner that is analogous in some ways to the von Kármán vortex street. The result of cross-gap flows induced by these vortices is a greatly enhanced inter-subchannel mixing, and an increase in cross-gap heat and mass transfer. In the case of a tightly-packed rod bundle, which contains multiple interconnected subchannels, the individual vortex streets that would form near each narrow gap would be coupled and would form a rod bundle vortex network (Tavoularis 2011). Experimental studies of cross-gap flows in rod bundles

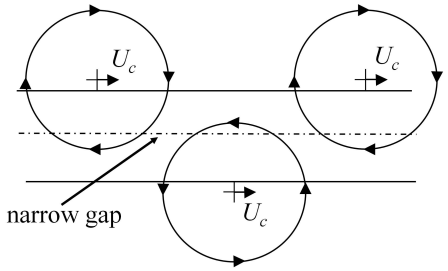

Figure 1: Sketch of an idealized gap vortex street, according to Meyer & Rehme (1994).

include those by Rowe *et al.* (1974), Hooper & Rehme (1984), Möller (1991), Krauss & Meyer (1996, 1998), Baratto *et al.* (2006) and Silin *et al.* (2008). Most of the published literature on the topic of cross-flows in gaps is concerned with relatively large Reynolds number flows, in which the flow is fully turbulent (Wu & Trupp 1993; Meyer & Rehme 1994; Guellouz & Tavoularis 2000a,b). The two previous experimental studies of laminar, and possibly transitional, flows in annular channels (Gosset & Tavoularis 2006; Piot & Tavoularis 2011) were based on flow visualization and did not report details of the velocity field or the development of gap instability and vortex street. Relevant measurements in square channels connected by a narrow gap have also been conducted (Lexmond *et al.* 2005; Mahmood *et al.* 2009); these covered a range of Reynolds numbers between 800 and 20,000. It is noted that, in the experimental studies, flow instability was observed to occur at Reynolds numbers that were significantly lower than the critical value of approximately 7000 predicted by Merzari *et al.* (2008).

The general objective of the present research is to document in detail the patterns of flows developing in eccentric annular channels under laminar, transitional and turbulent flow conditions and their dependence upon the Reynolds number, the eccentricity, the inlet conditions and the inner-to-outer diameter ratio. The results will be presented in two contiguous articles. In the present Part 1, we will examine in detail a representative paradigm of a flow in a highly eccentric annular channel. This is intended to establish on a firm basis our understanding of how gap instability is initiated and how a vortex street is generated and evolves. The choices of geometry and Reynolds number for the presented case were such that the phenomena of interest would be unambiguously present and in full strength: the diameter ratio was 0.5, the eccentricity was 0.8 and the Reynolds number was approximately equal to 7300. The choice of such a relatively low Reynolds number was made so that the flow would be turbulent, but at conditions that would be

accessible to numerical analysis with the use of direct numerical simulation and large eddy simulation techniques, for the validation of which these results can serve as a benchmark. In a future Part 2, we will present additional measurements, which will document the dependence of flow in eccentric annular channels on the Reynolds number (in the range from essentially zero to nearly 20,000), the eccentricity (in the range from 0 to 0.9), the inlet conditions (for several levels of disturbances at the inlet) and the inner-to-outer diameter ratio (in the range from 0.25 to 0.75). Gap instability and gap vortex streets are fascinating and complex flow phenomena with potential for beneficial application in diverse engineering and natural systems. We hope that the present work will expose their significance to the wider fluid mechanics research community.

2. Experimental facility and procedures

2.1. *Apparatus and instrumentation*

The experiments were conducted in a recirculating flow loop, shown in figure 2. The annular test section had a length $L = 1478\,\mathrm{mm}$ and consisted of two parts: an outer part, machined and polished from acrylic blocks to a square outer surface with sides equal to $60.5\,\mathrm{mm}$ and a cylindrical inner surface with a diameter $D = 50.8\,\mathrm{mm}$; and a core, consisting of a cast acrylic rod with a diameter $\mathrm{d} = 25.1\,\mathrm{mm}$, which was suspended at its two ends on horizontal traverses that were mounted inside the inlet and outlet tanks, away from the test section ends. Thus, the annular test section had a diameter ratio $d/D \approx 0.50$, a hydraulic diameter $D_h = D - d = 25.7\,\mathrm{mm}$ and a dimensionless length $L/D_h = 57.5$. The flow enters the test section through a bellmouth contraction proceeded by an array of fibrous inserts which manage the flow and suppress large-scale motions induced by the incoming liquid. The fluid was an aqueous solution of ammonium thiocyanate (NH_4SCN); its concentration was adjusted carefully so that its refractive index matched precisely that of acrylic material. The fluid viscosity μ and density ρ were measured independently for a range of temperatures that exceeded the experimental range, so that accurate values were used to calculate the Reynolds number for all tests. The fluid was seeded with hollow glass spheres (Sphericel 110P8, Potters Industries Inc., Malvern, Pennsylvania, USA) having a density of $1100\,\mathrm{kg/m^3}$ and a mean diameter of $8\,\mu\mathrm{m}$. The flow rate was measured with calibrated transit-time ultrasonic flow meters (FDT-31 and FDT-32, OMEGA Engineering, Inc., Stamford, Connecticut, USA). The flow meter results were recorded using a multifunction data acquisition system (NI USB-6008, National

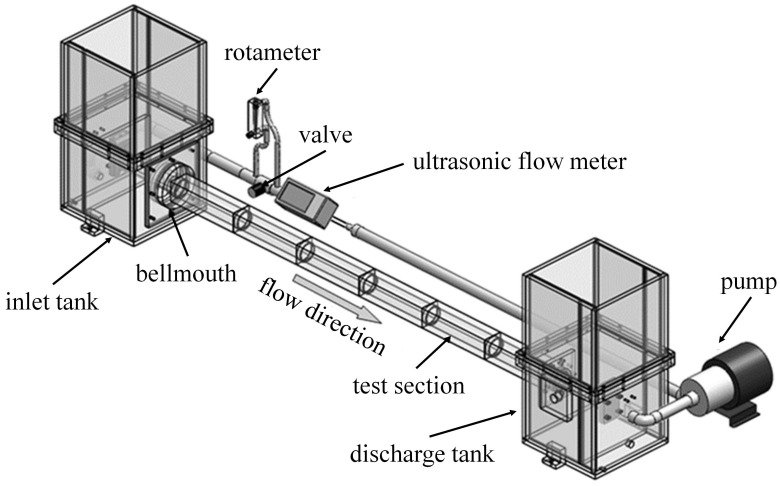

Figure 2: The experimental setup.

Instruments Corp., Austin, Texas, USA). Time-resolved local flow velocity was measured with a two-component laser Doppler velocimeter (LDV) system (Fiber Flow 2D LDA and BSA F50 signal processor, Dantec Dynamics S/A, Skovlunde, Denmark; 55 mm ML f/1.2 lens, Yashica Co. Ltd., Nagano, Japan) having a maximum measurement volume with a length of 0.061 mm and a diameter of 0.014 mm for the streamwise component and a length of 0.058 mm and a diameter of 0.014 mm for the transverse component. The sampling rate, which depended on the local seed concentration and the local flow velocity, had an average value of 215 samples/s. Cross-sectional velocity maps were recorded with a planar particle image velocimeter (PPIV) and a stereoscopic particle image velocimeter (SPIV), at the rates of 7.0 Hz and 3.5 Hz respectively (Cameras: Imager pro X 4M, LaVision Inc., Ypsilanti, Michigan, USA, with 50 mm lenses AF-Nikkor, Nikon Corp. Tokyo, Japan; double pulse Nd:YAG laser, Solo PIV 120XT, New Wave Research, Fremont, California, USA).

Figure 3 shows all relevant coordinates and dimensions as well as the positions of main measurement points on a cross-plane. Position 1 is the centre of the narrow gap, while position 5 is the centre of the wide gap. Flow perpendicular to the $x - y$ plane will be referred to as the axial flow, whereas at positions 1 and 5, flow in the x direction will be called the cross-flow. Table 1 lists the coordinates of cross-sectional measurement positions that have been marked in figure 3. The eccentricity is defined as

$$e = \frac{2\Delta y}{D - d}, \tag{2.1}$$

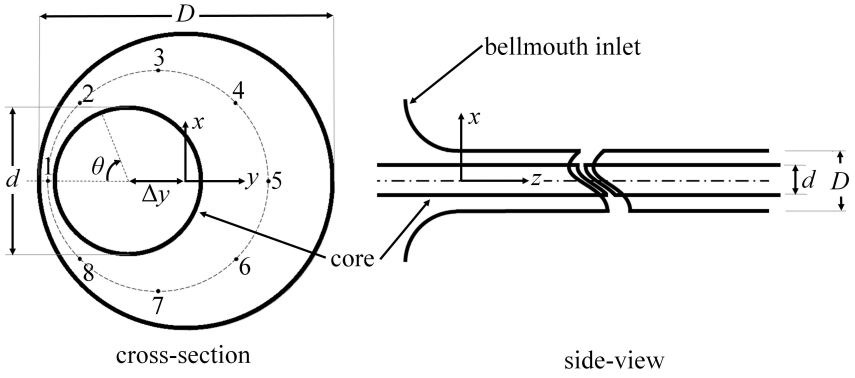

Figure 3: Annular geometry with a definition of coordinates and measurement positions on a cross-plane.

Position	x/D	y/D
1	-0.48	0.00
2	-0.37	0.27
3	-0.10	0.38
4	0.17	0.27
5	0.28	0.00
6	0.17	-0.27
7	-0.10	-0.30
8	-0.37	-0.27

Table 1: Measurement positions on a cross-plane.

where Δy is the distance between the axes of the inner and outer cylinders.

2.2. *Measurement procedures and uncertainties*

The refractive index of the ammonium thiocyanate solution was measured with the use of an optical refractometer with an uncertainty of 0.0001 (model ABBE-3L, Bausch & Lomb, Rochester, New York, USA). The solution concentration was adjusted to match that of acrylic material, cited in the literature as 1.4915. Water was occasionally added to the solution to account for evaporation. It is noted that the solution refractive index varied slightly with the solution temperature (over the fluid temperature range from 302 K to 310 K during the experiments, the refractive index was approximately 1.487 ± 0.001), but it was verified that this variation did not affect the results by a measurable amount. The viscosity and specific gravity of the solution were, respectively, measured using a calibrated falling ball viscometer with repeatability of ±1% (GV-2100, size No.1, Gilmont Instruments Inc., Great Neck, New York, USA) and a calibrated hydrometer with an

uncertainty of 0.005 (model 11522A, Fisher Scientific Ltd. Hampton, New Hampshire, USA). It was found that, at 303 K, $\mu = 1.69 \pm 0.02$ mPa s and $\rho = 1138 \pm 5$ kg/m^3. The flow meter results were compared with the bulk velocity calculated from cross-sectional SPIV measurements and, after temperature corrections were applied to the former, the mean, standard deviation and maximum differences were found to be 0.9%, 1.8% and 3.6%, respectively. The Reynolds number, based on the hydraulic diameter and the bulk flow velocity U_b, was calculated as

$$\mathrm{Re} = \frac{\rho D_h U_b}{\mu} \tag{2.2}$$

The estimated uncertainty in the Reynolds number value was 300 for Re = 7300, which is the nominal value for the results presented in this article. The eccentricity was set by eye under 40X magnification at three positions along the test section length using crossing LDV beams as a reference for the position of the inner core; based on the dimensions of the LDV beams, the magnification and a margin of error, we estimated the uncertainty in Δy to be 0.5 mm. The corresponding uncertainty for an eccentricity of 0.80 was 0.04. Two sets of LDV measurements were collected. For the first set, the LDV measurement volume was fixed at one position and measurements were taken over a relatively long time (approximately 1000 times the period of large-scale fluctuations in the flow); these measurements were used to calculate local statistics, including power spectra. For the second set, the LDV probe was traversed axially with a constant velocity of typically about $0.004U_b$, which was slow enough to permit the calculation of a meaningful average of the local velocity; this was done by segmenting the signal into 25 blocks and calculating the mean velocity of each block; moreover, traversed-probe velocity signals provided a fairly representative indication of the local velocity fluctuation level and waveform shape. Two subsets of traversing LDV measurements were taken in most cases, with the LDV probe facing the test section from two different directions; in one orientation the LDV system measured the z and x velocity components, whereas in the other orientation it measured the z and y velocity components. PPIV measurements were performed using two cameras side by side in order to capture the flow over a longer axial distance than a single camera would permit without sacrificing spatial resolution. The axial length of these dual images was $\Delta z/D_h = 10$. For the SPIV measurements, undistorted recording of the flow in the channel cross-section was achieved by camera viewing through two

precisely machined and polished acrylic prisms, affixed to the sides of the test section; Scheimpflug lens adapters were used to allow the measurement plane to be in focus.

3. Results and discussion

3.1. *Inlet flow conditions*

As mentioned previously, all results presented in this article were taken in an annular channel with a diameter ratio of 0.5, at the same nominal eccentricity of 0.8 and, with some exceptions, at the same nominal Reynolds number of 7300. However, for measurements taken at different times, core position and bulk velocity values were adjusted independently and could not be matched precisely, with their variations specified by the reported uncertainties. In some cases, small differences in eccentricity and Reynolds number are reflected in small differences in local velocity values measured at different times or by different techniques, but this has no effect on the general observations and conclusions. A more significant effect on the development of flow phenomena of interest in this work was introduced by differences in the flow conditions in the inlet tank. Effort was made to create a flow at the inlet of the test section that would be fairly uniform and free of coherent structures and significant turbulence. Towards this objective, the inlet tank was made fairly large by comparison to the test section volume and was equipped with flow management devices as well as a bellmouth entry to the test section. Although this objective was generally met, the apparatus needed frequent cleaning and service, following which it was impossible to reproduce the exact flow management device arrangement and this resulted in somewhat different inlet conditions for different sets of results. A systematic study of the effects of upstream conditions was conducted and its results will be reported in the companion article. For rough purposes, one may characterise each particular arrangement of inlet tank flow management devices as mild, moderate or strong upstream flow management, as manifested by the presence of relatively strong, moderate or weak, respectively, velocity fluctuations just downstream of the test section inlet. As a representative set of "moderate" inlet conditions, LDV measurements of the time-averaged streamwise and transverse velocity components and the corresponding turbulence intensities at a few selected positions (see figure 3 for a definition of these positions) on the cross-plane at $z/D_h = 1.4$ are presented in table 2. The inlet conditions were the same for all results in the present article, except those presented in sections 3.5 and 3.6. In section 3.5, strong flow management was used to allow the flow to develop

Position	U_x/U_b	u'_x/U_b	U_z/U_b	u'_z/U_b
1	0.010	0.008	0.927	0.032
2	-0.069	0.014	1.042	0.025
5	0.014	0.021	1.114	0.023
7	0.026	0.017	1.118	0.035
8	0.058	0.012	1.114	0.040

Table 2: Near-inlet velocity measurements ($z/D_h = 1.4$).

more slowly, so that it would only reach full development near the end of the test section; the inlet conditions for this flow are presented in that same section. In section 3.6, the inlet conditions were intended to be "moderate", but because precise matching of inlet conditions was not possible, local values in this case were slightly different from those in earlier sections, although these differences had at most a minor effect on the flow beyond the development region. Table 2 shows that, near the inlet and away from walls, the streamwise velocity component was nearly uniform (within roughly $\pm 0.12 U_b$) and the transverse velocity component was quite small (within $\pm 0.07 U_b$). Moreover, the standard deviation of the streamwise velocity fluctuations at all inlet measuring positions was less than $0.04 U_b$ and that of the transverse velocity fluctuations was less than half that value. In summary, the inlet flow for the experiments reported in this article may be deemed to be moderately disturbed in its mean and its fluctuations. The level of inlet disturbances is probably comparable to that at the inlet of pipes in common engineering systems and, although not excessive, it is deemed to be sufficient for triggering instability processes to which the flow may be prone and inducing bypass transition in the boundary layers.

3.2. *Mean flow development*

As an overall view of the velocity field development along the annular channel, figure 4 shows traces of the three velocity components U_x, U_y and U_z at five representative positions on a cross plane (figure 3). These traces were obtained with the LDV probe traversed slowly along the test section, first in one orientation to measure U_x and U_z and then in another to measure U_y and U_z. One may get representative local averages from these traces, which have been marked on the plots in figure 4. The evolutions of the mean streamwise velocity component at all five positions have been plotted together in figure 5 for comparative purposes. One may notice that only this component has significant values, whereas the two mean transverse components fluctuate only slightly around zero. These results demonstrate that the flow in the test section can be divided

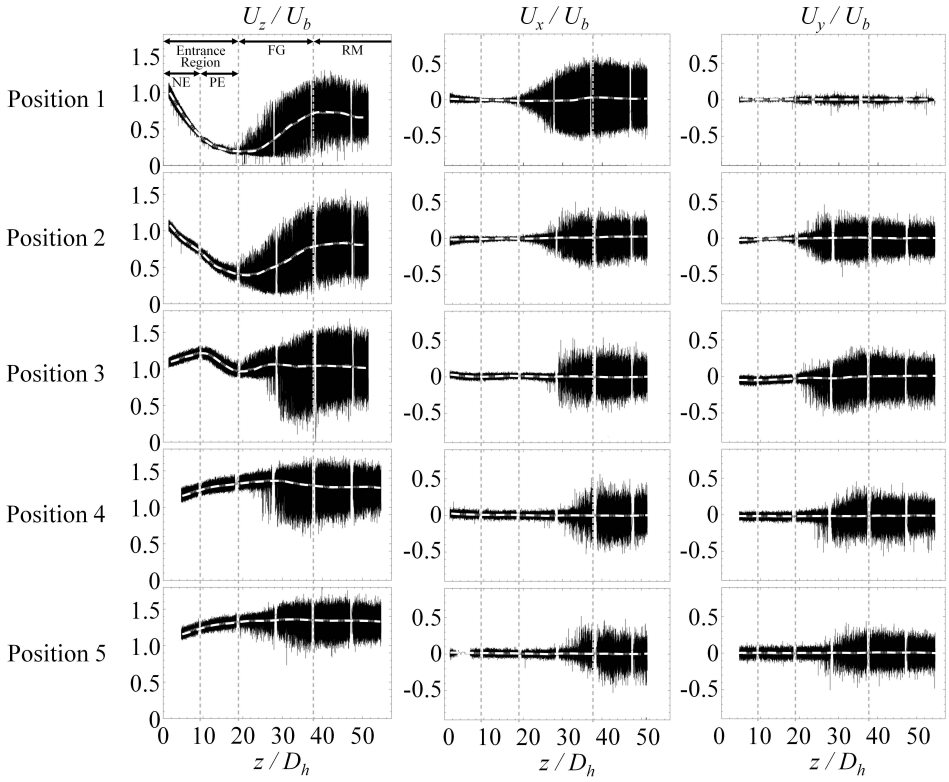

Figure 4: Traces of the fluctuating velocity components, measured by a probe that was traversed slowly along the test section; the gaps in the signals correspond to optically inaccessible regions, where segments of the test section were glued together; white dashed lines indicate local averages; dashed lines parallel to the ordinate axes indicate boundaries between regions with distinct flow features: a) the entrance region, b) the fluctuation-growth (FG) region and c) the rapid-mixing (RM) region; the entrance region is further subdivided into i) the non-periodic-flow entrance (NE) subregion and ii) the periodic-flow entrance (PE) subregion.

into three regions, in each of which the mean streamwise velocity exhibits a distinct trend. Although their presence can be detected at all positions, these trends are more clearly visible at mid-gap (position 1) and so the discussion will first focus at this position. For their convenient reference in the remainder of this article, these three regions have been assigned names, which are indicative of the dominant local physical phenomena. The reader is referred to later sections for a full justification of the chosen names. The three regions are the following ones.

(*a*) *The entrance region* ($0 \leqslant z/D_h \leqslant 18.5$): In the middle of the narrow gap (position 1), U_z decreased monotonically from a value roughly equal to U_b at the inlet to a mini-

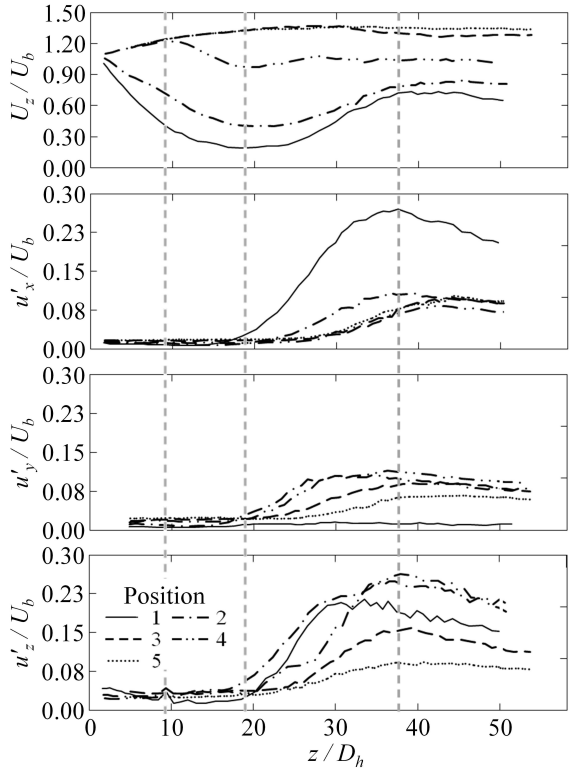

Figure 5: Streamwise variations of the local axial velocity average and the local standard deviations of the three velocity components; dashed lines parallel to the ordinate axes indicate boundaries between regions, as defined in figure 4.

mum of about $0.19U_b$ at $z/D_h = 18.5$. A similar, but less intense, trend was observed at position 2, which was still in a narrow part of the channel and where the mean axial flow reached a minimum of about $0.40U_b$ at $z/D_h = 18.5$. In contrast, at position 3, which was intermediate between the narrow and wide parts of the channel, the mean axial flow was found to initially increase gradually, reaching a maximum value of $1.22U_b$ at $z/D_h = 10$, before decreasing again to a minimum of $0.98U_b$. At positions 4 and 5, which are both in the wide part of the channel, the mean axial velocity increased monotonically in the entrance region to a value of $1.33U_b$ at $z/D_h = 18.5$, which was not, however, a local maximum as the velocity kept increasing slowly in the next region. The previous observations clearly demonstrate that the entrance region is characterized by a redistribution of the flow in the cross-section, such that some fluid moved away from the vicinity of the narrow gap towards the rest of the channel. This is the expected trend, as frictional stresses with the wall would be stronger in the narrow gap than in the open channel.

(*b*) *The fluctuation-growth (FG) region* ($18.5 \leqslant z/D_h \leqslant 37.5$): In this region, the mid-gap velocity, and the one at position 2, increased from their minima to maxima, which were, respectively, $0.73U_b$ and $0.80U_b$. At the three other positions, the velocity variations within this region were fairly small. As far as the mean velocity distribution is concerned, this region is characterized by a tendency towards a partial restoration of the nearly uniform field that existed at the inlet. This restoration is, of course, not complete and reflects the fact that friction is stronger in the narrow gap.

(*c*) *The rapid-mixing (RM) region* ($37.5 \leqslant z/D_h$): The mean velocities at all positions in this region change little, if at all, with streamwise distance. One may observe, however, a slow decrease of the mid-gap velocity.

In summary, observation of the mean velocity variation alone was sufficient for one to identify three distinct regions along the annular channel. This, however, cannot fully describe, neither explain, the profound structural changes that take place as the flow evolves and so additional flow properties need to be examined.

3.3. *Growth of velocity fluctuations*

The envelopes of the velocity traces shown in figure 4 are essentially loci of the extreme values of the corresponding velocity components and so they provide a good measure of the local intensity of velocity fluctuations. The streamwise variations of the standard deviations of the three velocity components are further shown in figure 5. A discussion of the evolutions of the velocity fluctuations in the three regions that were identified previously is as follows.

(*a*) *The entrance region*: In the entrance region, the intensities of all velocity fluctuations remain fairly small (a few percentage points of U_b) and comparable to the corresponding levels at the inlet and the fluctuation intensities in the cores of fully developed turbulent pipe flows. Although the mean velocity is redistributed in this region, this does not entail large velocity fluctuations.

(*b*) *The fluctuation-growth region*: Following the start of this region, the velocity fluctuations at all positions grow explosively and reach maximum amplitudes at about the end of this region. The most drastic growth is demonstrated by the mid-gap (position 1) cross-flow fluctuations u'_x, which increased from about $0.01U_b$ to about $0.27U_b$, with the peak-to peak amplitude reaching about $0.59U_b$. Similarly, the mid-gap axial velocity fluctuations u'_z grew to a value of about $0.20U_b$ within the FG region. Towards the end of this region, the mid-gap axial velocity occasionally exceeded U_b, which corroborates the

fact that high-speed fluid from the open channel occasionally crossed the narrow gap. By exception, the along-gap fluctuation u'_y maintained relatively low values, which is attributed to its obstruction by the two nearby walls (no penetration condition). Similar but less drastic observations can be made for the velocity fluctuations at position 2. At positions 3, 4 and 5, it is also clear that the fluctuations of all velocity components grew drastically within the FG region. Nevertheless, the axial fluctuation patterns at these positions are noticeably different from those at position 1. As the envelopes of the velocity traces in figure 4 illustrate, the maximum and minimum velocities at position 1 were essentially at equal distances from the corresponding means, whereas at positions 3, 4 and 5 the velocity waveforms were strongly skewed, indicating that slow fluid occurrences were less frequent but more intense than fast fluid occurrences. The presence of fluid with velocity lower than $0.2U_b$ at position 3, where the average velocity is not very different from U_b, shows the occasional deep penetration of mid-gap fluid into the open channel.

(*c*) *The rapid-mixing region*: The rapid growth of velocity fluctuations that was observed in the FG region did not extend to the RM region. On the contrary, in the RM region all fluctuations diminished downstream, albeit at relatively slow rates. This trend continued to the last measuring station, where the rates of fluctuation decrease appeared to tend towards asymptotes. Although our test section was not sufficiently long for a definitive proof, the observed trends support the conjecture that both the mean velocity and the velocity fluctuations would eventually reach fully developed states, in which their statistical properties would be independent of streamwise location.

3.4. *Onset and growth of quasi-periodic motions*

In this section, we will examine the presence of regularly recurring patterns in the velocity field, which are indicative of quasi-periodic motions. As mentioned previously, the phenomena of interest manifest themselves most clearly at mid-gap and so we will first focus at this position. Figure 6 shows representative time histories of the cross-flow and axial velocity components at mid-gap (position 1) at five downstream locations. These measurements were obtained with the LDV probe fixed at the corresponding location. Let us first examine the cross-flow time histories, shown on the left column of this figure. Close to the inlet (z/D_h = 1.4), the velocity signal appears to be random, as it corresponds to turbulence from the inlet tank entering the annular channel. At z/D_h = 14.4, however, the signal looks roughly sinusoidal, although some random fluctuations also seem to ride on the quasi-periodic mode. The latter location is well within the entrance region and is not

marked by any distinct change in either the mean velocity, which continues to decrease downstream, or the standard deviation of the velocity fluctuations, which continues to be relatively small. Nevertheless, this signal is unmistakeable evidence for the onset of periodicity somewhere in the entrance region. The time history at $z/D_h = 14.4$ exhibits familiar patterns of other types of flows in early stages of instability, when a mode at a preferred frequency (or wavelength) is excited and sustained, whereas perturbations at other frequencies die out. The periodic appearance of the cross-flow is maintained in both the FG and RM regions, as illustrated by the time histories at $z/D_h = 24.2$, 31.9 and 51.5. Even though the period of the dominant oscillations does not seem to change much downstream, their amplitudes are much higher in the FG and RM regions than in the entrance region. Small-scale turbulence is also seen superimposed on the quasi-periodic velocity fluctuations, but is not strong enough to obscure them or change their character. Another important observation is that all quasi-periodic signals have occasional phase shifts, marking the partial missing of some cycles. The time histories of the axial velocity components, shown on the right column of figure 6, are qualitatively similar with the corresponding cross-flow time histories, although the former are not as regular as the latter. More importantly, the axial velocity fluctuates at twice the frequency of the cross-flow, which is consistent with the vortex street model presented in figure 1.

Additional evidence for the presence of periodic motions is provided by representative spectra of the cross-flow at mid gap, shown in figure 7. Whereas the spectrum at $z/D_h = 1.4$ has no discernible peak, the spectra at the four other locations have very prominent peaks, all at approximately the same frequency. The spectrum of the axial velocity at $z/D_h = 51.5$, also plotted in the same figure, does not have as strong peaks as that of the cross-flow. Nevertheless, it has an identifiable peak at approximately the same frequency as the cross-flow peak and a more prominent peak at twice that frequency. Similar observations in the centres of narrow gaps have been made by previous investigators (*e.g.*, Wu & Trupp 1993; Meyer & Rehme 1994), whereas in some cases no axial velocity peak was discernible. Even though periodicity is evident in the time histories of both the cross- and axial flow components (see figure 6), axial flow has stronger fluctuations at other frequencies, which may obscure or obliterate its main peak.

The frequency of flow oscillations may be presented in dimensionless form as the Strouhal number, defined as

$$\mathrm{St} = \frac{fd}{U_b}. \tag{3.1}$$

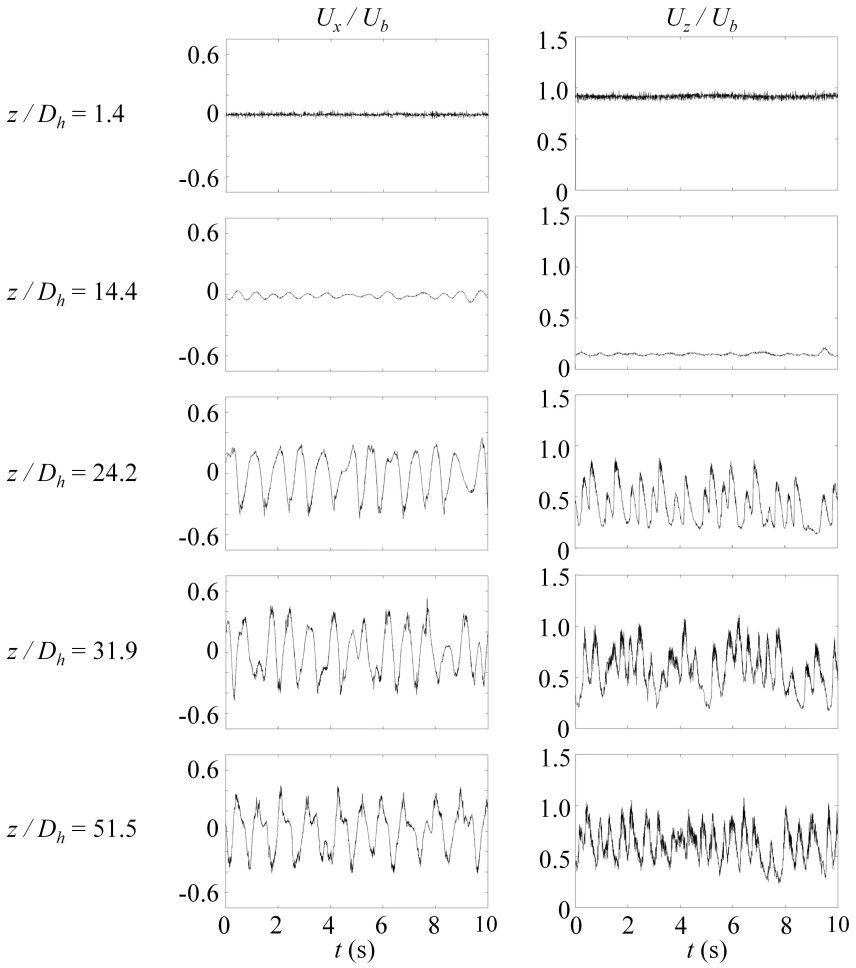

Figure 6: Time history segments of the cross-flow and axial velocity components at mid-gap (position 1) at five downstream locations.

Figure 8 shows the streamwise variation of the Strouhal number of cross-flows at mid-gap. It was observed that a distinct peak in the spectra only appeared for $z/D_h \geqslant 9.0$. Based on this observation, one may subdivide the entrance region into two subregions: i) *the non-periodic-flow (NE) entrance subregion*, extending in the range $0 \leqslant z/D_h \leqslant 9.0$), and ii) *the periodic-flow (PE) entrance subregion*, in the range $9.0 \leqslant z/D_h \leqslant 18.5$). The boundary between these subregions has been marked in figure 4; it may be confirmed that the onset of periodic motions has no visible effect on the development of the velocity field in the entire entrance region. The Strouhal number at mid-gap appears to increase slightly within the FG region (roughly from 0.08 to 0.09) and then to decrease slightly

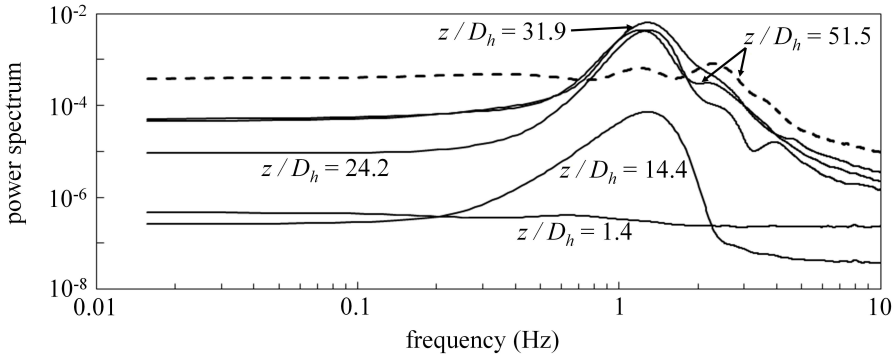

Figure 7: Power spectra of mid-gap cross-flows at five different downstream positions (solid lines) and power spectrum of axial velocity (dashed line) at $z/D_h = 51.5$; the scale of the ordinate axis is arbitrary.

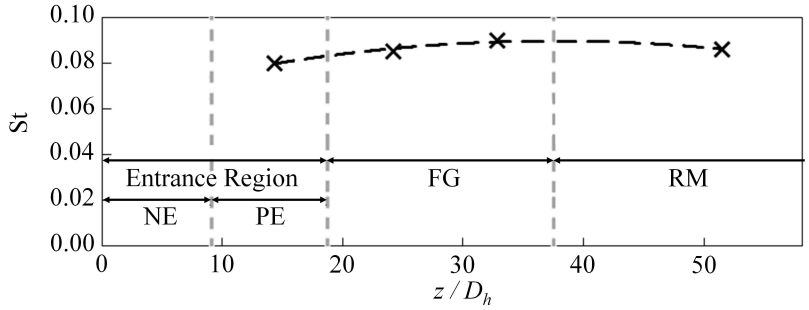

Figure 8: Streamwise variation of the Strouhal number of mid-gap cross-flow velocity fluctuations.

again in the RM region. It is noted that the frequency of spatially extending flow patterns, measured by a probe fixed at some location, is proportional to the local convection speed of these patterns and so a small change in frequency may be also attributed to a small change in convection speed due to flow redistribution over the cross-section. Moreover, as mentioned in the introduction, flow development is sensitive to inlet conditions, especially at Reynolds numbers below 10,000. The effects of inlet conditions will be discussed in detail in Part 2, which will present comparative analyses of measurements obtained for ranges of dynamic and geometric conditions and with data from the literature.

So far, the occurrence of quasi-periodic velocity fluctuations was established for the narrow gap region. It would be of further interest to examine how far into the open channel such periodicity can be detected. Figure 9 shows representative time histories of all three velocity components at five positions on the cross-plane in the RM region

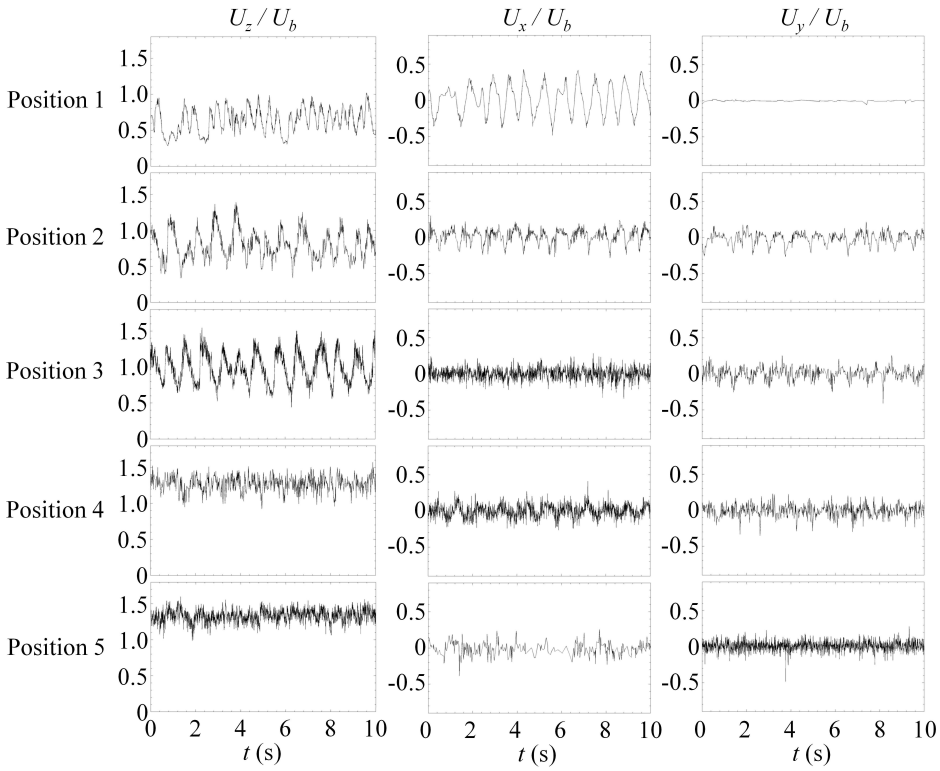

Figure 9: Representative segments of the time histories of the three velocity components at five positions near the end of the test section (z/D_h = 51.5).

(z/D_h = 51.5). Without getting into particulars for each time history, it is evident that some periodicity can be discerned by naked eye at all positions, even though in some cases it is less apparent than in others. This figure supports the conclusion that quasi-periodic motions extend in the entire cross-section of the annular channel. The reasons for the differences in the appearances of the time histories of the three components at different positions will become evident following the presentation of a physical model in the following sections.

3.5. *The mixing layers*

To determine the flow distribution on cross-planes along the test section, instantaneous maps of the three velocity components on the entire cross-plane were recorded using SPIV. A sufficient number of such maps were averaged to give the corresponding time average maps. Figure 10 shows both time-averaged axial velocity contours and two representative sets of instantaneous contours at four downstream locations representing the

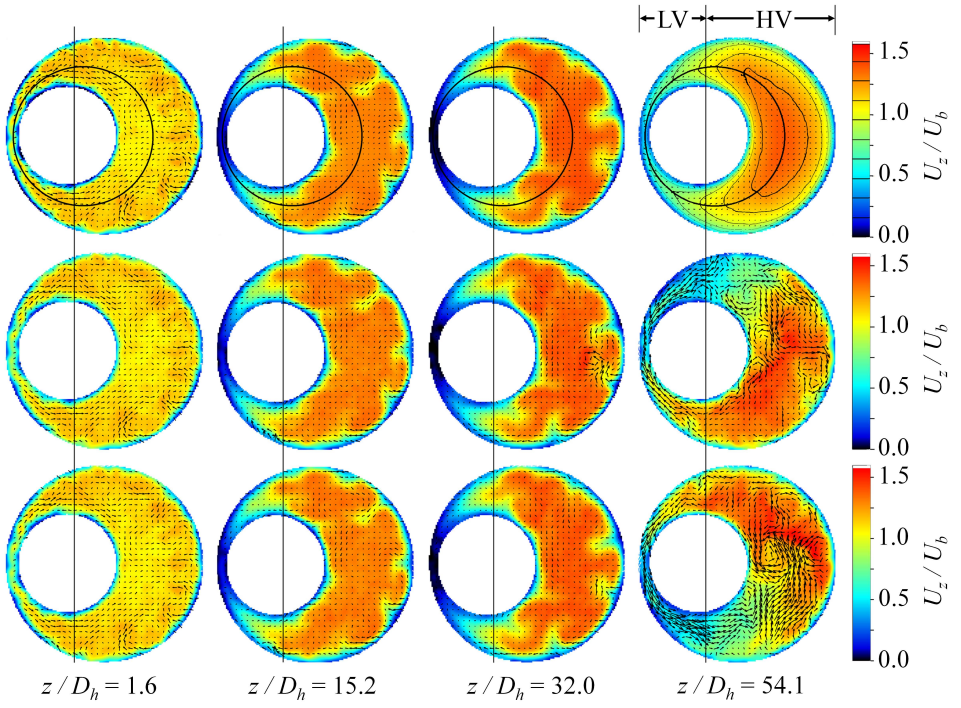

Figure 10: Axial velocity contours and the corresponding transverse velocity vector maps on three cross-planes; images in the three columns are, from left to right, in the NE subregion, the PE subregion and the RM region; the top row shows time averages, whereas the middle and bottom rows show two sets of instantaneous results; the intermediate circles on the top row indicate the locus of local velocity maxima in the space between the two surfaces of the annulus at $z/D_h = 54.1$; vertical lines connect approximately the two inflection points of the azimuthal profile of the local velocity maxima at $z/D_h = 54.1$ (figure 11).

three distinct regions and two subregions of flow development. The instances shown in figure 10 are not consecutive in the video sequence, nor separated by a specified time interval, because our SPIV system was not time resolving. Instead, they are representative of the diversity of appearances of velocity maps at a given location. Moreover, as we have stated elsewhere, the SPIV experiments were conducted under upstream conditions that were slightly different from those corresponding to LDV results and so the streamwise developments of flows may vary somewhat among the different sets of results.

(*a*) *The entrance region. i) The NE subregion*: In a cross-section near the inlet ($z/D_h = 1.6$) and within the NE subregion where no cross-flow periodicity was detected, the local velocity variations both in space and in time were relatively small (up to ±20%) and the instantaneous velocity maps did not differ significantly from each other or the time-

average map. Because the flow at the inlet is sensitive to upstream conditions, we will refrain from attaching particular significance to the various weak vortices and other patterns that one may identify by close observation of the maps. A clear pattern that is visible on the superimposed vector maps of the transverse velocity is that fluid from the narrow gap region, where viscous stresses are relatively high, is directed towards the open channel; these transverse velocities were of the order of 1% near the inlet and diminished progressively downstream. Moreover, fluid from near the walls in the open channel is seen to shift towards the core; this does not occur in a spatially uniform fashion, but in the form of stripes of low velocity fluid separating spots with higher velocity; these azimuthally distributed patterns appear to be similar to those forming in the entrance regions of turbulent pipe flows at moderate Reynolds numbers. *i) The PE subregion*: Further into the entrance region (z/D_h = 15.2), where cross-flow periodicity was detectable but very weak, the instantaneous and time-average velocity maps still looked very much alike, but the local velocity in the open part of the channel was significantly larger than that in the narrow gap region. In the open channel, the azimuthally distributed low and high velocity patterns of near-wall fluid became much more distinct and fewer in number than closer to the inlet, but remained stable and did not change position in time. Whatever quasi-periodic velocity fluctuations were present in this region were not discernible on the cross-sectional velocity maps.

(*b*) *The fluctuation-growth region*: In this region, fluid continued to be diverted from the narrow gap to the open channel; however, the volume of fluid in the gap was small and the resolution of velocity maps was not sufficient to show clearly such motion. Deeply into this region (z/D_h = 15.2) , cross-flow oscillations in the gap became very strong, but once more such oscillations were only slightly perceptible in instantaneous velocity maps, which differed little from the average ones. So, one may conjecture that the growing cross-flow fluctuations in the gap set the rest of the fluid in weak, nearly rigid-body-type oscillations, but without effecting much mixing.

(*c*) *The rapid-mixing region*: Near the end of the test section (z/D_h = 54.1), the cross-planar velocity maps were dramatically different from those at upstream locations. The two instantaneous maps were very different from each other and the velocity contours were strongly asymmetric. A large pocket of high velocity fluid was present in each instantaneous map, but its position shifted across the open channel from one flank to the other. A large pocket of low velocity fluid also appeared next to the high-speed pocket

and shifted widely across the gap. In sharp contrast, the time averaged velocity contours were essentially symmetric and quite smooth. The maximum average velocity in the entire channel was $1.40U_b$ and occurred near the middle of the wide gap and the local average velocity decreased monotonically from this position towards the narrow gap in either direction; in the middle of the narrow gap, the time average velocity was $0.63U_b$. The near-wall low- and high-velocity patterns remained visible in the instantaneous maps, shifting back and fourth sideways with the rest of the fluid, but disappeared altogether in the average map. In general, the instantaneous contours were much more distorted than those upstream and bore evidence of small-scale turbulence and intense mixing. In order to define radial-like profiles of the velocity in this annular geometry, we introduced the bipolar coordinate system (El-Saden 1961; Snyder & Goldstein 1965) (η, ξ), in which curves of constant η are non-intersecting circles of different radii bounded by the inner and outer surfaces of the annular channel, and curves of constant ξ are non-concentric circles which are orthogonal to the constant-η circles. Then we traced time averaged axial velocity profiles along the curves of constant ξ for $0 \leqslant \xi \leqslant 2\pi$ and identified the maximum velocity along each curve. The locus of the locations of these local maxima $z/D_h = 54.1$ coincided approximately with the perimeter of a circle with a diameter $0.70D$ and centred along the plane of symmetry at $\Delta y = 0.13D$. For comparisons, the same circle has been drawn on the time average velocity maps at the three upstream locations (figure 10). Next, the azimuthal variations of the axial velocity around the previously defined circles were plotted in figure 11. In all cases, these profiles were roughly wake-like, if one considers the mid-gap as the centre, with a mixing layer forming on either side. Consequently, each profile had a pair of symmetrically located inflection points, whose azimuthal position, however, depended on downstream location. At $z/D_h = 54.1$, these inflection points occurred at $\theta = \pm 100^\circ$. For comparison, we have also computed the locus of the local velocity maxima of the exact solution for fully developed laminar flow in the present annular channel (Snyder & Goldstein 1965; Piot & Tavoularis 2011) and found that the inflection points occurred at $\theta = \pm 82^\circ$, namely closer to the narrow gap than the present results. A plane that is parallel to channel axis and contains the two inflection points separates the channel into two zones: a low velocity (LV) zone, around the narrow gap, and a high velocity (HV) zone, encompassing the open channel. This allows us to define twin mixing layers between these two zones and explore a possible analogy between conventional mixing layers and the present annular flow. These zones have been identified

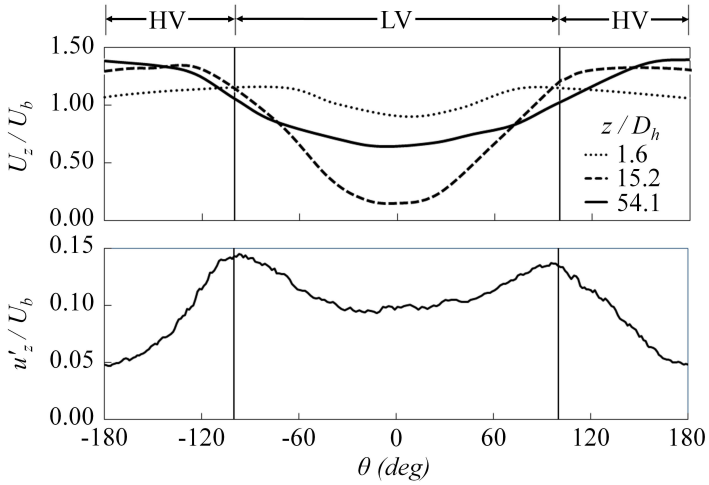

Figure 11: Azimuthal variations of the time average axial velocity along the locus of the local velocity maxima at three downstream locations (top) and the standard deviation of the axial velocity at z/D_h = 54.1 along the same locus (bottom).

in figures 10 and 11. In plane turbulent mixing layers, the inflection point coincides with the peak velocity fluctuations, as it is the location of maximum turbulent production. This is also the case in the RM region of the annular channel, as shown in figures 11-bottom and 12-left. Moreover, figure 12-right demonstrates that, in the proximity of the inflection points, not only the velocity fluctuations are at their strongest, but also the periodicity is strongest; this figure shows contours of local power spectral density at the peak frequency and it is noted that similar contours at slightly lower or higher frequencies had much lower values, to the degree that they were indistinguishable from the background level. This is an important observation, because it demonstrates that, at least in the RM region, periodic motions that were first detected in the narrow gap extended far into the open channel and that they peaked in magnitude at two intermediate azimuthal positions.

3.6. *The vortex street*

Figure 13 (top) shows representative velocity maps at five sections of the channel in a vertical plane passing through the centre of the narrow gap; the images of the five sections presented were recorded separately but under the same flow conditions, and were matched in phase and collated such that the flow appeared to be continuous along the channel. Below the velocity maps is a plot of the streamlines of velocity in a frame convected axially by the average axial flow velocity in the final frame, which was approximately

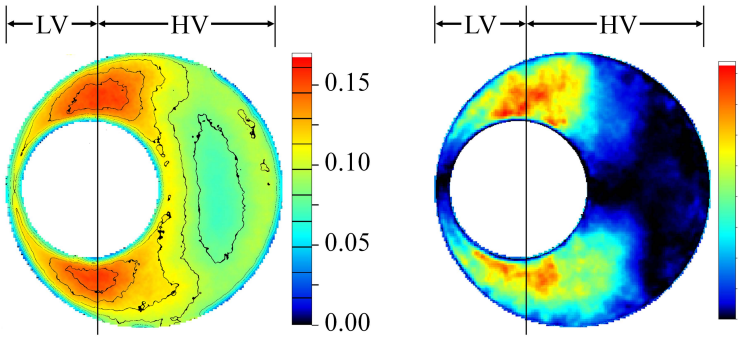

Figure 12: Contours of the standard deviation of the axial velocity fluctuations u'_z/U_b (left) and the power spectral density of the axial velocity at the peak frequency (right; arbitrary scale); $z/D_h = 54.1$.

$0.65U_b$. A street of staggered, counter-rotating vortices, compatible in general terms with the model shown in figure 1, can be identified. The centres of these vortices were outside the measurement plane, even in the early stages of their formation. This demonstrates that these vortices are not generated in the narrow gap and move outwards as they grow, but rather in the mixing layer from which they extend to the gap region as they evolve downstream. From figure 13, one may estimate the vortex street wavelength, namely the distance between consecutive vortex pairs, as roughly $\lambda \approx 7D_h$, which also corresponds to $\lambda \approx 7d$ in the present case; it is noted that in past literature λ has usually been normalized by the rod diameter d. It should also be noted that the Reynolds number for these measurements was slightly higher than that for results presented in earlier sections and the upstream flow was more heavily managed to further reduce upstream disturbances; although such differences do not change our main observations, they are responsible for some small quantitative variations that one may notice by comparing different figures. For a more quantitative estimate of the vortex street wavelength in the rapid-mixing region, we took measurements of the streamwise spatial autocorrelation coefficient of the axial and cross-flow velocities by ensemble averaging of SPIV images (figure 14-left). Both correlations show clear spatial periodicity, with the wavelength of the axial fluctuations being roughly half that of the cross-flow fluctuations. An average vortex street wavelength $\lambda \approx 7.5d$ is compatible with these correlations. The periods of the cross-flow and axial velocity fluctuations were estimated from the corresponding temporal autocorrelation functions at mid-gap and at approximately the same downstream position (figure 14-right). Once more, both types of fluctuations were found to have a strongly periodic

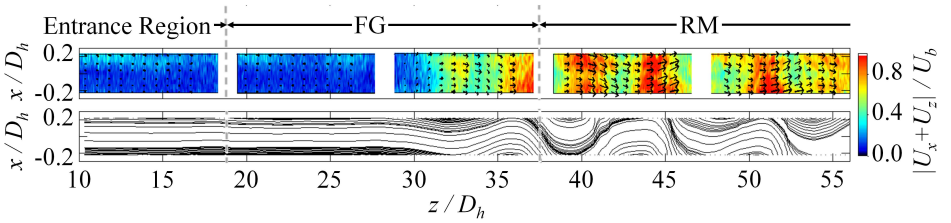

Figure 13: Velocity vector maps in an axial plane passing through the narrow gap centre (top); streamline projections in a the same plane, viewed in a frame convected by $0.65U_b$ (bottom); Re ≈ 7800.

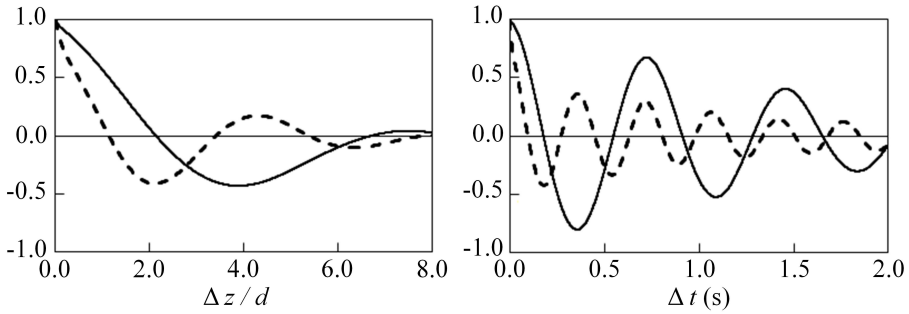

Figure 14: Spatial (left) and temporal (right) autocorrelation coefficients of the cross-flow velocity (solid lines) and the axial velocity (dashed lines) at mid-gap and near the end of the test section; Re ≈ 7800.

character; the period of cross-flow fluctuations, deemed to be equal to the period T of the vortex street, was essentially twice that of the axial velocity fluctuations. These results can be used to estimate the convection speed of the vortex street as $U_c = \lambda/T \approx 0.65U_b$. This value is consistent with the convection speed used to obtain the streamlines in figure 13 (bottom).

Flow visualization using a high speed camera pointed parallel to the plane passing through positions 2 and 4 in figure 3 is displayed beside PIV results on the same plane but taken at a later time (figure 15). The narrow gap is toward the bottoms of each of the four sections of the figure and the wide gap is toward the tops. In the flow visualization one can see roll-ups that are transported downstream; the roll-up direction is consistent with a mixing layer having a lower velocity at the bottom. A high degree of complexity is evident in the flow; in addition to the main vortex, multiple smaller vortices can be seen at the upper boundary of the main vortex; immediately proceeding the main vortex the flow appears quite uniform. Following the vortex, however, the flow appears much more turbulent. Observing the flow in slow motion using a high speed camera showed that the

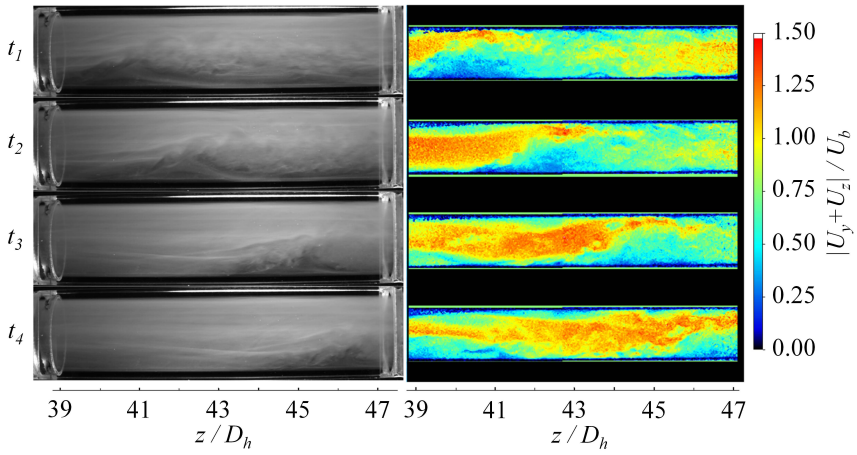

Figure 15: Flow visualization (left) and PIV (right) results showing the plane crossing positions 2 and 4 in figure 1.

boundary between the low and high speed fluid oscillates between the narrow and wide gap; at some point, as this boundary moves more toward the wide gap, a series of small vortices suddenly appear and grow; these small vortices however are rapidly absorbed by a larger vortex which appears almost independently of them and quickly dominates the region. To provide a clear view of the various flow patterns that were observed during flow development along the channel, "Movie 1" has been included as supplementary material.

4. Summary and concluding remarks

In this work, we investigated isothermal flow development and structure in a strongly eccentric annular channel, considered to be representative of complex channels having narrower regions that are adjacent to wider ones. This flow was shown to be very complicated, with dominant features that are absent from flows in channels with relatively simple cross sections, such as pipes and rectangular or concentric annular channels. Although it is recognized that flow development in an eccentric channel depends on inner-to-outer diameter ratio, eccentricity, Reynolds number and inlet conditions, the present article examines in depth a single case that exhibits all phenomena of interest, delegating discussion of various effects to a second article.

Based on observations of the streamwise evolution of the mean velocity components at various azimuthal positions, we have identified three distinct flow development regions: the entrance region, the fluctuation-growth region, and the rapid-mixing region. In the

entrance region, fluid was diverted from the narrow gap vicinity towards the open channel and velocity fluctuations were relatively small. Closer observation of velocity fluctuations in the entrance region led us to subdivide it to an initial subregion, in which there was no evidence of any periodic motions, and a following subregion, in which periodicity was detectable in the velocity field. The axial velocity at mid-gap reached a minimum at the end of the entrance region, but increased again to a higher level in the fluctuation-growth region. The most prominent feature of flow in the latter region was a rapid growth of the quasi-periodic velocity fluctuations, which reached amplitudes that were a significant fraction of the bulk velocity. In the rapid-mixing region, the local time-averaged velocity and the amplitude of the velocity fluctuations changed by relatively small amounts, but the flow structure underwent a drastic change: a vortex street, consisting of pairs of counter-rotating vortices on either side of the gap, was formed and fluid mixing became very thorough in the entire channel. The generation of this "gap vortex street" was attributed to the instability of the two mixing layers that formed between slower fluid in the gap and faster fluid elsewhere.

Having identified all these interesting phenomena in a particular eccentric channel, we turn to reflecting on the roles the presence and relative width of a narrow gap play in this process. The observed flow instability was of the Kelvin-Helmholtz type and associated with the inflectional mixing layer profile. The narrow gap is necessary to generate the mixing layers in the first place. Moreover, it permits communication in the pressure fields of the two mixing layers, in a manner analogous to the boundary layer communication on the two sides of a cylinder in cross-flow, which leads to the generation of the von Kármán vortex street. These two effects of the gap need to be considered separately. The instability and the vortex formation in each mixing layer of the eccentric channel can be present in isolation from the other mixing layer. The strong coupling of the vortices on the two sides of the inner cylinder, however, is most likely activated by communication across the gap.

The present work has profited from experience accumulated on similar topics by several authors for many years. However, this is the first study to synthesize the analysis of several types of strategically planned measurements and to reconstruct the sequence of events which lead to the formation of a gap vortex street with its important consequences on flow mixing in complex channels. It has also elucidated the underlying reasons that drive gap instability and gap vortex street formation.

Financial support by the Natural Sciences and Engineering Research Council of Canada and Atomic Energy of Canada Limited are gratefully acknowledged.

REFERENCES

Baratto, F., Bailey, S. C. & Tavoularis, S. 2006 Measurments of frequencies amd spatial correlations of coherent structures in rod bundle flows. *Nucl. Eng. Des.* **236**, 1830–1837.

El-Saden, M. R. 1961 Heat conduction in an eccentrically hollow, infinitely long cylinder with internal heat generation. *J. Heat Transfer* **83** (4), 510–512.

Gosset, A. & Tavoularis, S. 2006 Laminar flow instability in a rectangular channel with a cylindrical core. *Phys. Fluids* **18**, 044108.

Guellouz, M. S. & Tavoularis, S. 2000a The structure of turbulent flow in a rectangular channel containing a cylindrical rod - part 1: Reynolds-averaged measurements. *Exp. Therm. Fluid Sci.* **23**, 59–73.

Guellouz, M. S. & Tavoularis, S. 2000b The structure of turbulent flow in a rectangular channel containing a cylindrical rod - part 2: Phase-averaged measurements. *Exp. Therm. Fluid Sci.* **23**, 75–91.

Hooper, J. D. & Rehme, K. 1984 Large-scale structural effects in developed turbulent flow through closely spaced rod array. *J.Fluid Mech.* **145**, 305–337.

Kacker, S. C. 1973 Some aspects of fully developed turbulent flow in non-circular ducts. *J. Fluid Mech.* **57** (3), 583–602.

Krauss, T. & Meyer, L. 1996 Characteristics of turbulent velocity and temperature in a wall channel of a heated rod bundle. *Exp. Therm. Fluid Sci.* **12**, 7586.

Krauss, T. & Meyer, L. 1998 Experimental investigation of turbulent transport of momentum and energy in a heated rod bundle. *Nucl. Eng. Des.* **180**, 185206.

Lexmond, A. S., Mudde, R. F. & van der Hagen, T. H. J. J. 2005 Visualisation of the vortex street and characterisation of the cross flow in the gap between two sub-channels. In *NURETH-11*. Avigon, France.

Mahmood, A., Rohde, M., van der Hagenand, T. H. J. J. & Mudde, R. F. 2009 Contribution of large-scale coherent structures towards the cross flow in two interconnected channels. In *NURETH-13*. Kanazawa, Japan.

Merzari, E., Wang, S., Ninokata, H. & Theofilis, V. 2008 Biglobal linear stability analysis for the flow in eccentric annular channels and a related geometry. *Phys. Fluids* **20**, 114104.

Meyer, L. 2010 From discovery to recognition of periodic large scale vortices in rod bundles as source of natural mixing between subchannels - a review. *Nucl. Eng. Des.* **240**, 1575–1588.

Meyer, L. & Rehme, K. 1994 Large scale turbulence phenomena in compound rectangular channels. *Exp. Therm. Fluid Sci.* **8**, 286–304.

Möller, S. V. 1991 On phenomena of turbulent flow through rod bundles. *Exp. Therm. Fluid Sci.* **4**, 25–35.

Mott, J. E. & Joseph, D. D. 1968 Stability of parallel flow between concentric cylinders. *Phys. Fluids* **11**, 2065–2073.

Nikitin, N., Wang, H. & Chernyshenko, S. 2009 Turbulent flow and heat transfer in eccentric annulus. *J. Fluid Mech.* **638**, 95–116.

Nouri, J. M., Umur, H. & Whitelaw, J. H. 1993 Flow of newtonian and non-newtonian fluids in concentric and eccentric annuli. *J. Fluid Mech.* **253**, 617–641.

Piot, E. & Tavoularis, S. 2011 Gap instability in laminar flows in eccentric annular channels. *Nucl. Eng. Des.* **241** (11), 4615–4620.

Rehme, K. 1992 The structure of turbulence in rod bundles and the implications on natural mixing between the subchannels. *Int. J. Heat Mass Tran.* **35** (2), 567581.

Rowe, D. S., Johnson, B. M. & Knudsen, J. G. 1974 Implications concerning rod bundle crossflow mixing based on measurment of turbulent flow sturcture. *Int. J. Heat Mass Tran.* **17**, 407–419.

Silin, N., Masson, V. & Rauschert, A. 2008 Large-scale pulsation detection by means of temperature measurments. *J. Heat Transfer* **130** (11), 111602.

Snyder, W. T. & Goldstein, G. T. 1965 An analysis of fully developed laminar flow in an eccentric annulus. *AIChE J.* **11** (3), 462–467.

Tavoularis, S. 2011 Rod bundle vortex networks, gap vortex streets, and gap instability: a nomenclature and some comments on available methodologies. *Nucl. Eng. Des.* **241** (11), 4612–4614.

Wu, X. & Trupp, A. C. 1993 Experimental study on the unusual turbulence intensity distribution in rod-to-wall gap regions. *Exp. Therm. Fluid Sci.* **6**, 360–370.

5.2 Effects of inlet conditions, d/D, e and Re

The manuscript that follows, entitled "Experimental investigation of flow development and gap vortex street in an eccentric annular channel. Part 2. Effects of inlet conditions, diameter ratio, eccentricity and Reynolds number" is in preparation for submission to the Journal of Fluid Mechanics.

In preparation for submission to J. Fluid Mech. 1

Experimental investigation of flow development and gap vortex street in an eccentric annular channel. Part 2. Effects of inlet conditions, diameter ratio, eccentricity and Reynolds number.

George H. Choueiri[1] **and Stavros Tavoularis**[1]†

[1]Department of Mechanical Engineering, University of Ottawa, Ottawa, ON K1N 6N5, Canada

(Received ?; revised ?; accepted ?. - To be entered by editorial office)

The development and structure of flows in eccentric annular channels and their dependence on inlet conditions, inner-to-outer diameter ratio d/D, eccentricity e and Reynolds number Re were studied experimentally, with focus on the phenomena of gap instability and the resulting vortex street. Experimental conditions covered a Reynolds number range between 0 and 19000, an eccentricity range between 0 to 0.9 and inner-to-outer diameter ratios equal to 0.25, 0.50 and 0.75. Much of the discussion was based on measurements in the middle of the narrow annular gap, where the phenomena of interest could be observed most vividly. In the range Re < 7000, the Strouhal number, the normalized mid-gap axial flow velocity and the normalized axial and cross-flow fluctuations at mid-gap were found to increase with increasing Re and to depend strongly on inlet conditions. At higher Reynolds numbers, however, these parameters reached asymptotic values that were less sensitive to inlet conditions. We constructed a map for the various stages of periodic motions *vs.* eccentricity and Reynolds number and found that for $e < 0.5$ or Re < 1100 the flow was unconditionally stable, as far as gap instability is concerned. For $e \leqslant 0.5$, transition to turbulence occurred at Re ≈ 6000, whereas, for $0.6 \leqslant e \leqslant 0.9$, the critical Reynolds number for the formation of periodic motions was found to increase with eccentricity from 1100 for $e = 0.6$ to 3800 for $e = 0.9$. The use of a Strouhal number, based on empirical mixing layer scales, permitted a universal description of gap vortex street periodicity in eccentric annular channels.

Key words: annular flow, eccentricity, inlet conditions, diameter ratio, Reynolds number, gap instability, gap vortex street

† Email address for correspondence: stavros.tavoularis@uottawa.ca

1. Introduction

The present article is an extension of the one by Choueiri & Tavoularis (submitted, 2013), which will be hereafter referred to as Part 1, and which contains additional details about the motivation and objectives of this work. For the present purposes, flows in eccentric annular channels are investigated as paradigms of flows in compound channels containing relatively open subchannels, inter-connected through narrow gaps; compound channels include nuclear reactor rod-bundles, double-pipe heat exchangers, inundated rivers, catheterized arteries and other technological and natural systems. Under certain conditions, flows in such channels are prone to a particular type of instability, recently termed "gap instability" (Tavoularis 2011), which may lead to the formation of gap vortex streets, each consisting of pairs of staggered vortices of alternating direction forming on either side of the narrow gap, in a manner that is analogous in some ways to the von Kármán vortex street. These vortices induce strong cross-gap flow pulsations, which greatly enhance inter-subchannel mixing and cross-gap momentum, mass and heat transfer.

In Part 1, we documented in detail the gap instability and vortex generation and evolution mechanisms for a representative annular geometry and for one set of conditions. In particular, we examined flow in an annular channel with a diameter ratio of 0.50 and an eccentricity of 0.8 at a Reynolds number of 7300. While discussing these results, we elucidated the essential physical phenomena of interest, but we also acknowledged that the flow patterns in complex channels would depend on the geometry, inlet conditions and Reynolds number. The experimental determination of these effects is the objective of the work presented in this Part 2.

As far as fully developed flow in annular channels is concerned, geometry is defined by two parameters, the diameter ratio d/D and the eccentricity e. In rod bundles, important geometrical parameters are the shape of the rod array, the rod pitch-to-diameter ratio p/d and the wall pitch-to-diameter ratio w/d, where w is the sum of the rod diameter and the gap between the rod and an adjacent duct wall. Gap vortices in rod bundles are known to appear and form a network (Tavoularis 2011), but only for relatively small p/d, typically $p/d < 1.2$ (Meyer 2010), whereas whenever p/d was sufficiently large, the effects of such vortices were not measurable (Rowe *et al.* 1974; Hooper & Rehme 1984; Guellouz &

Tavoularis 2000a,b). It is also well known that inter-subchannel mixing and heat transfer become stronger as p/d decreases within a certain range but are weakened again when the gap size is reduced below a very small threshold (Hooper 1983, 1984; Hooper & Wood 1984; Rehme 1987, 1989; Baratto *et al.* 2006; Chang & Tavoularis 2008). The frequency of cross-gap flow pulsations has also been correlated to the gap size and p/d (Tapucu & Merilo 1977; Möller 1991; Guellouz & Tavoularis 2000b).

For a given compound channel geometry, the Reynolds number is expected to play an important role, as it affects all processes that are at work simultaneously, namely flow development starting from the channel inlet, flow instability, transition to turbulence, mixing and vortex interactions. A second factor, whose effect is intimately coupled with the Reynolds number effect, is the level and type of disturbances to the flow as it enters the channel as well as while it flows in it. By analogy to the much simpler flows in circular pipes, one would anticipate that, at least within a certain distance from the inlet and within a certain range of Reynolds numbers, flow patterns in complex channels would be largely determined by inlet conditions and Reynolds number effects. At the same time, one may also apply insight gained for pipe flows to speculate that, far from the inlet and for sufficiently large Reynolds numbers, the flow structure in complex channels may be fairly insensitive to such effects and depend only on the geometry. A conclusive resolution of these issues can only be based on reliable experimental results under well-planned conditions. Our goal is to contribute to this effort by focussing on eccentric annular channels as representative of more complex compound channels. The present work shares some goals with two previous studies in eccentric annular channels (Gosset & Tavoularis 2006; Piot & Tavoularis 2011), but, unlike them, it is quantitative, it extends over much wider ranges of parameters and, besides the Reynolds number effect, it also addresses the inlet conditions effect.

In this article, we will examine the dependence of flow development and flow structure in eccentric annular channels on four key factors: inlet conditions, inner-to-outer diameter ratio, eccentricity and Reynolds number. To quantify this dependence, we will compare measurements of some sensitive indicators under different conditions, with the objective to isolate the influence of each of these four factors from other effects. Tests with many combinations of values of these four factors will be examined within the following ranges: two representative sets of inlet conditions, distinguished by the effectiveness of flow management in the inlet tank; three inner-to-outer diameter ratios, namely $d/D = 0.25$, 0.50

and 0.75; a full range of eccentricities, from 0.0 to 0.9; and Reynolds numbers from 0 to 19000, which are expected to span the laminar, transitional and turbulent ranges. It is hoped that the present measurements and their analysis will enhance our understanding of the phenomena of gap instability and gap vortex street in complex channels and their dependence on geometric and dynamic conditions. They are also meant to form a substantial database for the testing of analytical models and numerical investigations.

2. Experimental facility, instrumentation and procedures

The recirculating flow loop used in these experiments, the instrumentation used for the measurements, the measurement methodology and the measurement uncertainties have been described in Part 1, so only a summary and information unavailable in Part 1 will be presented here. Sketches showing the apparatus and the annular geometry with definitions of coordinates are presented in figures 1 and 2, respectively. The annular test section had a length of $L = 1478\,\mathrm{mm}$ and consisted of two parts: an outer channel, machined and polished from acrylic blocks to a square outer surface with sides equal to 60.5 mm and a cylindrical inner surface with a diameter $D = 50.8\,\mathrm{mm}$; and one of three interchangeable cores, which were cast acrylic rods with diameters d = 12.7, 25.1 and 38.1 mm, respectively. When a core rod was in place, it was suspended at its two ends on horizontal traverses that were mounted inside the inlet and outlet tanks, away from the test section ends. Thus, the annular test section had three possible diameter ratio configurations, with $d/D \approx 0.25$, 0.50 and 0.75, corresponding to the hydraulic diameters $D_h = D - d$ = 38.1, 25.7 and 12.7 mm, respectively, and dimensionless lengths L/D_h = 38.8, 57.5 and 116.4. The eccentricity, defined as $e = 2\Delta y/(D - d)$, where Δy is the distance between the axes of the inner and outer cylinders, was adjusted to each selected value at three positions along the test section length. The uncertainty in Δy was 0.5 mm, from which one can estimate the eccentricity uncertainty as 0.04. An alternative geometrical parameter is the actual gap size δ, related to the eccentricity as $\delta = (1 - e)(D - d)/2$.

An important consideration in this work was the flow conditions at the inlet of the test section. To prevent the fluid that was discharged into the inlet tank from entering the test section as a high speed jet, the inlet tank was split vertically in two parts by a divider, which also acted as an overflow and as a support for the core traversing mechanism. Fluid from the pump impinged on the divider and recirculated in the rear chamber before entering the front chamber through the overflow and through slots machined on

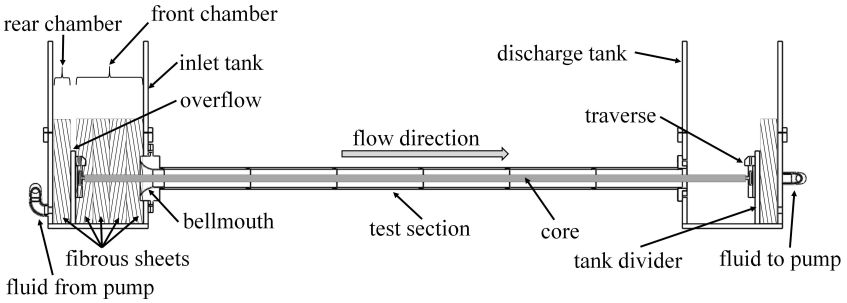

Figure 1: Sketch of the apparatus.

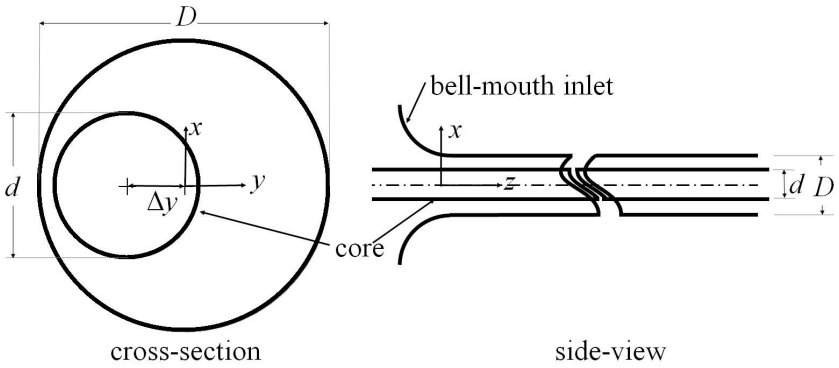

Figure 2: Annular geometry with a definition of coordinates.

the divider. The rear chamber was packed with a 50.8 mm thick fibrous sheet, which dampened the vortices generated by the jet impingement. The front chamber of the inlet tank was also partially or totally filled with fibrous sheets, which were stacked together and acted as flow management devices. The number of these sheets and the arrangement of sheets with different porosities could be changed in order to modify the inlet conditions. Flow uniformity and inlet turbulence suppression were further enhanced by the flow acceleration through a bell-mouth inlet.

Two types of fibrous sheets were used, one of which consisted of compacted hog's hair, whereas the other type was synthetic and had a more cancellous structure. Unfortunately, we had no way of quantifying, or even reproducing exactly, the properties of the sheet arrangement. For this reason, we resorted to a qualitative description of inlet conditions, which is actually based on the assessment of their effects on the flow. Based on these effects, we will distinguish between three classes of inlet-tank flow management: "mild flow management", for which we only used two (out of five possible) fibrous sheets of

the first type, "moderate flow management", for which the inlet tank was completely filled with fibrous sheets of the first type, and "strong flow management", for which the inlet tank was completely filled with a combination of fibrous sheets of both types. Measurements reported in this work were collected over a period of several years, and in some of the early work documentation of the inlet conditions was of limited extent. As the flow passed through these sheets, its non-uniformity was reduced by the incurring viscous actions and large-scale motions would tend to be broken down. At the same time, small scale-motions would be produced in the wakes of the fibres. So, overall, mild flow management would likely result in inlet flows with relatively high turbulence intensity and some remnants of slowly decaying large-scale motions, whereas strong flow management would likely result in a more uniform inlet flow with small-scale fluctuations.

Flow measurements were taken using laser Doppler velocimetry (LDV), as well as planar and stereo particle image velocimetry, but only LDV results are reported in the following, as they were sufficient to support the points of present interest. The uncertainty in the Reynolds number $\mathrm{Re} = \rho D_h U_b/\mu$, where U_b is the bulk flow velocity, was $\pm 6\%$. An upper bound for the Reynolds number that could be achieved in this apparatus with each test section in place was imposed by the pump's capacity and other features of the loop and the instrumentation. For the three test sections considered in this study, which had diameter ratios $d/D = 0.25, 0.50$ and 0.75, the maximum achievable Reynolds numbers were 9900, 15500 and 19000, respectively.

3. Issues to be investigated and investigation strategies

In Part 1, we examined in detail flow in an eccentric annular channel for a particular set of conditions, under the assumption that this was a representative case and that phenomena similar to those observed in that flow would appear under significant ranges of conditions. We identified three distinct flow regions in the considered eccentric annular channel: the entrance region, the fluctuation-growth region (FG) and the rapid-mixing region (RM). In the entrance region, fluid was diverted from the narrow gap vicinity toward the open channel and velocity fluctuations were relatively small. This region was further subdivided into two subregions: close to the inlet, there was a subregion (NE) in which there was no sign of periodic motions; and, further away, there was a subregion (PE), in which some periodicity was detectable. In the fluctuation-growth region the axial velocity at mid-gap changed from a minimum at the end of the entrance region, to

a maximum at the the start of the rapid-mixing region; the most prominent feature of the FG region was a rapid growth of quasi-periodic velocity fluctuations, which reached amplitudes that were a significant fraction of the bulk velocity. In the rapid-mixing region, the local time-averaged velocity and the amplitude of the velocity fluctuations changed by relatively small amounts; it is in this region that the gap vortex street was fully formed.

The phenomena summarized in the previous paragraph are very complex as well being prone to be sensitive to many influences. A first step towards reaching conclusions with a broader applicability is to identify the influencing factors (or sets of conditions) that affect significantly these phenomena and over which we have some control in our experiments. The conditions that could potentially have an effect on the development and state of the flow in eccentric annuli can be separated into two classes: geometric conditions and dynamic conditions. Geometric conditions include the diameter ratio, the eccentricity, and the length of the test section; wall roughness is another geometric condition, but it cannot be examined in this work because all test sections had smooth walls. Dynamic conditions include the Reynolds number and the inlet conditions.

For a clear illustration of the effects of each influencing factor, it is necessary to isolate each factor from other modifying and interfering factors; to do so, we need to control each type of condition independently of all others. For example, dynamic effects can be separated from geometry-related effects by comparing cases with different inlet conditions and Reynolds numbers, while keeping the diameter ratio, eccentricity and distance from the inlet fixed. Moreover, we need to define appropriate flow indicators, which will serve as quantitative criteria by which each effect will be evaluated. As discussed in Part 1, the phenomena of interest can be observed most vividly in the narrow gap centre ("mid-gap"); therefore, much of the following discussion will be concerned with measurements at that location. Among the many flow indicators, we selected four: the time-averaged streamwise velocity U_z, the standard deviations of the streamwise u'_z and cross-gap u'_x velocity fluctuations (all non-dimensionalized by the bulk velocity U_b) and the frequency f of the cross-flow fluctuations, expressed as a Strouhal number St = fd/U_b.

To avoid getting sidetracked, it is also necessary to limit the scope of the investigation upon aspects that are both meaningful as well as likely to be resolved by the present experiments. The first step towards this objective is to identify a set of questions to which

responses will be attempted. Among the many relevant questions that may be posed, we chose the following ones.

(a) For a given geometry and Reynolds number, is there a downstream distance beyond which the flow may be considered to be fully developed, namely statistically insensitive to axial position? Assuming that a fully developed state has been achieved, would it be independent of inlet conditions? Is there a value of the Reynolds number, beyond which the fully developed state would be also insensitive to Re?

(b) Is there a critical Reynolds number Re_{cr}, below which no gap instability occurs in an eccentric annular channel with a specified diameter ratio under any conditions? We need to emphasize that this Re_{cr} should not be confused with the synonymous property whose prediction is a main objective of linear stability analysis, as the conditions we refer to here include large disturbances of all sorts. It is an intuitive expectation, however, that such a Re_{cr} exists, because, as Re decreases, viscous effects should increase in significance and eventually dampen all motions other than the basic, parallel flow. Of course, finding experimentally the value of such a Re_{cr} is not an easy matter, because i) it is impossible to impose each and every kind of disturbance to which the flow may be sensitive, and ii) it is, in theory at least, possible for a flow that is stable within the confines of our test section to become unstable in a test section of indefinite length. These types of limitations are common to many problems in fluid mechanics; for example, it has been recognized that the Kolmogorov hypotheses, which are meant to apply to turbulent flows at arbitrarily large Reynolds numbers, cannot be disproved by any experiment which would necessarily be performed at a finite Reynolds number. Consequently, we will only seek a *practical* Re_{cr}, namely one that corresponds to *practical* levels of disturbances and *practical* channel lengths. We believe that the present apparatus length and disturbance levels are typical of conditions encountered in industrial systems, such as nuclear reactor rod bundles.

(c) Is there a critical eccentricity e_{cr}, below which no gap instability occurs in an eccentric annular channel with a specified diameter ratio under any conditions? The limitations that were mentioned in the previous paragraph would also apply to this question. Therefore, instead of an unconditional e_{cr}, we will seek a value that applies to *practical* conditions.

(d) Is it possible to reconcile results for different annular channel geometries, as far as gap instability is concerned?

4. Effect of inlet conditions on flow development

Let us first address question (a) in section 3 by examining the effects of inlet conditions on flow development and asymptotic state for a representative case, chosen to have the same geometry and Reynolds number as the one discussed in detail in Part 1. As in Part 1, we will base our discussion upon observation of the time histories of cross-flow and axial velocities, obtained by a two-dimensional LDV probe that was traversed slowly along the channel while its measurement volume was in the centre of the narrow gap. Figure 3 shows such time histories for three types of inlet-tank flow management. This figure makes it evident that the introduction of progressively stronger flow management had the effect of prolonging the entrance region, and consequently shifting the start of the fluctuation-growth region towards the downstream end of the test section. In the mild and moderate flow management cases, the FG region was succeeded by the rapid-mixing region, which occupied roughly 3/4 of the test section length for the mild flow management case and 1/4 of it for the moderate flow management case. In contrast, in the strong flow management case, the FG region emerged only at a quarter-length distance from the exit and persisted to the exit, but the trend indicates that the RM region would have appeared in this case as well had the test section been a bit longer. Based on these observations, one may say with fair confidence that the asymptotic flow state does not depend, at least qualitatively, on the inlet conditions. Therefore, it seems acceptable to disregard the inlet condition effect when we examine measurements obtained sufficiently far downstream. Of course the evidence so far has only been based on a single geometry and Reynolds number, so it is necessary to investigate whether this conclusion has a broader validity. In the remainder of this section we will focus on cases with mild and moderate flow management, which were deemed to suffice for a general qualitative illustration of the inlet condition effects.

In the following, we will investigate whether asymptotic states that are qualitatively independent of inlet conditions and Reynolds number would arise for eccentric annuli with all three diameter ratios we considered. For economy of presentation, we shall limit the discussion to two sets of representative geometries: one with an eccentricity of 0.8 and another with a relative gap size $\delta/D = 0.05$, which corresponds to $e = 0.8$ for the case with $d/D = 0.50$.

Figure 4 shows the variations of the four chosen flow indicators with the Reynolds number for three diameter ratios and two gap configurations. All measurements were taken in the centre of the narrow gap near the end of the test section, where the flow

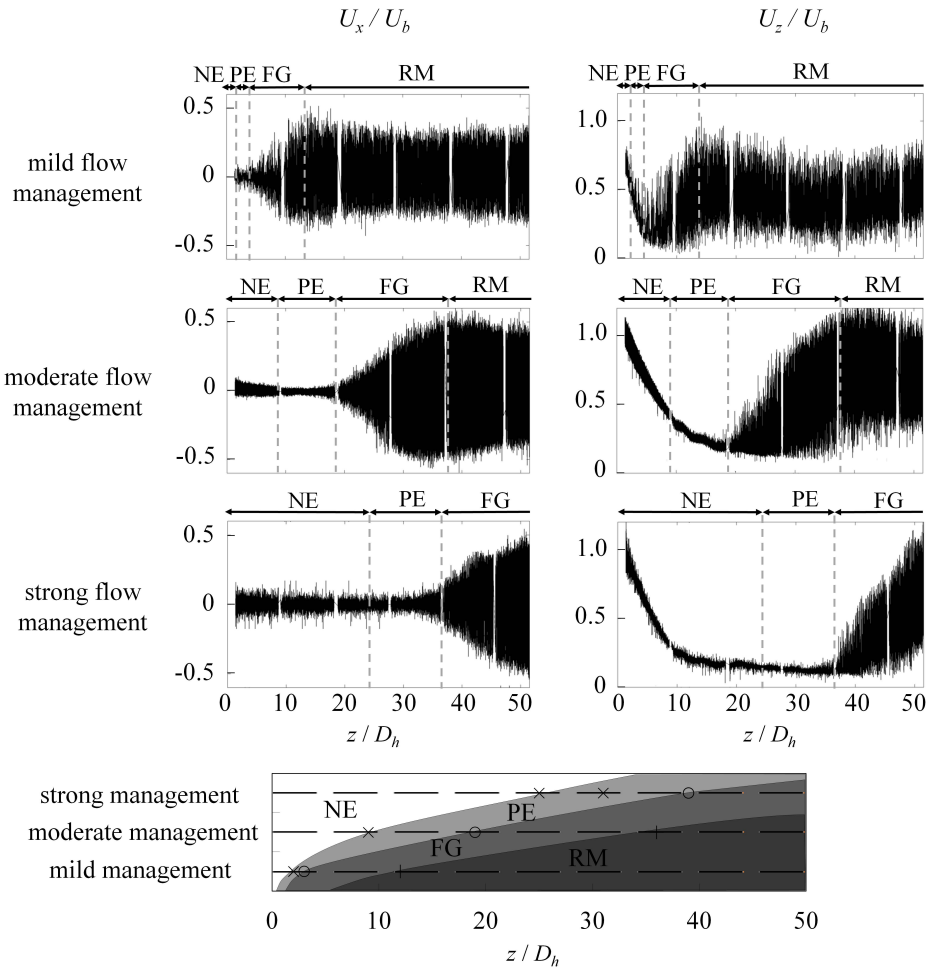

Figure 3: The top three rows present time histories of cross- and axial velocity components along the centres of the narrow gaps of annular channels with d/D = 0.50, e = 0.8, Re = 7500 and different types of flow management (these measurements were obtained by an LDV probe that was traversed very slowly along the channel); the bottom row shows a flow state map along the channel.

was most likely to be fully developed, if it ever reached that stage of development. This position corresponded to z/D_h = 36, 54, and 108 for the annuli with d/D = 0.25, 0.50 and 0.75, respectively. The left column in this figure is for e = 0.8, while the right one is for a gap size δ/D = 0.05. Measurements are reported for two sets of inlet conditions: mild flow management, indicated by dashed lines and hollow symbols, and moderate flow management, indicated by solid lines and filled symbols; cross-hatched or shaded areas are bounded by the loci of mild and moderate flow management points.

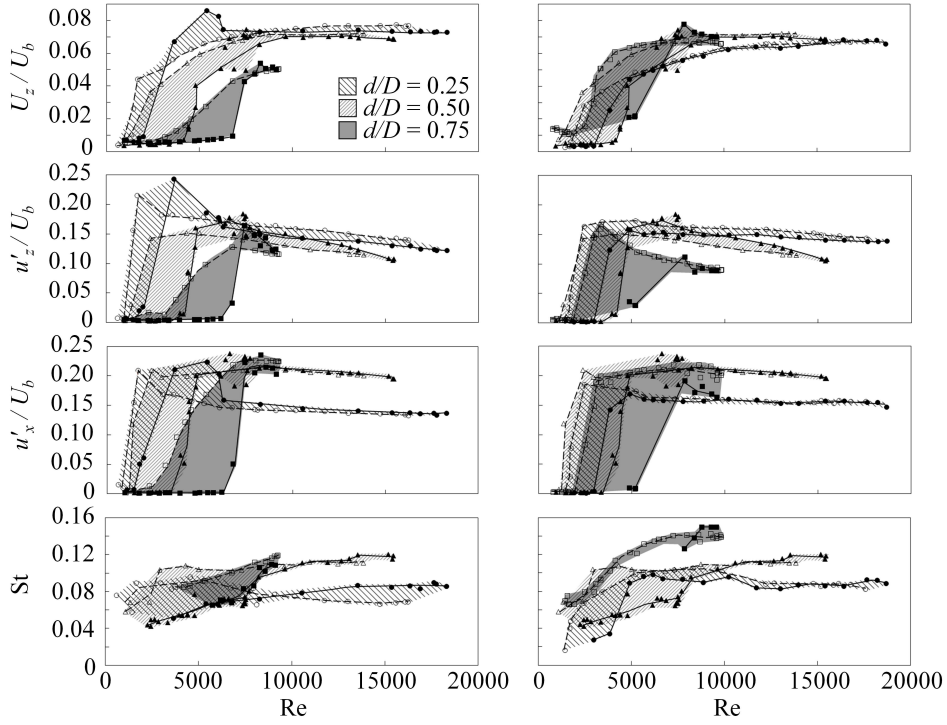

Figure 4: Reynolds number dependence of the time-averaged streamwise velocity, the standard deviations of the streamwise u'_z and cross-gap u'_x velocity fluctuations (all non-dimensionalized by the bulk velocity) and the Strouhal number for $e = 0.8$ (left column) and $\delta/D = 0.05$ (right column). Solid lines and filled markers represent moderate flow management, while dashed lines and hollow markers represent mild flow management. Circular, triangular and square symbols indicate annuli with $d/D = 0.25, 0.50$ and 0.75, respectively. Cross-hatched or shaded areas are bounded by the loci of measurements under moderate and mild flow management conditions for each diameter ratio.

A common feature observed for all cases examined is that, at low Re, gap velocity, gap fluctuations and gap Strouhal number increased with increasing Re, whereas at sufficiently large Re these four parameters reached asymptotes, or showed a tendency towards such behaviour. This is consistent with many other flow phenomena which become weakly dependent, if at all, on Re at large Re and so it is not a surprise. Nevertheless, the dependence of this behaviour upon inlet conditions is unmistakeable: the lower bound of Re for quasi-asymptotic attainment of the four indicators is lower for the case of mild flow management cases than for the corresponding moderate flow management cases. This observation conforms with our expectations: compared to moderate flow management, mild flow management allows stronger disturbances to enter the channel, which

are more effective in triggering the instability and vortex generation mechanisms at relatively low Re. At sufficiently large Re, however, the flow becomes sensitive to even small disturbances and so the inlet conditions have no effect on the asymptotic state. The lower bound of Re for the quasi-asymptotic state varies somewhat with geometry and flow indicator used; however, a value that is representative of all cases considered is about 7000, which is approximately the condition examined in Part 1.

5. Flow patterns for different eccentricities and Reynolds numbers

In this section, we will investigate whether the succession of flow regions identified in Part 1 and in the previous section for $d/D = 0.50$, $e = 0.8$ and Re = 7300 can also be found under different conditions. At the same time, we will attempt to provide an answer to questions (b) and (c) in section 3. To reduce the complexity of the discussion, we will first focus on the effects of eccentricity and Reynolds number for the case with $d/D = 0.50$ and we'll discuss the effect of diameter ratio in a following section. Moreover, we will consider mainly one type of inlet conditions, ones that were previously characterised as moderate flow management. The furthest downstream measurement location for these experiments was at $z/D_h \approx 54$ and consequently only phenomena that are present within the available test section were documented. Nevertheless, in cases in which the flow structure demonstrated a well established trend, one might speculate with some confidence on how the flow would have developed in a longer test section. Moreover, as mentioned in section 3, a specific objective of this work was to document the flow patterns not under any arbitrary conditions of disturbances and apparatus lengths, but under "practical" ones.

Figure 5 shows an array of time histories at mid-gap, measured by a slowly traversed LDV probe and obtained with moderate flow management for eccentricities in the range $0.4 \leqslant e \leqslant 0.9$ and Reynolds numbers in the range $2100 \leqslant Re \leqslant 15500$. Similar measurements were also made for lower eccentricities and lower Reynolds numbers, but are not presented here as they showed no evidence for the presence of periodic motions. Following procedures explained in Part 1, one may visually assert whether, for any given e – Re combination, the flow state at the end of the channel is in the entrance region, the fluctuation-growth (FG) region or the rapid-mixing (RM) region. To illustrate whether each flow has a quasi-periodic component or not, we have presented representative segments of local time histories at $z/D_h \approx 53$ in figures 6 and 7 for the cross- and axial flow velocity components, respectively. In most cases, observation of the signal pattern

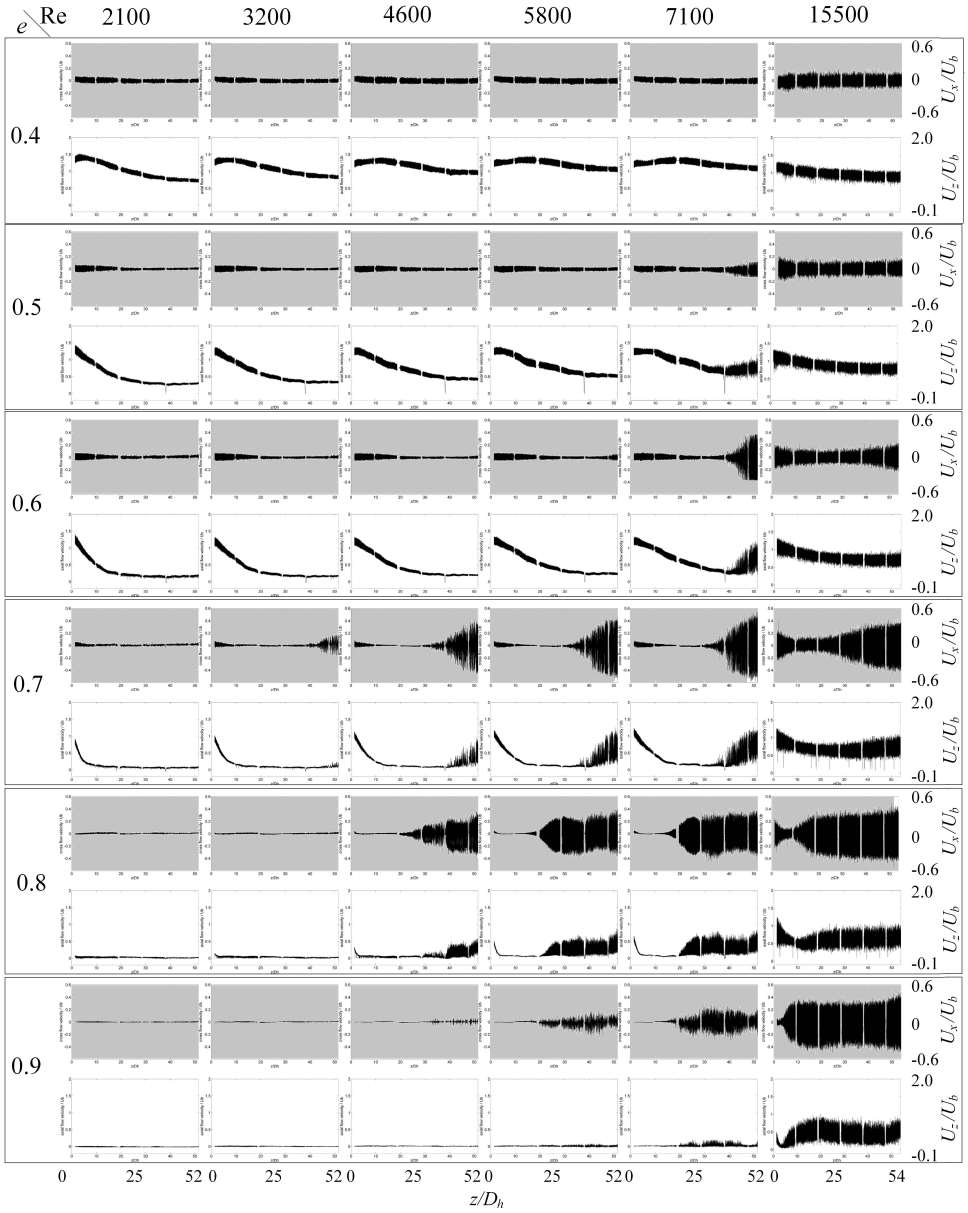

Figure 5: Time histories of cross- and axial velocity components along the centres of the narrow gaps of annular channels with d/D = 0.50 and moderate flow management for different eccentricities and Reynolds numbers; these measurements were obtained by an LDV probe that was traversed very slowly along the channel.

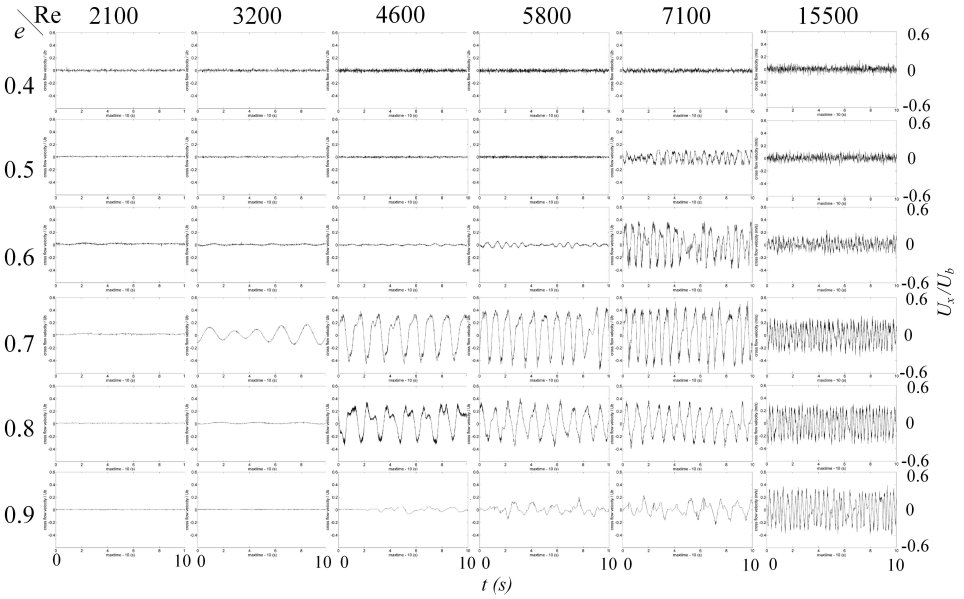

Figure 6: Time histories of mid-gap cross-flow velocity in annular channels with d/D = 0.50 and moderate flow management for different eccentricities and Reynolds numbers; these measurements were obtained by an LDV probe fixed at $z/D_h \approx 53$.

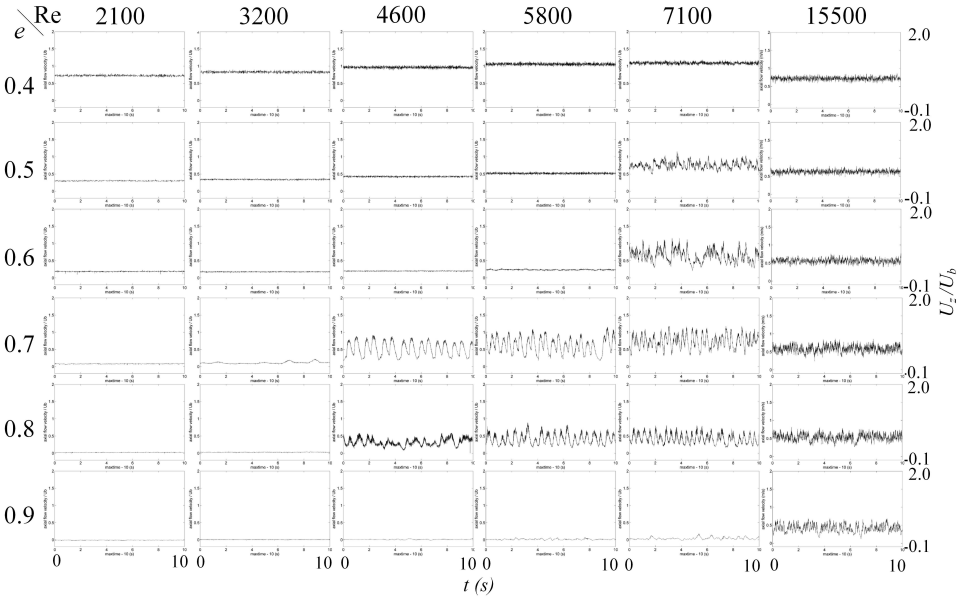

Figure 7: Time histories of mid-gap axial flow velocity in annular channels with d/D = 0.50 and moderate flow management for different eccentricities and Reynolds numbers; these measurements were obtained by an LDV probe fixed at $z/D_h \approx 53$.

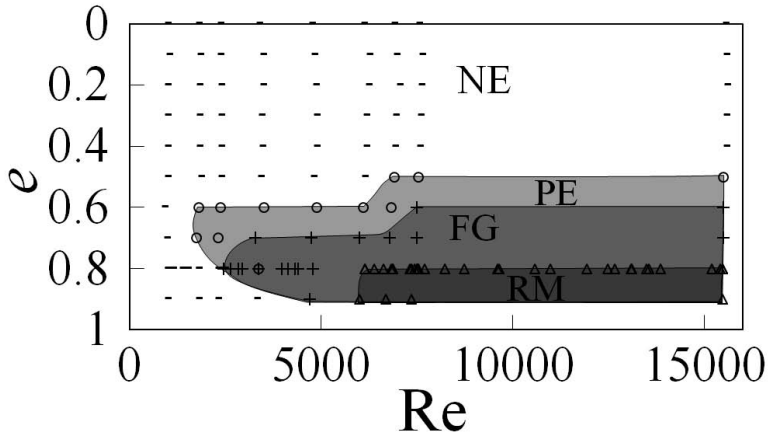

Figure 8: Flow state map near near the exits ($z/D_h \approx 53$) of eccentric annular channels with $d/D = 0.50$ and moderate flow management.

makes it evident whether a flow exiting the channel was in the non-periodic (NE) or the periodic (PE) subregion of the entrance region. To increase our confidence in this assessment, the visual identification of periodicity was confirmed by inspection of power spectra (not shown here) of long time histories of the mid-gap cross-flow at $z/D_h \approx 53$, which clearly revealed whether they had prominent peaks or not.

A summary of our observations concerning the states of the flows near the channel's exit is shown in the form of a flow state map in figure 8. Although the presented results only extend to Reynolds numbers up to 15500, based on figure 4, we can plausibly anticipate that the flow states would not change significantly with increasing Re beyond that value. Of course, a question that cannot be conclusively answered by the present results is whether, and under which conditions, the flow states would change further downstream, if the channel were longer than the present one. The main observations from this map can be summarized as follows. It is noted that the values of Reynolds numbers and eccentricities cited in this discussion are not meant to be exact but indicative of magnitude.

- For Re < 1100, no periodicity was detectable for any eccentricity, so one may conclude that this is approximately the *practical, universal, critical Reynolds number*, below which all practical flows in eccentric annuli with $d/D = 0.50$ would be unconditionally stable as far as gap instability is concerned. This value was established with a relatively high confidence by using a wider range of measurements than the ones shown in the previous

figures. Later in this section, we will discuss the dependence of the critical Reynolds number on eccentricity.

- For $e < 0.5$, no periodicity was detectable for any Reynolds number, so one may conclude that this is approximately the *practical critical eccentricity*, below which flow in practical eccentric annuli with $d/D = 0.50$ would be unconditionally stable as far as gap instability is concerned.
- For $1100 < \mathrm{Re} < 3500$, weak periodic motions became measurable for an intermediate, narrow range of eccentricities. This indicates that the gap instability mechanism was activated under these conditions. Whether and under which conditions these motions may eventually grow to the fluctuation-growth stage cannot be resolved by the present results.
- For $3500 < \mathrm{Re} < 5500$, there is a range of eccentricities for which periodic motions reached the fluctuation-growth stage. This range must surely include cases that would develop to the rapid-mixing stage in a longer channel.
- For the cases that had an identifiable FG region, the entrance length was rather insensitive to Reynolds number, although it varied with eccentricity.
- For $5500 < \mathrm{Re}$, there is a range of eccentricities for which the annular flow reached the rapid-mixing stage, which may be deemed to indicate the full development of the gap vortex street.
- For all Reynolds numbers, one may speculate that, as eccentricity approaches 1, cross-gap flows would be progressively obstructed, and they would cease altogether when the core contacts the outer channel ($e = 1$). The minimum eccentricity (or minimum gap size) for cross-flows to be significant would likely diminish with increasing Re. Nevertheless, it should also be noted that the absence of cross-gap motions does not necessarily exclude the presence of instability and even vortex formation in the two mixing layers on either side of the gap. A remaining question, to be addressed in future research, is whether rapid-mixing in highly eccentric channels can exist without significant cross-gap motions.

The flow regime map in figure 8 applies to moderate inlet flow management conditions. Based on the observations made with regards to figure 3 and many other similar observations, we may assess with a fair degree of confidence that the lower bounds of the flow development regions in figure 8 would generally shift toward the left under milder inlet flow management conditions and towards the right under stronger ones.

To investigate the Reynolds number dependence of flow instability in annular channels with different eccentricities, we conducted a series of specific experiments in flows with $d/D = 0.50$ and moderate inlet flow management conditions. We repeated these tests for eccentricities in the range $0 \leqslant e \leqslant 0.9$, with increments of 0.1. For each eccentricity, the tests started at a very low Re, typically of the order of 100. After the flow was given sufficient time to reach stationarity, cross- and axial velocity time histories were recorded at mid-gap near the exit of the channel. Then, the flow rate was increased by a small amount (typically by Re increments of 150 in the sensitive range) and the same type of measurements were recorded again; this was repeated until the flow rate reached the maximum capacity of the pump. The same tests were also repeated by starting at the highest obtainable flow rate and decreasing it gradually, so that we could identify possible hysteresis effects. We inspected all signals carefully and noted the conditions at which we observed a significant change in their patterns. In general, we observed two types of pattern changes, both of which were drastic, repeatable and unmistakeable.

At low eccentricities, the velocity fluctuation level increased measurably for a small increase in Re, but the signals showed no evidence of periodicity. We interpreted this as an indication of transition to turbulence in the gap region and noted the Reynolds number at which this occurred as Re_{tr}. At high eccentricities, the cross-flow velocity signal attained a quasi-periodic waveform when the Reynolds number exceeded a value Re_{cr}, which we interpreted as the critical Reynolds number for gap instability.

Figure 9 summarizes the values of the critical and transitional Reynolds numbers for different eccentricities. Non-periodic transition at $\mathrm{Re}_{tr} \approx 6000$ was observed for the cases with $0 \leqslant e \leqslant 0.4$, whereas in the case with $e = 0.5$ transition to turbulence and the appearance of periodic motions appeared almost simultaneously, as though one triggered the other. It is noted that the absence of turbulence in the gap region does not necessarily exclude its presence in other parts of the channel. For eccentricities in the range $0.6 \leqslant e \leqslant 0.9$, the onset of periodic motions was observed at Reynolds numbers that increased monotonically from 1100 for $e = 0.6$ to 3800 for $e = 0.9$. This trend is consistent with the observations of Gosset & Tavoularis (2006) and Piot & Tavoularis (2011) and demonstrates that increasing eccentricity tends to strengthen viscous forces, which in turn tend to impede gap instability.

A close examination of the velocity signals revealed a wealth of interesting patterns, which in their details depended on the geometric and dynamic conditions. For example,

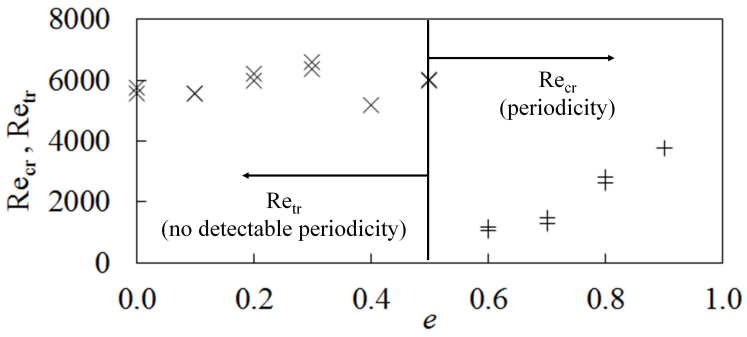

Figure 9: Critical Reynolds number for gap instability and transition to turbulence Reynolds number versus eccentricity.

in the PE subregion, the cross-flow signal (figure 6) had a quasi-sinusoidal waveform at relatively low Reynolds numbers, but, as Re increased, the signal appearance tended towards a square wave shape; with further increase in Re, the same signal tended towards a triangular waveform. This progression indicates that, besides a fundamental oscillation mode that appears at the onset of gap instability while Re is not much larger than Re_{cr}, additional modes and/or harmonics are triggered with increasing Re. Signal modulation at lower frequencies was also observed in some cases. Analysis of such phenomena is beyond the scope of the present work.

6. Towards a quantification of eccentricity and Reynolds number effects

This section presents comparisons of the values of the four previously introduced flow indicators at mid-gap and near the exit of the channel for wide ranges of eccentricities and Reynolds numbers (see figure 10). To avoid complications stemming from additional geometric and dynamic effects, only cases with the same diameter ratio (0.50) and the same level of inlet flow management (moderate) were included in the comparisons. The findings of these quantitative comparisons are meant to complement the qualitative observations that were presented in previous sections. It is, of course, recognized that, among the cases for which periodic motions were detected, only few reached a fully developed state, namely exhibited a rapid mixing region, as demonstrated in figure 8. Comparisons of values and trends for the different cases shown in figure 10 have resulted in the following main observations.

In general, and with some notable exceptions, the normalized mid-gap axial velocity

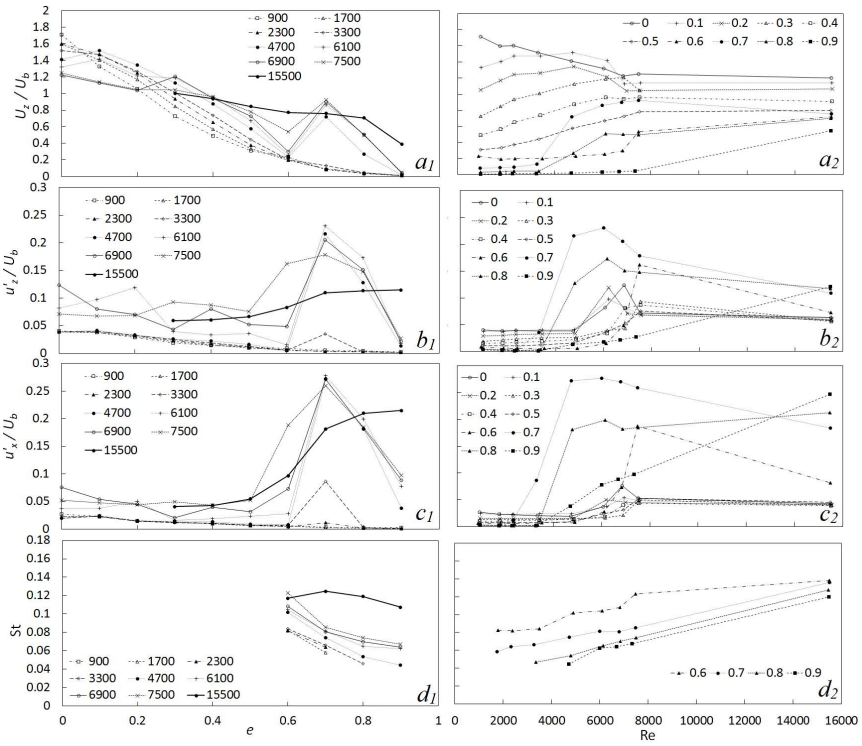

Figure 10: Dependence of the time-averaged streamwise velocity, the standard deviations of the streamwise and cross-gap velocity fluctuations (all non-dimensionalized by the bulk velocity) and the Strouhal number at mid-gap near the exit of the test section ($z/D_h \approx 53$) upon eccentricity and Reynolds number; in all cases, d/D = 0.50 and inlet conditions corresponded to moderate flow management.

decreased with increasing eccentricity and increased gradually with increasing Reynolds number. For very low eccentricities ($0 \leqslant e \leqslant 0.4$), this velocity was fairly insensitive to e and also showed reversing trends with Re. In contrast, for very high eccentricities ($0.6 \leqslant e \leqslant 0.9$) and 4700 < Re < 7500, the mid-gap velocity was significantly higher than values consistent with the overall decreasing trend and in some cases reached levels consistent with higher turbulence at Re = 15500. The mid-gap velocity fluctuation level was fairly low and insensitive to eccentricity for $0 \leqslant e \leqslant 0.4$, but it both increased and became $e-$sensitive for $0.6 \leqslant e \leqslant 0.9$. The velocity fluctuation level in the low$-e$ range was also insensitive to Reynolds number up to some Re and then showed a moderate increase at some Re in the range 4700 < Re < 6100; this moderate increase is attributed to the onset of transition to turbulence in the gap region, rather than gap instability and related phenomena. At high eccentricities, however, the mid-gap fluctuation level

increased nearly abruptly at some Re-value, as a result of the flow entering the fluctuation growth region. These observations support other indications that flows in the low and high e–ranges belong to different classes.

In all cases with Re $\leqslant$ 7500 that had periodic motions, the Strouhal number St = fd/U_b decreased measurably with increasing eccentricity. It also increased at a very slow rate with increasing Reynolds number in the range 1500 $\leqslant$ Re $\leqslant$ 7500; at higher Re, figure 4 demonstrates that the Strouhal number tended towards asymptotic values. For Re = 15500 the Strouhal number appears to be less sensitive to eccentricity; this may be due to the increased turbulence level in the entire cross-sectional area, which tends to reduce the non-uniformity of the azimuthal velocity variation. A comparison of results at Re = 15500 obtained under different inlet conditions showed that a change of inlet flow management from moderate to strong resulted in a 16% change in the Strouhal number, which is comparable to the variation of the Strouhal number with eccentricity. This observation implies that the large-Re limit for St may be weakly dependent on inlet conditions.

7. Effects of geometry on the flow characteristics

In this section, we will address question (d) of section 3, namely we will investigate the effect of annular geometry (*i.e.*, the inner-to-outer diameter ratio and eccentricity) on the flow structure away form the inlet and, as much as possible, independently of Reynolds number effects. As demonstrated in a previous section, inlet effects for the three geometries considered ceased to be significant in the present test sections for Re $\gtrsim$ 7000, so we will only consider results in this Re-range. For a meaningful comparison of the three cases, it is necessary to compare results at the same Re, which should be as large as possible. Because the highest Re that could be achieved in the channel with d/D = 0.75 was 9300, we will focus on results taken at this Reynolds number. Another concern was to isolate the effect of diameter ratio from other geometric effects. It has been amply demonstrated that the phenomena of interest in this work depend strongly upon the relative size of the narrow gap; however, it is not clear whether it is the eccentricity, the absolute gap size or some other parameter that plays an important role. After considering various possibilities, we decided to make two sets of comparisons: first, to evaluate the diameter effect while keeping the eccentricity constant and equal to 0.80, which is the value used most extensively in Part 1 and the present article; and second, to evaluate

d/D	e	δ/D	U_z/U_b	u'_z/U_b	u'_x/U_b	St
0.25	0.80	0.075	0.735	0.157	0.147	0.076
0.50	0.80	0.050	0.707	0.142	0.213	0.107
0.75	0.80	0.026	0.501	0.120	0.214	0.114
0.25	0.87	0.050	0.606	0.155	0.158	0.100
0.50	0.80	0.050	0.707	0.142	0.213	0.107
0.75	0.60	0.050	0.684	0.090	0.184	0.144

Table 1: Asymptotic values of the normalized mid-gap mean axial flow velocity, normalized standard deviation of axial and cross-flow fluctuations and Strouhal number for different diameter ratios; Re ≈ 9300.

the diameter effect while keeping the gap size δ/D constant and equal to 0.05, which corresponds to $e = 0.8$ for the $d/D = 0.50$ case.

Table 1 summarizes the relevant values of the chosen four flow indicators, as extracted from figure 4. It was shown previously that the dimensionless mid-gap velocity U_z/U_b was affected strongly by the gap vortex street and increased considerably from the FG region to the RM region. Increasing the diameter ratio while keeping the eccentricity constant generally resulted in lower mid-gap axial velocities (figure $4a_1$). For the same gap size (figure $4a_2$), U_z/U_b for the three diameter ratios changed by lesser amounts and did not have a monotonic trend. This appears to show that U_z/U_b is more dependant on the gap size than on the diameter ratio within the ranges considered. The mid-gap axial flow fluctuations u'_z/U_b appear to decrease with increasing diameter ratio, both under constant eccentricity (figure $4b_1$) and under constant gap size (figure $4b_2$). The mid-gap cross-flow fluctuations u'_x/U_b decrease from the case with $d/D = 0.25$ to the one with $d/D = 0.50$ but stay about the same for the case with $d/D = 0.75$.

An important parameter of interest in this work is the frequency of periodic motions, which was found not to change significantly along a channel with a fixed geometry at a fixed Reynolds number. To present this frequency in dimensionless form, *i.e.*, as a Strouhal number, we need a length scale and a velocity scale. In previous discussion up to this point, we have used the inner diameter d and the bulk velocity U_b as scales. These scales apply to the channel as a whole and may be suitable for scaling frequencies in channels with the same cross-sectional shape but different sizes or different Reynolds numbers in the asymptotic state of development. Nevertheless, the same scales are not sensitive to the channel's internal geometry, namely the diameter ratio and eccentricity, and this explains why St was found to vary with these parameters. As discussed in Part

1, gap instability originates in the mixing layers forming on either side of the gap and, consequently, frequency scaling should be based on length and velocity scales that are relevant to these mixing layers, rather than the channel as a whole. Consequently, it seems logical for one to choose a length scale that is a measure of the mixing layer thickness and a velocity scale that is a measure of the convection speed of periodic motions in the mixing layer. In a plane mixing layer, the convection speed of vortices is equal to the average velocity of the two streams, but there is no obvious choice of this scale for an eccentric annular channel. By analogy to a plane mixing layer, one could use the bulk velocity as representative of the high-velocity side of the gap mixing layer and then seek an empirical expression for the low-velocity side. In the absence of an all-encompassing theory of gap instability, we will attempt an empirical determination of both the length scale and the velocity scale, which would necessarily be valid within the ranges of measurements used for the empirical fits but whose general validity would need to be tested under a variety of geometrical conditions.

The shape of the annular geometry is defined by the diameter ratio and the eccentricity, so these parameters could be used as independent variables for scaling purposes. Instead of eccentricity, however, which is a rather complex property, it seems more straightforward to assume that the mixing layer strength would depend on the ratio of narrow and wide gap sizes δ/Δ, which is related to eccentricity as $\delta/\Delta = (1-e)/(1+e)$, such that $\delta/\Delta = 1$ when $e = 0$ and $\delta/\Delta = 0$ when $e = 1$. Therefore, the mixing layer length and velocity scales can be expressed as $\phi_1(\frac{d}{D}, \frac{\delta}{\Delta})d$ and $\frac{1}{2}U_b\left[1+\phi_2(\frac{d}{D}, \frac{\delta}{\Delta})\right]$, respectively, where $\phi_1(\frac{d}{D}, \frac{\delta}{\Delta})$ and $\phi_2(\frac{d}{D}, \frac{\delta}{\Delta})$ are empirical dimensionless functions. Then, a Strouhal number of the periodic motions in eccentric annular channels may be defined in terms of mixing layer scales as

$$\mathrm{St}^* = \frac{f d \phi_1(\frac{d}{D}, \frac{\delta}{\Delta})}{\frac{1}{2}U_b\left[1+\phi_2(\frac{d}{D}, \frac{\delta}{\Delta})\right]}. \tag{7.1}$$

If sufficient data were available for the complete determination of the functions ϕ_1 and ϕ_2, the issue of empirical description of geometry effects upon the frequency of periodic motions would be resolved. Unfortunately, a complete set of data is not available. To proceed, we will test two simplifying hypotheses, which have some plausible physical basis. We will assume that the length scale is insensitive to δ/Δ and that the velocity scale is insensitive to d/D within the range of present conditions. Then, an approximate

d/D	e	δ/Δ	St	$\phi_1{}'$	$\phi_2{}'$	$\mathrm{St}^{*\prime}$
0.25	0.80	0.111	0.087	11.465	-0.872	15.630
0.50	0.80	0.111	0.128	7.815	-0.872	15.630
0.75	0.80	0.111	0.140*	7.143	-0.872	15.630
0.50	0.50	0.250	0.133	7.815	-0.867	15.630
0.50	0.60	0.176	0.139	7.815	-0.861	15.630
0.50	0.70	0.111	0.136	7.815	-0.864	15.630
0.50	0.80	0.053	0.128	7.815	-0.872	15.630
0.50	0.90	0.053	0.120	7.815	-0.880	15.630
0.25	0.87	0.071	0.087	11.465	-0.878	16.317
0.50	0.80	0.111	0.128	7.815	-0.872	15.630
0.75	0.60	0.250	0.150*	7.143	-0.861	15.418

Table 2: Estimates of the mixing layer length and velocity scale functions and the corresponding Strouhal numbers and data used for their determination.

mixing layer Strouhal number can be defined as

$$\mathrm{St}^{*\prime} \approx \frac{f d \phi_1'(\frac{d}{D})}{\frac{1}{2}U_b\left[1+\phi_2'(\frac{\delta}{\Delta})\right]} \approx \mathrm{St}\frac{\phi_1'(\frac{d}{D})}{\frac{1}{2}\left[1+\phi_2'(\frac{\delta}{\Delta})\right]}. \tag{7.2}$$

The empirical function $\phi_1{}'(\frac{d}{D})$ can be determined as a curve fitted to measurements of St under constant e and varying d/D, whereas $\phi_2{}'(\frac{\delta}{\Delta})$ can be determined as a curve fitted to measurements of St under constant d/D and varying e.

Data used for the curve fitting and for validation of 7.2 have been collected in table 2. For the $d/D = 0.25$ and 0.50 cases, values of St in table 2 correspond to Re $\approx$ 16000; for the $d/D = 0.75$ case, in which such a high Re could not be achieved in our apparatus, values of St, which have been marked by an asterisk, were obtained by extrapolation towards higher Re. All data presented in table 2 were collected in channels with strong inlet flow management.

The function $\phi_1{}'$ was determined by fitting a parabola to the three values of St for $e = 0.80$ and different d/D, whereas the function $\phi_2{}'$ (equation 7.4) was determined by fitting a quartic polynomial to the five values of St for $d/D = 0.50$ and different e. The corresponding fitted equations are as follows

$$\phi_1{}' = 23.8(d/D)^2 - 32.5(d/D) + 18.1 \tag{7.3}$$

and

$$\phi_2{}' = 11.7(\delta/\Delta)^4 - 9.79(\delta/\Delta)^3 + 2.28(\delta/\Delta)^2 - 0.0560(\delta/\Delta) - 0.882\ . \tag{7.4}$$

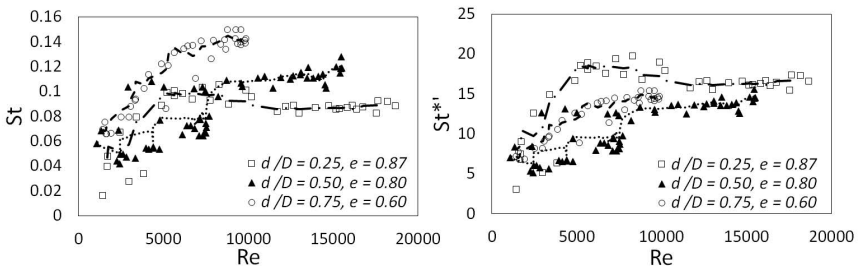

Figure 11: Dependence of Strouhal number (left) and mixing layer Strouhal number (right) on the Reynolds number for annular channels with d/D = 0.25, 0.50, and 0.75; in all cases, δ/D = 0.05.

Because the fitted polynomials were of the highest possible order, both curves had perfect fits to all data points that were used. Therefore, we could only test the validity of 7.2 against two cases in table 2, for which both d/D and e differed from the reference values. As the same table shows, the values of $\mathrm{St}^{*\prime}$ predicted by 7.2 for these two cases differed from the reference value by less than 6%, which is remarkably small in view of the approximations that were made during this process. Additional support for the fair predictive accuracy of 7.2 for annular channels is provided by figure 11, which shows all available values of St and $\mathrm{St}^{*\prime}$ for annular channels with δ/D = 0.05; whereas the values of St for different d/D approach distinct asymptotes at high Re, all values of $\mathrm{St}^{*\prime}$ converge towards the common asymptote 15 ± 3. In summary, a Strouhal number that was based on mixing layer scales was found to be much more appropriate than the commonly used parameter for providing a universal description of the vortex street periodicity in annular channels at relatively large Reynolds numbers.

8. Summary and concluding remarks

In this work we identified several flow indicators that are relevant to gap instability in eccentric annular channels and examined their dependence on inlet conditions, inner-to-outer diameter ratio, eccentricity and Reynolds number. These flow indicators were the mid-gap axial flow velocity, the axial and cross-flow velocity fluctuations and the Strouhal number of the cross-flow oscillations; all measured were in the middle of the narrow gap and normalized by the bulk velocity.

Inlet conditions were found to affect the flow development, as progressively stronger flow management prolonged the entrance region and shifted the development of periodic motions and ensuing phenomena further downstream. In general, at low Re, the four flow

indicators increased with Re, at rates which were highly dependant on inlet conditions; however, at higher Re, all these indicators approached asymptotic values which were only mildly sensitive to inlet conditions. Flows with mild inlet management (namely, with stronger inlet disturbances) reached their asymptotic states closer to the inlet than those with moderate or strong management.

For a range of Reynolds number and eccentricity, we constructed state maps which show the various stages of flow development for a particular set of inlet conditions. It was found that, for Re < 1100 or for $e < 0.5$, no periodicity was detectable and the flow was unconditionally stable to gap instability. For $e \leqslant 0.5$, transition to turbulence occurred at Re ≈ 6000, whereas, for $0.6 \leqslant e \leqslant 0.9$, the critical Reynolds number for the formation of periodic motions was found to increase with eccentricity from 1100 for $e = 0.6$ to 3800 for $e = 0.9$.

The normalized mid-gap axial flow velocity generally decreased with increasing eccentricity, and increased asymptotically with increasing Reynolds number. The rate of increase was accelerated with the ensuing gap instability when conditions for its development were favourable. The axial and cross-flow fluctuation intensities were insensitive to eccentricity for $0 \leqslant e \leqslant 0.5$; they peaked at $e = 0.7$ for Re ⩽ 7500 and at $e = 0.9$ for Re = 15500.

It was found that the use of an empirical mixing layer Strouhal number allows a universal description of the vortex street periodicity for $Re > 10500$ and for all geometries and upstream conditions considered; the average value for this mixing layer Strouhal number was 15 ± 3.

Financial support by the Natural Sciences and Engineering Research Council of Canada and Atomic Energy of Canada Limited are gratefully acknowledged.

REFERENCES

Baratto, F., Bailey, S. C. & Tavoularis, S. 2006 Measurments of frequencies amd spatial correlations of coherent structures in rod bundle flows. *Nucl. Eng. Des.* **236**, 1830–1837.

Chang, D. & Tavoularis, S. 2008 Simulations of turbulence, heat transfer and mixing across narrow gaps between rod- bundle subchannels. *Nucl. Eng. Des.* **238** (1), 109–123.

Choueiri, G. H. & Tavoularis, S. submitted, 2013 Experimental investigation of flow development and gap vortex street in an eccentric annular channel. part 1. overview of the flow structure. *J. Fluid Mech.* .

Gosset, A. & Tavoularis, S. 2006 Laminar flow instability in a rectangular channel with a cylindrical core. *Phys. Fluids* **18**, 044108.

Guellouz, M. S. & Tavoularis, S. 2000a The structure of turbulent flow in a rectangular channel containing a cylindrical rod - part 1: Reynolds-averaged measurements. *Exp. Therm. Fluid Sci.* **23**, 59–73.

Guellouz, M. S. & Tavoularis, S. 2000b The structure of turbulent flow in a rectangular channel containing a cylindrical rod - part 2: Phase-averaged measurements. *Exp. Therm. Fluid Sci.* **23**, 75–91.

Hooper, J. D. 1983 Large scale structural effects in a symmetrical four-rod subchannel. In *Eighth Australasian Fluid Mechanics Conference*. Newcastle, New South Wales.

Hooper, J. D. 1984 The development of a large structure in the rod gap region for turbulent flow through closely spaced rod arrays, in: Fourth symposium on turbulent shear flows. In *Fourth Symposium on Turbulent Shear Flows*, pp. 1.23–1.27. Karlsruhe, Germany.

Hooper, J. D. & Rehme, K. 1984 Large-scale structural effects in developed turbulent flow through closely spaced rod array. *J.Fluid Mech.* **145**, 305–337.

Hooper, J. D. & Wood, D. H. 1984 Fully developed rod bundle flow over a large range of reynolds number. *Nucl. Eng. Des.* **83**, 3146.

Meyer, L. 2010 From discovery to recognition of periodic large scale vortices in rod bundles as source of natural mixing between subchannels - a review. *Nucl. Eng. Des.* **240**, 1575–1588.

Möller, S. V. 1991 On phenomena of turbulent flow through rod bundles. *Exp. Therm. Fluid Sci.* **4**, 25–35.

Piot, E. & Tavoularis, S. 2011 Gap instability in laminar flows in eccentric annular channels. *Nucl. Eng. Des.* **241** (11), 4615–4620.

Rehme, K. 1987 The structure of turbulent flow through rod bundles. *Nucl. Eng. Des.* **99**, 141154.

Rehme, K. 1989 Experimental observations of turbulent flow through subchannels of rod bundles. *Exp. Therm. Fluid Sci.* **2**, 341349.

Rowe, D. S., Johnson, B. M. & Knudsen, J. G. 1974 Implications concerning rod bundle crossflow mixing based on measurment of turbulent flow sturcture. *Int. J. Heat Mass Tran.* **17**, 407–419.

Tapucu, A. & Merilo, M. 1977 Studies on diversion cross-flow between two parallel channels communicating by a lateral slot. ii: Axial pressure variations. *Nucl. Eng. Des.* **42**, 307318.

Tavoularis, S. 2011 Rod bundle vortex networks, gap vortex streets, and gap instability: a nomenclature and some comments on available methodologies. *Nucl. Eng. Des.* **241** (11), 4612–4614.

Chapter 6

Conclusions and recommendations for future work

6.1 Summary of results

In the first part of this work, we investigated isothermal flow development and structure in a strongly eccentric annular channel, considered to be representative of complex channels having narrower regions that are adjacent to wider ones. This flow was shown to be very complicated, with dominant features that are absent from flows in channels with relatively simple cross-sections, such as pipes, rectangular channels or concentric annular channels.

Based on observations of the streamwise evolution of the mean velocity components at various azimuthal positions, we have identified three distinct flow development regions: the entrance region, the fluctuation-growth region, and the rapid-mixing region. In the entrance region, fluid was diverted from the narrow gap vicinity towards the open channel and velocity fluctuations were relatively small. Closer observation of velocity fluctuations in the entrance region led us to subdivide it into an initial subregion, in which there was no evidence of any periodic motions, and a following subregion, in which periodicity was detectable in the velocity field.

The axial velocity at mid-gap reached a minimum at the end of the entrance region,

but increased again to a higher level in the fluctuation-growth region. The most prominent feature of flow in the latter region was a rapid growth of the quasi-periodic velocity fluctuations, which reached amplitudes that were a significant fraction of the bulk velocity.

In the rapid-mixing region, the local time-averaged velocity and the amplitude of the velocity fluctuations changed by relatively small amounts, but the flow structure underwent a drastic change in that a vortex street, consisting of pairs of counter-rotating vortices on either side of the gap, was formed and fluid mixing became very thorough in the entire channel. The generation of this "gap vortex street" was attributed to the instability of the two mixing layers that formed between slower fluid in the gap and faster fluid elsewhere.

In the second part of this work, we identified several flow indicators that are relevant to gap instability in eccentric annular channels and examined their dependence on inlet conditions, inner-to-outer diameter ratio, eccentricity and Reynolds number. These flow indicators were the mid-gap axial flow velocity, the axial and cross-flow velocity fluctuation intensity and the Strouhal number of the cross-flow oscillations.

Inlet conditions were found to affect the flow development, as progressively stronger flow management prolonged the entrance region and shifted the development of periodic motions and ensuing phenomena further downstream. In general, at low Re, the four flow indicators increased with Re, at rates which were highly dependant on inlet conditions; however, at higher Re, all these indicators approached asymptotic

values which were not sensitive to inlet conditions. Flows with mild inlet management (namely, with stronger inlet disturbances) reached their asymptotic states closer to the inlet than those with moderate or strong management.

For a range of Reynolds number and eccentricity, we constructed state maps which show the various stages of flow development for a particular set of inlet conditions. It was found that, for Re < 1100 or for $e < 0.5$, no periodicity was detectable and the flow was unconditionally stable to gap instability. For $e \leq 0.5$, transition to turbulence occurred at Re ≈ 6000, whereas, for $0.6 \leq e \leq 0.9$, the critical Reynolds number for the formation of periodic motions was found to increase with eccentricity from 1100 for $e = 0.6$ to 3800 for $e = 0.9$.

The normalized mid-gap axial flow velocity generally decreased with increasing eccentricity and increased asymptotically with increasing Reynolds number. The axial and cross-flow fluctuation intensities were insensitive to eccentricity for $0 \leq e \leq 0.5$; they peaked at $e = 0.7$ for Re ≤ 7500 and at $e = 0.9$ for Re = 15500.

It was found that the use of an empirical mixing layer Strouhal number allows a universal description of the vortex street periodicity for $Re > 10500$ and for all geometries and upstream conditions considered; the average value for this mixing layer Strouhal number was 15 ± 3.

6.2 Main contributions of this thesis

The work presented in this thesis follows many studies on related topics by several authors over many years. However, this is the first study to synthesize the analysis of

several types of strategically planned measurements and to reconstruct the sequence of events which lead to the formation of a gap vortex street and its important consequences on flow mixing in complex channels. It has also elucidated the underlying reasons that drive gap instability and gap vortex street formation.

The uses of an optically accessible test section and a refractive index matching fluid permitted the non-intrusive collection of velocity measurements in essentially the entire annular channel. This allowed us to examine in detail the onset of gap instability under different geometric and dynamic conditions and its development to a vortex street following the formation of two sufficiently strong mixing layers on either side of the narrow gap. For the first time, we identified three distinct flow development regions and the conditions under which these are present in a particular flow.

For the first time, stereoscopic PIV measurements were used to confirm the hypothesis proposed by Piot & Tavoularis (2011), which associates gap instability with the inflection points of the azimuthal peak velocity profile.

This study is amongst the few which examined gap instability and the resulting gap vortex street in detail for a wide range of Reynold numbers, extending over laminar, transitional and turbulent flows. Moreover, it covered the entire range of eccentricities and a range of diameter ratios of the annular channels. We were also the first to study experimentally the effect of upstream conditions on the flow development and structure. Our study allowed us to identify quantitatively the critical Reynolds

numbers for transition to turbulence and gap instability in eccentric annular channels. Additionally, by analysing the large database of measurements collected under various geometric, dynamic, and upstream conditions, we were able to define an empirical Strouhal number, which permitted for the first time for eccentric annular channels a universal description of gap vortex street periodicity.

6.3 Recommendations for future work

In closing, we would like to present a few recommendations for future work on this topic. The length of the present test section imposed unnecessary limitations on the present experiments. The use of a much longer test section would allow flows under a wider set of dynamic and geometric conditions to reach their final stage of development. It is recognised that extending the test section would be faced with technical challenges, one of which would be to maintain a uniform gap width between the core and the enclosure. Another area that deserves additional investigation is the importance of the existence of a gap for the formation and growth of the gap vortex street. Future experiments with the gap blocked over the entire test section length, or in parts of it, would help resolve this question. Experiments in annular channels with a wider range of inner-to-outer diameter ratios and in complex channels with different cross-sectional shapes would be beneficial for testing the universality of the proposed mixing layer Strouhal number. A final, and most important, recommendation for future work is to apply similar experimental methods to the investigation of the gap vortex network that is expected to appear in tightly packed rod bundles.

Bibliography

Baratto, F., Bailey, S. C. & Tavoularis, S. 2006 Measurments of frequencies amd spatial correlations of coherent structures in rod bundle flows. *Nucl. Eng. Des.* **236**, 1830–1837.

Batchelor, G. K. 1967 *An introduction to fluid dynamics.*. Cambridge University Press.

Bhowmik, G. & Bose, S. 2010 *Analyticals Techniques in Biotechnology.*. Tata McGraw-Hill Education.

Bradshaw, P. 1987 Turbulent secondary flows. *Annu. Rev. Fluid Mech.* **91** (1), 53–74.

Chang, D. & Tavoularis, S. 2005 Unsteady numerical simulations of turbulence and coherent structures in axial flow near a narrow gap. *J. Fluid Eng. - T. ASME* **127** (3), 458–466.

Chang, D. & Tavoularis, S. 2007 Numerical simulation of turbulent flow in a 37-rod bundle. *Nucl. Eng. Des.* **237** (6), 575–590.

Chang, D. & Tavoularis, S. 2008 Simulations of turbulence, heat transfer and mixing across narrow gaps between rod- bundle subchannels. *Nucl. Eng. Des.* **238** (1), 109–123.

Chang, D. & Tavoularis, S. 2012 Numerical simulations of developing flow and vortex street in a rectangular channel with a cylindrical core. *Nucl. Eng. Des.* **243**, 176–199.

Drazin, P. G. 2002 *Introduction to hydrodynamic stability.*. Cambridge ; New York: Cambridge University Press.

Drazin, P. G. & Reid, W. H. 2004 *Hydrodynamic stability.*. Cambridge; New York: Cambridge University Press,.

Fox, R. W., McDonald, A. T. & Pritchard, P. J. 2004 *Introduction to fluid mechanics.*, 6th edn. Hoboken, N.J.: Wiley.

Gosset, A. & Tavoularis, S. 2006 Laminar flow instability in a rectangular channel with a cylindrical core. *Phys. Fluids* **18**, 044108.

Grandy, Walter T. & Grandy, Walter T. 2008 *Entropy and the Time Evolution of Macroscopic Systems*. Oxford ; New York; Oxford.

Greitzer, E. M., Tan, C. S. & Graf, M. B. 2004 *Internal flow : concepts and applications*. New York: Cambridge University Press,.

Guellouz, M. S., Kaddeche, S., Sebti, M. B. & Salah, N. Ben 2009 On the formation of coherent structures in narrow gaps of complex channels a linear stability analysis. In *NURETH-13*. Kanazawa, Japan.

Guellouz, M. S. & Tavoularis, S. 2000a The structure of turbulent flow in a rectangular channel containing a cylindrical rod - part 1: Reynolds-averaged measurements. *Exp. Therm. Fluid Sci.* **23**, 59–73.

Guellouz, M. S. & Tavoularis, S. 2000b The structure of turbulent flow in a rectangular channel containing a cylindrical rod - part 2: Phase-averaged measurements. *Exp. Therm. Fluid Sci.* **23**, 75–91.

Home, D., Arvanitis, G., Lightstone, M. F. & Hamed, M. S. 2009 Simulation of flow pulsations in a twin rectangular sub- channel geometry using unsteady reynolds averaged navier- stokes modelling. *Nucl. Eng. Des.* **239** (12), 2964–2980.

Hooper, J. D. 1980 Developed single phase turbulent flow through a square- pitch rod cluster. *Nucl. Eng. Des.* **60** (3), 365–379.

Hooper, J. D. 1983 Large scale structural effects in a symmetrical four-rod subchannel. In *Eighth Australasian Fluid Mechanics Conference*. Newcastle, New South Wales.

Hooper, J. D. 1984 The development of a large structure in the rod gap region for turbulent flow through closely spaced rod arrays, in: Fourth symposium on turbulent shear flows. In *Fourth Symposium on Turbulent Shear Flows*, pp. 1.23–1.27. Karlsruhe, Germany.

Hooper, J. D. & Rehme, K. 1984 Large-scale structural effects in developed turbulent flow through closely spaced rod array. *J.Fluid Mech.* **145**, 305–337.

Hooper, J. D. & Wood, D. H. 1984 Fully developed rod bundle flow over a large range of reynolds number. *Nucl. Eng. Des.* **83**, 31–46.

Ikeno, T. & Kajishima, T. 2010 Analysis of dynamical flow structure in a square arrayed rod bundle. *Nucl. Eng. Des.* **240** (2), 305–312.

Krauss, T. & Meyer, L. 1996 Characteristics of turbulent velocity and temperature in a wall channel of a heated rod bundle. *Exp. Therm. Fluid Sci.* **12**, 75–86.

Krauss, T. & Meyer, L. 1998 Experimental investigation of turbulent transport of momentum and energy in a heated rod bundle. *Nucl. Eng. Des.* **180**, 185–206.

Lee, K. B. & Jang, H. C. 1997 A numerical prediction on the turbulent flow in closely spaced bare rod arrays by a nonlinear k-epsilon model. *Nucl. Eng. Des.* **172** (3), 351–357.

Levchenko, Yu D., Subbotin, V. I. & Ushakov, P. A. 1972 Experimental investigation of averaged characteristics of turbulent flow in cells of rod packs. *Soviet Atomic Energy* **33** (5), 1035–1042.

Lexmond, A. S., Mudde, R. F. & van der Hagen, T. H. J. J. 2005 Visualisation of the vortex street and characterisation of the cross flow in the gap between two sub-channels. In *NURETH-11*. Avigon, France.

Mahmood, A., Rohde, M., van der Hagen, T. H., Mudde, R. F. & Ikeno, T. 2011 An experimental study of identification of flow patterns responsible for crossflow in a vertical tube bundle geometry. In *NURETH-14*.. Toronto, Canada.

Mahmood, A., Rohde, M., van der Hagenand, T. H. J. J. & Mudde, R. F. 2009 Contribution of large-scale coherent structures towards the cross flow in two interconnected channels. In *NURETH-13*. Kanazawa, Japan.

Massey, B. & Ward-Smith, A. 2006 *Mechanics of Fluids*, 8th edn. London, Uk: Taylor & Francis.

Mayer, G. & Hzi, G. 2006 Direct numerical and large eddy simulation of longitudinal flow along triangular array of rods using the lattice boltzmann method. *Math. Comput. Simulat.* **72** (2-6), 173–178.

Mayer, G., Ples, J. & Hzi, G. 2007 Large eddy simulation of subchannels using the lattice boltzmann method. *Ann. Nucl. Energy* **34** (1-2), 140–149.

Merzari, E. & Ninokata, H. 2009 Anisotropic turbulence and coherent structures in eccentric annular channels. *Flow Turbul. Combust.* **82** (1), 93–120.

Merzari, E., Ninokata, H. & Baglietto, E. 2008*a* Numerical simulation of flows in tight- lattice fuel bundles. *Nucl. Eng. Des.* **238** (7), 1703–1719.

Merzari, E., Wang, S., Ninokata, H. & Theofilis, V. 2008*b* Biglobal linear stability analysis for the flow in eccentric annular channels and a related geometry. *Phys. Fluids* **20** (11).

Meyer, L. 2010 From discovery to recognition of periodic large scale vortices in rod bundles as source of natural mixing between subchannels - a review. *Nucl. Eng. Des.* **240**, 1575–1588.

Meyer, L. & Rehme, K. 1994 Large-scale turbulence phenomena in compound rectangular channels. *Exp. Therm. Fluid Sci.* **8** (4), 286–304.

Meyer, L. & Rehme, K. 1995 Periodic vortices in flow through channels with longitudinal slots or fins. In *Tenth Symposium on Turbulent Shear Flows*. Pennsylvania, U.S.A.

Möller, S. V. 1991 On phenomena of turbulent flow through rod bundles. *Exp. Therm. Fluid Sci.* **4**, 25–35.

Mott, J. E. & Joseph, D.D. 1968 Stability of parallel flow between concentric cylinders. *Phys. Fluids* **11**, 2065–2073.

Nikitin, N. V. 2006 Direct numerical simulation of turbulent flows in eccentric pipes. *Comput. Maths. Math. Phys.* **46** (3), 489–504.

Ninokata, H., Merzari, E. & Khakim, A. 2009 Analysis of low reynolds number turbulent flow phenomena in nuclear fuel pin subassemblies of tight lattice configuration. *Nucl. Eng. Des.* **239** (5), 855–866.

Piot, E. & Tavoularis, S. 2011 Gap instability in laminar flows in eccentric annular channels. *Nucl. Eng. Des.* **241** (11), 4615–4620.

Rapley, C. W. & Gosman, A. D. 1986 The prediction of fully developed axial turbulent flow in rod bundles. *Nucl. Eng. Des.* **97** (3), 313–325.

Rayleigh, Lord 1880 On the stability of certain fluid motions. *Proc. Math. Soc.* **11**, 57–70.

Rehme, K. 1987 The structure of turbulent flow through rod bundles. *Nucl. Eng. Des.* **99**, 141–154.

Rehme, K. 1989 Experimental observations of turbulent flow through subchannels of rod bundles. *Exp. Therm. Fluid Sci.* **2** (3), 341–349.

Rehme, K. 1992 The structure of turbulence in rod bundles and the implications on natural mixing between the subchannels. *Int. J. Heat Mass Tran.* **35** (2), 567–581.

Rowe, D. S., Johnson, B. M. & Knudsen, J. G. 1974 Implications concerning rod bundle crossflow mixing based on measurment of turbulent flow sturcture. *Int. J. Heat Mass Tran.* **17**, 407–419.

Seale, W. J. 1979 Turbulent diffusion of heat between connected flow passages. part 1: outline of problem and experimental investigation. *Nucl. Eng. Des.* **54** (1), 183–195.

Silin, N. & Juanic, L. 2006 Experimental study on the reynolds number dependence of turbulent mixing in a rod bundle. *Nucl. Eng. Des.* **236** (18), 1860–1866.

Silin, N., Juanic, L. & Delmastro, D. 2004 Thermal mixing between subchannels: Measurement method and applications. *Nucl. Eng. Des.* **227** (1), 51–63.

Silin, N., Masson, V. & Rauschert, A. 2008 Large-scale pulsation detection by means of temperature measurments. *J. Heat Transfer* **130** (11), 111602.

Skinner, V. R., Freeman, A. R. & Lyall, H. G. 1969 Gas mixing in rod clusters. *Int. J. Heat Mass Transfer* **12** (3), 265–278.

Snyder, W. T. & Goldstein, G. T. 1965 An analysis of fully developed laminar flow in an eccentric annulus. *AIChE J.* **11** (3), 462–467.

Tachibana, F., Oyama, A., Akiyama, M. & Konodo, M. 1969 Measurments of heat transfer coefficients for axial alir flow through eccentric annulus and seven-rod cluster. *Nucl. Sci. Technol.* **6**, 207–214.

Tapucu, A. & Merilo, M. 1977 Studies on diversion cross-flow between two parallel channels communicating by a lateral slot. ii: Axial pressure variations. *Nucl. Eng. Des.* **42**, 307–318.

Tavoularis, S. 2007 Theory of turbulence. MCG 5152 course notes.

Tavoularis, S. 2011 Rod bundle vortex networks, gap vortex streets, and gap instability: A nomenclature and some comments on available methodologies. *Nucl. Eng. Des.* **241** (7), 2624–2626.

Vonka, V. 1988a Measurement of secondary flow vortices in a rod bundle. *Nucl. Eng. Des.* **106** (2), 191–207.

Vonka, V. 1988b Turbulent transports by secondary flow vortices in a rod bundle. *Nucl. Eng. Des.* **106** (2), 209–220.

Wu, Ge 2010 *Assay Development : Fundamentals and Practices*. Hoboken: John Wiley & Sons, Inc.

Wu, X. & Trupp, A. C. 1993 Experimental study on the unusual turbulence intensity distributions in rod-to- wall gap regions. *Exp. Therm. Fluid Sci.* **6** (4), 360–370.

Zhang, Z. 2010 *LDA application methods laser doppler anemometry for fluid dynamics*. Berlin ; London: Springer.